Conductive Si Doped Metal Oxide Fuel Cell Catalyst Supports: Understanding the Role of Si Content

by

Mason Thomas Sullivan

A thesis submitted to the
School of Graduate and Postdoctoral Studies in partial
fulfillment of the requirements for the degree of

Master of Science in Materials Science

Faculty of Science

University of Ontario Institute of Technology (Ontario Tech University)

Oshawa, Ontario, Canada

August 2021

THESIS EXAMINATION INFORMATION

Submitted by: **Mason T. Sullivan**

Master of Science in **Materials Science**

Thesis title:
Conductive Si Doped Metal Oxide Fuel Cell Catalyst Supports: Understanding the Role of Si Content

An oral defense of this thesis took place on August 18th, 2021 in front of the following examining committee:

Examining Committee:

Chair of Examining Committee	Dr. Theresa Stotesbury, Ontario Tech University
Research Supervisor	Dr. E. Bradley Easton, Ontario Tech University
Examining Committee Member	Dr. Rachel Wortis, Trent University
Examining Committee Member	Dr. Brian J. MacLean, St. Francis Xavier University
Thesis Examiner	Dr. Jean-Paul Desaulniers, Ontario Tech University

The above committee determined that the thesis is acceptable in form and content and that a satisfactory knowledge of the field covered by the thesis was demonstrated by the candidate during an oral examination. A signed copy of the Certificate of Approval is available from the School of Graduate and Postdoctoral Studies.

ABSTRACT

Current proton exchange membrane fuel cell (PEMFC) catalysts commonly use platinum supported on carbon (Pt/C) which is susceptible to corrosion, thus a highly conductive and stable Ti_3O_5 doped by Si (TOS) conductive metal oxide catalyst support is reported. The TOS support was optimized for 20 wt% Si and surface area. The support was studied under intensive electrochemical durability tests and exhibited impressive durability and stability, narrow band gap and high electronic conductivity. The TOS support was platinized (Pt/TOS) and possessed high stability under and electrochemical durability test while experiencing ca. 15% loss to the electrochemical surface area (ECSA) compared to the commercial Pt/C catalyst which decayed by 90%. The Pt/TOS catalyst maintained adequate electroactivity and stability toward the ORR and produced a maximum power density of 900 mW cm^{-2} compared to 850 mW cm^{-2} for Pt/C.

Keywords: metal oxide; electrocatalyst support; durability; proton exchange membrane fuel cell

AUTHOR'S DECLARATION

I hereby declare that this thesis consists of original work of which I have authored. This is a true copy of the thesis, including any required final revisions, as accepted by my examiners.

I authorize the University of Ontario Institute of Technology (Ontario Tech University) to lend this thesis to other institutions or individuals for the purpose of scholarly research. I further authorize University of Ontario Institute of Technology (Ontario Tech University) to reproduce this thesis by photocopying or by other means, in total or in part, at the request of other institutions or individuals for the purpose of scholarly research. I understand that my thesis will be made electronically available to the public.

_____ Mason T. Sullivan

STATEMENT OF CONTRIBUTIONS

Part of the work described in Chapter 3 has been published as follows:

Sullivan, M. T., Alipour Moghadam Esfahani, R. & Easton, E. B. Conductive Metal Oxide-Based Fuel Cell Catalyst Supports Prepared by Doping TiO2 with Si: Understanding the Role of Si Content ECS Trans. 97, 659–670 (2020).

In Chapter 4, the TOS_{SG} catalyst support and Pt/TOS_{SG} catalyst were synthesized by Dr. Reza Alipour Moghadam Esfahani. I performed all physical and electrochemical characterization experiments.

ACKNOWLEDGEMENTS

I would like to express my appreciation to my supervisor Dr. Brad Easton. I am grateful for your encouragement and patience throughout my time in the Easton lab group. As a student in the Easton group, I have learned many things and connected with some amazing people which I will carry with me as my adventure post-grad school unfolds. I would also like to thank my committee members, Dr. Brian MacLean and Dr. Rachel Wortis, for their constructive criticism and comments.

I would like to take this time to dedicate this dissertation to my late grandfather Thomas Sullivan and to my greatest childhood friend, Ruby, both whom I lost during this degree. I am forever grateful for the way you both touched my life.

A huge shoutout to Easton group members, past and present. It was a tremendous privilege to work alongside you all. While it has been a wild ride as we faced a pandemic, I am indebted to you all for the support you provided and all the fun we've had along the way. I would also like to further express my thanks to Holly Fruehwald (PhD candidate), Dr. Reza Alipour, and Dr. Iraklii Ebradlize for their guidance and patience when teaching me how to use the various instruments in the lab.

To Dr. Richard Bartholomew, Michael Allison, Clayton Jakins, Genevieve Barnes, Stephanie Mavilla, and Cristen Hucaluk: thank you for the office chats and support as both a student and TA. Each of you made the teaching and learning experience in Chemistry labs/tutorials an enjoyable one. To everyone else I have befriended and met along this adventure in the Ontario Tech U community: thank you. The benefit of being a part of this small but ever-growing community meant friends were near and new relationships were never too far away.

Lastly, words cannot express my appreciation for all the accommodations made and support given by my family and friends. Especially my oldest friends: Jeff Holmes, Regan Turner, Jacob Raggiunti, Brandon Laughlin, and Alex Wheeler.

TABLE OF CONTENTS

LIST OF FIGURES

Chapter 1: Introduction

LIST OF TABLES

LIST OF ABBREVIATIONS AND SYMBOLS

AADT	After accelerated durability test
ADT	Accelerated durability test
AST	Accelerated stress test
BADT	Before accelerated durability test
BET	Brunauer-Emmett-Teller
BOL	Beginning of Life
CE	Counter electrode
CV	Cyclic voltammogram
DoE	Department of Energy
ECSA	Electrochemical surface area
EDX	Energy dispersive x-ray
EIS	Electrochemical impedance spectroscopy
FC	Fuel cell
FCT	Fuel cell test
GDE	Gas diffusion electrode
GDL	Gas Diffusion Layer
HOR	Hydrogen oxidation reaction
LSV	Linear sweep voltammogram
MEA	Membrane electrode assembly
NP	Nanoparticle
OCV	Open Circuit Potential
O_2	Oxygen
OH	Hydroxyl group
ORR	Oxygen reduction reaction
PEM	Proton exchange membrane
PGM	Platinum group metals
RDE	Rotating disk electrode
RE	Reference electrode

RHE	Reversible hydrogen electrode
RΣ	Total resistance
SEM	Scanning electron microscope
SMSI	Strong metal-support interaction
SU/SD	Startup/shutdown
TEM	Transmission electron microscope
TOM	Ti_3O_5 doped by Mo
TOMS	Ti_3O_5 doped by Mo and Si
TOS	Ti_3O_5 doped by Si
WE	Working electrode
XRD	X-ray diffraction

Chapter 1: Introduction

1.1 Background on Fuel Cell Technology

In recent years, the global spotlight has concentrated on a sustainable future that includes reducing CO_2 emissions or "decarbonizing solutions", improvement of air quality, and establishing a wealthy, clean energy supply.[1–4] This has catalyzed interest toward clean energy sources, hydrogen and fuel cell (FC) technology for instance, over the last few decades.[3,5–10] Hydrogen is of particular interest due to its availability from a vast number of renewable and non-renewable energy sources including solar, hydro, wind, and nuclear power. Combining these, hydrogen can be produced at the megaton scale (~50 million tons per year).[11] The Hydrogen Council, an initiative started by various international corporations, aims to position hydrogen as the catalyst for the transition from carbon-based economy to a renewable energy-based economy.[12] To achieve this, several key challenges must be overcome include: (i) various processes and sources from which hydrogen can be produced, therefore there exists a vast range of costs and emissions associated with these processes; (ii) application of hydrogen must be versatile (ie. transportation, heating, electricity); (iii) expansion of the hydrogen infrastructure off pre-existing networks.

FCs serve a key role in sustainable energy as electrochemical devices which directly convert chemical energy into electrical energy in just one step. On the other hand, combustion engines involve various steps between fuel injection and energy output. The initial concept of the FC dates back to 1839 and was invented by Sir William Grove.[13–15] This involved an electrolyzer intended for educational purposes to show the electrochemical dissociation of water.[14,16] He eventually demonstrated the reverse process could generate electricity. While this device was

labeled a “gas battery”, it was eventually referred to as a fuel cell. A century later, in 1939, Sir Francis Bacon started his famous work on fuel cells. The final and fully operational product was accepted by NASA into the U.S. Apollo space program.[13]

As technology advances, so to do the innovations which have enabled FCs to achieve operational efficiencies up to 65% (compared to the 25% efficiency associated with internal combustion vehicles). Through the combination of thermal and electrical energy, the efficiency of FCs can be boosted to 80%.[17] When operating under pure hydrogen gas, the efficiency can be enhanced past 90%.[18] In addition to efficiency, these devices offer silent and low temperature operation, and zero to low emissions. To realize the full potential of fuel cell technology and facilitate the transition from a carbon-based economy to a hydrogen-based economy, there are several barriers which must be overcome: (i) hydrogen infrastructure: both the development and cost associated with it, must be reduced; (ii) stationary and mobile FC technology solutions must undergo constant development and refinement (ie. durability and degradation, efficiency, and safety); (iii) the technology must be commercialized.[1,4] Proton exchange membrane fuel cells (PEMFCs) are one such example that addresses the concerns above.

1.2 Proton Exchange Membrane Fuel Cell (PEMFC)

PEMFCs are electrochemical energy conversion systems which offer an efficient pathway, using hydrogen gas as fuel, to reduce carbon emissions in many applications such as the transportation sector. Specifically, the PEMFC uses hydrogen and oxygen gas primarily to produce electricity with water and some heat as by-products. In this thesis, the membrane electrode assembly (MEA) within the PEMFC is of particular interest. The MEA is comprised of 3 main components: 1) a negatively charged electrode (anode), 2) a positively charged electrode

(cathode), and 3) the PEM which is sandwiched between the anode and cathode (Figure 1.1).

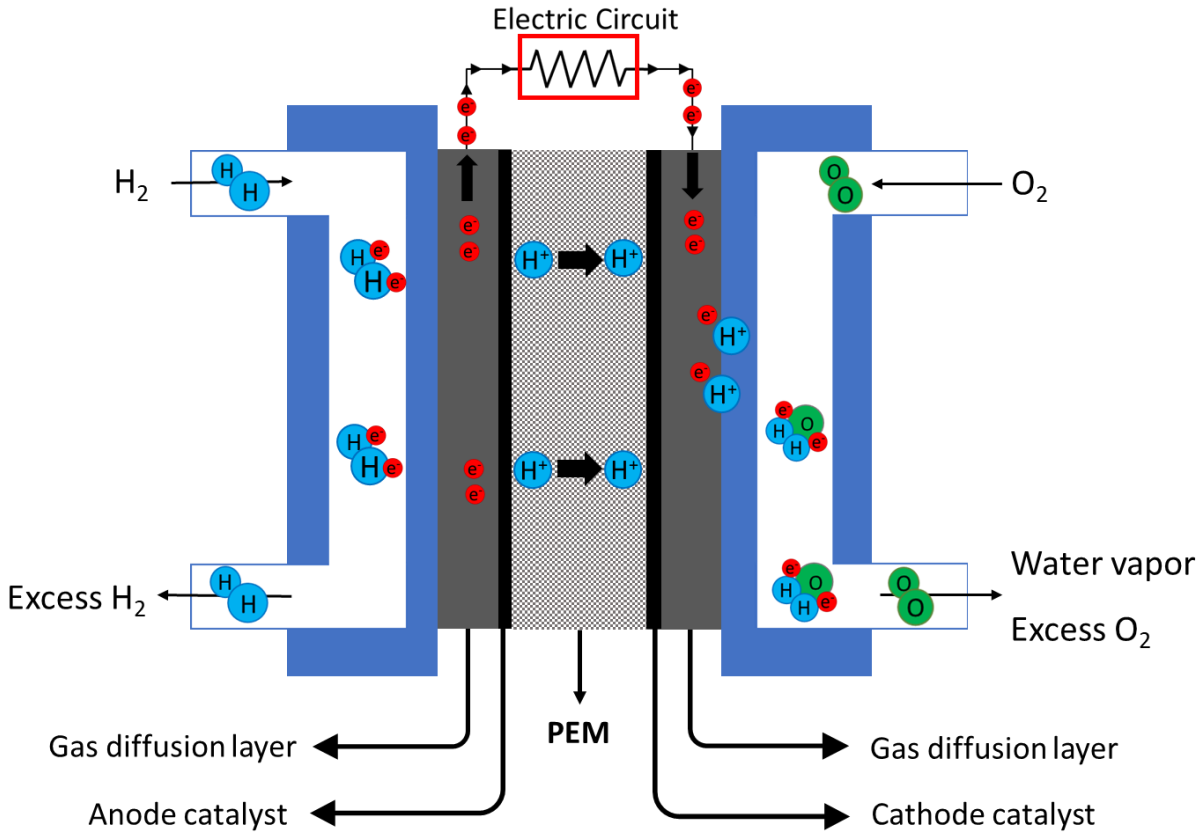

Figure 1.1. Schematic for the proton exchange membrane fuel cell.

The two redox reactions central to PEMFC operation are shown in Figure 1.1. Starting at the anode, hydrogen is introduced to the cell and undergoes the hydrogen oxidation reaction (HOR) whereby the hydrogen fuel is oxidized and split into protons (H^+) and electrons (e^-):

$$H_2 \rightarrow 2H^+ + 2e^- \qquad E^o = 0.00\ V \tag{1.1}$$

The electrons pass through an external circuit to provide power while the protons permeate through the PEM toward the cathode. The second redox reaction occurs at the cathode where oxygen is reduced and recombined with the protons and electrons to produce water and some

heat as byproducts. This is called the oxygen reduction reaction (ORR):

$$\frac{1}{2}O_2 + 2H^+ + 2e^- \rightarrow H_2O \qquad E^o = +1.23\,V \tag{1.2}$$

The ORR is a kinetically slow process which dictates the overall performance of the PEMFC. As such, there has been much development toward PEMFC ORR catalysts.[3,19–23] The PEM should be insulative to fuel and oxidants at the anode while possessing high proton conductivity (0.1 S cm^{-1}) and exhibit mechanical and thermal stability to withstand fuel cell operating conditions.[24] In addition, the PEM serves to separate the electrons from protons during anodic redox processes. A common PEM material is Nafion®, a fluoropolymer, designed by DuPont to conduct protons.

1.3 PEMFC Electrocatalysts and Supports

There are 4 criteria which must be considered when choosing a PEMFC catalyst material for the ORR: (1) the catalyst material should be able to facilitate enough adsorption of O_2 to initiate a reaction but not too much as to inhibit the catalyst active sites; (2) the material should be selective toward the 4-electron process of H_2O formation rather than the 2-electron process of H_2O_2 formation which is known to be detrimental to the PEMFC; (3) the material must be stable against the harsh, corrosive environments of PEMFC operation; and (4) the catalyst should bear high resistance to poisoning by impurities found within the reactant gases and in the PEMFC.[6,25] The most common catalyst is platinum (Pt) which is a rare and expensive noble metal thus hindering the commercialization of PEMFCs due to the expensive costs associated with the catalyst component. The classical volcano plot representing the binding energy of oxygen to various metals is shown in Figure 1.2a which demonstrates Pt is the closest metal to the theoretical activity peak.[25] However, ORR activity is not just a measure of oxygen binding energy

alone, as the ORR mechanism follows a 2-step process which is initiated by the binding of oxygen (O_2) to the catalyst surface. This is followed by the association of hydroxyl groups (OH) which is further reduced to produce H_2O and finally dissociates from the catalyst surface and this activity is better represented in Figure 1.2b. Indeed, other metal catalysts have been investigated such as copper and nickel however these bind too strongly with O_2 and become unreactive as their surfaces become oxidized. Metals such as silver and gold are associated with higher O_2 binding energies thus making it harder for O_2 to bind to the metal surface.[25] This will result in poorer activity as it becomes limited by the dissociation of O_2 or the rate at which electrons and protons can be transferred between the reactant and catalyst.

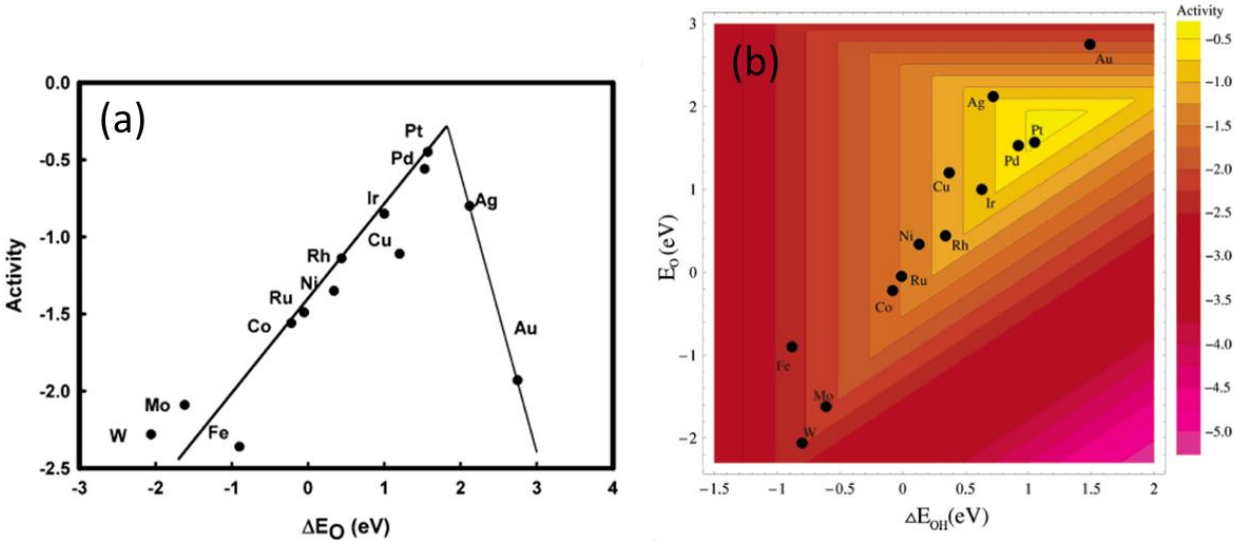

Figure 1.2. (a) Volcano plot showing the trend in oxygen reduction activity as a function of the binding energy of oxygen. (b) Trends in oxygen reduction activity as a function of both oxygen and hydroxyl binding energies for various metals. Reprinted with permission from Nørskov, J. K., Rossmeisl, J., Logadottir, A., Lindqvist, L., Kitchin, J. R., Bligaard, T. & Jónsson, H. Origin of the overpotential for oxygen reduction at a fuel-cell cathode. *J. Phys. Chem. B*. **108**, 17886–17892 (2004). Copyright 2004 American Chemical Society.

While the DoE Pt loading target for 2020 was set to 0.125 mg cm^{-2} at both electrodes

(equating to ca. 6-9 g/vehicle), the Pt loading at the anode can be kept low around ca. 0.05 mg cm^{-2}, owing to the fast kinetics of the HOR.[26,27] However, there is almost a 10-fold increase in the amount of Pt required for the sluggish ORR kinetics at the cathode (ca. 0.3-0.5 mg cm^{-2}).[28] This has been a significant factor driving the research for optimizing Pt utilization and boosting the performance of PEMFC catalysts thereby reducing costs. Moreover, the catalyst and its applications make up to 41% of the overall PEMFC stack cost, compared to other components, which reinforces the significance of Pt loading within PEMFCs. [8,26,29]

There has been a great effort to eliminate platinum group metal (PGM) catalysts due to their cost and scarcity, so PGM-free catalysts have been explored. However, these PGM-free catalysts do not yet meet the benchmark activity and performance set by PGM catalysts.[9] Currently, Pt-based catalysts are the best catalysts for the ORR however, they are susceptible to oxidation and dissolution when exposed to high potentials, low pH values, and high temperatures.[30,31] Although it is quite stable, Pt dissolution in acidic media can proceed as follows:[19,32,33]

$$Pt \rightarrow Pt^{2+} + 2e^{-} \ \ (Pt\ dissolution) \qquad E^0 = 1.18\ V_{SHE} \tag{1.3}$$

$$Pt + H_2O \rightarrow PtO + 2H^{+} + 2e^{-} \ \ (Pt\ oxide\ formation) \qquad E^0 = 0.98\ V_{SHE} \tag{1.4}$$

$$PtO + 2H^{+} \rightarrow Pt^{2+} + H_2O\ (Chemical\ dissolution\ of\ PtO) \tag{1.5}$$

Equations (1.3 – 1.4) represent the loss of Pt activity during PEMFC operation via electrochemical dissolution and irreversible oxide formation, respectively. Equation (1.5) shows the dissolution of the Pt oxide which results in the Pt^{2+} ions dissolving in the electrolyte. These pathways result in a reduced electrochemical surface area (ECSA) for Pt and diminish the long-term stability of

the electrocatalyst performance.[34]

1.3.1 Carbon Supports for Pt Catalysts

To improve upon the electrocatalyst performance in PEMFCs, a material on which Pt nanoparticles (NPs) can be evenly dispersed is required. The most common support material for Pt is carbon black which has been applied to the cathode and anode for the ORR and the HOR, respectively. While there are other forms of carbon available such as activated carbon and graphene, carbon blacks are the most studied and accepted form of carbon. Carbon blacks are inexpensive and readily prepared from the partial pyrolysis of hydrocarbons. Investigations involving diffraction and transmission electron microscopy (TEM) techniques determined that carbon blacks were a mix of graphitic layers consisting of single layers to multiple layers.[35] A model of these materials is shown in Figure 1.3 which describes carbon black particles as aggregates formed from arrangements of spherical particles assembled concentrically from turbostratic graphitic domains.

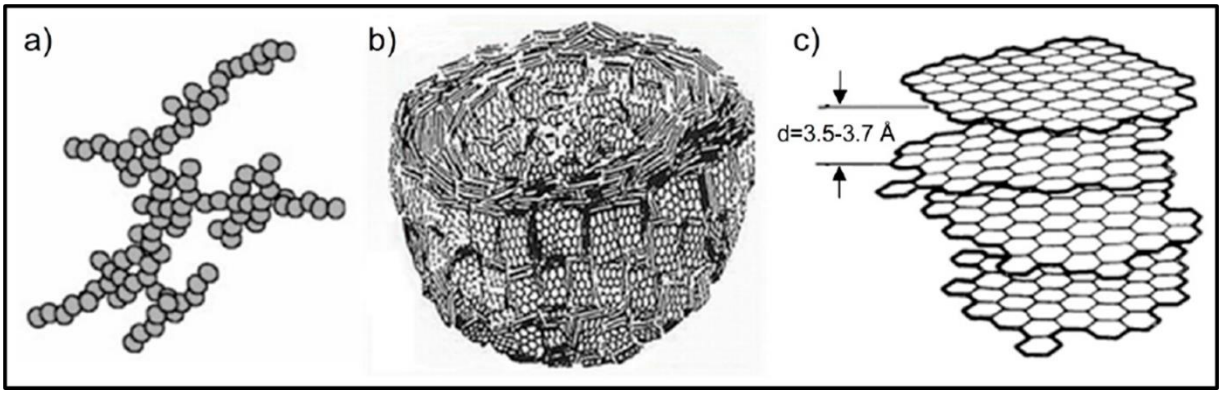

Figure 1.3. Multiscale model representing carbon black comprised of (a) aggregates constructed from (b) spherical carbon black particles assembled concentrically from (c) turbostratic graphitic layers. Reproduced from Jurkiewicz, K., Pawlyta, M. & Burian, A. Structure of Carbon Materials Explored by Local Transmission Electron Microscopy and Global Powder Diffraction Probes. C. 4, 68 (2018).

These carbonaceous materials are desirable because they are inexpensive, good electrical conductors, and possess a large surface areas which enhance Pt utilization.[32,36–38] The incorporation of a catalyst support material introduces interactions between the support and the Pt NPs that stabilize and enhance the catalytic performance of Pt. A variety of commercially available carbon black include Vulcan XC-72, Ketjen Black, and Black Pearls. These typically range in particle size from 30 - 100 nm with varying surface areas between ca. 200 – 2000 $m^2 g^{-1}$ allowing them to support the smallest Pt NP sizes of ca. 2-5 nm.[36,39–41] Among these carbon black materials, Vulcan XC-72 is the most common as it highly graphitic yet also possess a higher concentration of nucleation sites that promote better Pt dispersion. There are two common techniques for preparing Pt/C catalysts: (i) the impregnation method and (ii) the colloidal method.[38] The impregnation method involves the preparation of a slurry consisting of a Pt salt (ie. chloroplatinic acid, H_2PtCl_6) with the carbon support which is then dried to evaporate off any solvent followed by heat-treatment to reduce the resulting powder to the desired catalyst structure. On the other hand, the colloidal method describes the adsorption of a platinum metal colloid onto the surface of the desired carbon support.

Under acidic conditions, high potential and temperature, carbon supports undergo oxidation due to a low standard electrode potential, E^0, for the carbon/carbon dioxide redox couple:[42–45]

$$C + 2H_2O = CO_2 + 4H^+ + 4e^- \qquad E^0 = +0.207\ V_{RHE} \tag{1.6}$$

Especially when exposed to high potentials for startup and shutdown (SU/SD) tests which can reach as high as 1.6 V_{RHE}, the carbon support oxidizes to CO and CO_2 rendering the Pt catalyst unsupported and inactive (see example in Figure 1.4).[39,44,46] The unsupported Pt NPs generally

form agglomerations which impacts the ECSA thereby decreasing cell performance. Thus, it is imperative to design corrosion-resistant support materials to achieve low Pt loadings while maximizing Pt utilization and enhancing cell performance.

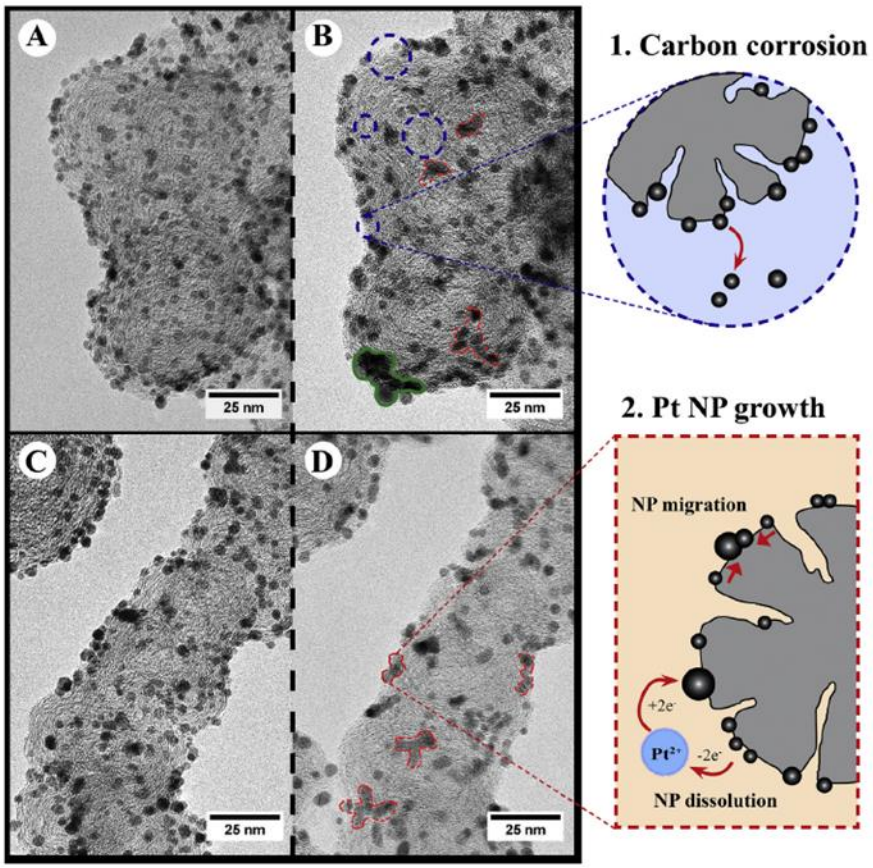

Figure 1.4. Platinum NP degradation mechanisms observed via TEM images for 30 wt% Pt/Ketjen black before and after AST protocols (A,B – 27,000 potential cycles between 1.0-1.5 V_{RHE}, 500 mV s^{-1}; C,D – 9,000 potential cycles between 0.6-1.0 V_{RHE} with a retention time of 3.3 s). The blue circles indicate regions of carbon corrosion where the Pt NPs are left unsupported and the red circles indicate Pt agglomerations. Reprinted from Speder et al. *J. Power Sources*. **261**, 14–22 (2014). Comparative degradation study of carbon supported proton exchange membrane fuel cell electrocatalysts – The influence of the platinum to carbon ratio on the degradation rate. Reproduced with permission from Elsevier B.V.

1.3.2 Metal Oxide Supports

To achieve corrosion-resistant materials, the first step is to seek carbon-free support materials which would serve to reduce costs by mitigating corrosion and improving the stability of the catalyst and catalyst support. Selection criteria for PEMFC supports outlined by Zhang et al. (2014) suggests supports should (i) exhibit high stability in acidic media, (ii) exhibit resistance to electrochemical corrosion, (iii) be good conductor of electrons and protons, and (iv) possess high surface area. According to these criteria, metal oxides such as titanium oxides (TiO_x), tungsten oxides (WO_x), niobium oxides (NbO_x), and molybdenum oxides (MoO_x), stand out as suitable support materials in PEMFCs.[47–52] Since their first use in the electrochemical photolysis of water, metal oxides have been closely studied in many catalysis applications.[53–55] Compared to carbon, the most appealing feature of metal oxides as electrocatalyst supports is their overall inertness to electrochemical and chemical corrosion. While metal oxides offer a very stable and durable solution for replacing carbon, they are semiconductors and as such, have wide band gaps and low electrical conductivity.

1.3.3 Titanium Oxide Supports

Titanium oxides are of particular interest as a catalyst support because they are inexpensive, abundant, and environmentally friendly. Titanium oxides introduce corrosion resistance via strong metal-support interactions (SMSI) between the Pt NPs and TiO_x support which enhances catalytic performance toward the ORR.[51,56–58] These SMSI serve to anchor Pt to the support and prevent dissolution or agglomeration of the catalyst NPs. The SMSI between Pt and TiO_2 clusters were explored via quantum mechanical calculations by Hepel et al. (2007) which demonstrated the net reduction in band gap between the HOMO and LUMO energy levels as Pt

formed bonds with the O atoms or Ti atoms in TiO_2.[59] While Pt/TiO_2 catalysts do exhibit good durability and some catalytic activity, TiO_2 on its own is a poor conductor and possesses a smaller surface area than most carbon materials. As such, it does not make for a practical fuel cell catalyst support. However, by altering the composition of TiO_2 supports, it is possible to achieve better conductivity, activity, and higher surface areas. One such example has been reported by Huang et al. (2011) through doping TiO_2 with Nb to form the $Pt/Nb_xTi_{(1-x)}O_2$ catalyst which displayed higher stability and ORR activity after potential cycling compared to a commercial Pt/C catalyst.[60] Figure 1.5 shows the stability of the Pt NPs supported by $Nb_xTi_{(1-x)}O_2$ which remained relatively stable and exhibited no signs of Pt dissolution or support corrosion over the course of a 2,500 cycle accelerated durability test (ADT) which was swept between 0.6 to 1.4 V at 50 mV s^{-1}.

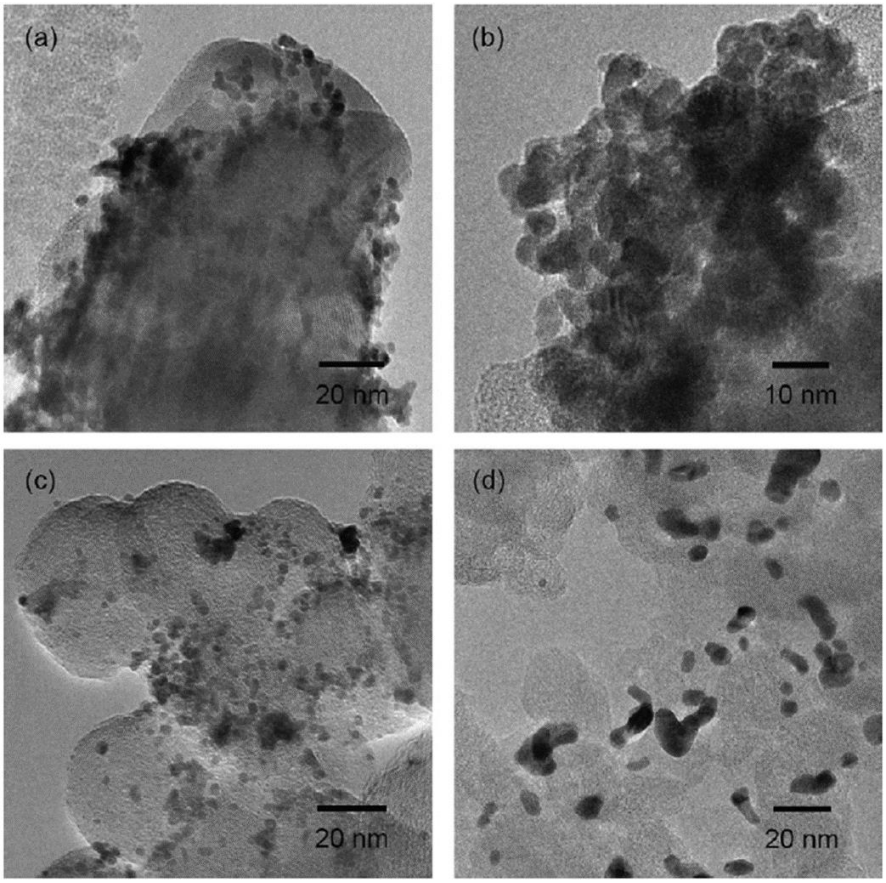

Figure 1.5. TEM images of (a,b) $Pt/Nb_xTi_{(1-x)}O_2$ and (c,d) commercial Pt/C catalysts before and after a 2,500 potential cycle ADT, respectively. Reprinted from Huang et al. Appl. Catal. B Environ. 96, 224–231 (2010). Electrocatalytic activity and stability of niobium-doped titanium oxide supported platinum catalyst for polymer electrolyte membrane fuel cells. Reproduced with permission from Elsevier B.V.

1.3.4 Conductive Titanium Sub-Oxide Catalyst Supports via Modification of TiO_2

PEMFCs require highly conductive support materials, therefore, it is necessary to improve upon the conductivity of TiO_2 if its durability and stability as a catalyst support are to be exploited for use as fuel cell catalyst supports. A common approach is to reduce TiO_2 under high temperatures ($400\ K < T < 1470\ K$)[61,62] in the presence of a reducing agent which improves crystallinity and produces lattice defects (ie. oxygen vacancies) which substantially lower the band gap and enhance the electronic conductivity. The resulting material is a "sub-oxide" of TiO_2

that follows the Ti_xO_{2x-1} formula ($3 \leq x \leq 20$). Within this range of suboxides, Ti_2O_3, Ti_3O_5, and Ti_4O_7 are the most common.[63] This class of metal oxides displays exceptional thermal and oxidative stability, resistance to corrosion and stability in acidic media, as well as good electronic conductivity. Ti_3O_5 and Ti_4O_7 have been heavily studied for their superior electronic conductivities up to 1,000 S cm^{-1} which is governed by several factors such as synthesis conditions, particle size, and temperature.[64–69]

To further enhance the conductivity of TiO_2 supports, the titania lattice can be doped with various transition metals such as Nb[70,71], Mo[72,73], Ta[23], and Ru[74,75]. Doping the TiO_2 lattice structure not only lowers the temperature requirements to produce suboxide phases, but it also increases the electronic conductivity by creating vacancies within the lattice which serve as electron recombination centers which reduces the band gap. Esfahani et al have reported molybdenum (Mo) doped TiO_2 to produce a Ti_3O_5-$Mo_{0.2}$ (TOM) catalyst support which exhibited adequate electrocatalytic performance due to the SMSI and substantially larger conductivity.[73] Despite this, the band gap improved only marginally, 2.6 eV down from 3.2 eV for TiO_2, which is impractical for PEMFC applications. To improve upon the TOM support conductivity and band gap, silicon (Si) was considered as a second dopant (hereafter referred to as TOMS, Ti_3O_3-$Mo_{0.2}Si_{0.4}$) due to its high stability, low cost, and successful incorporation into the catalyst layer to promote SMSI.[76–78] Addition of Si to the TOM support significantly narrowed the band gap to 0.31 eV and improved the conductivity as well.[79,80] The TOMS support demonstrated good SMSI with the Pt catalyst and enhanced the Pt activity toward the ORR and the methanol oxidation reaction.[81,82] Figure 1.6 shows the performance of the Pt/TOMS catalyst before and after a 5,000 potential cycle AST. The elemental distribution of Pt, Ti, Mo, and Si remained unchanged and

stable over the course of the test illustrating the superior retention of catalytic performance during accelerated stress tests (ASTs) compared to the commercial Pt/C catalyst.[79]

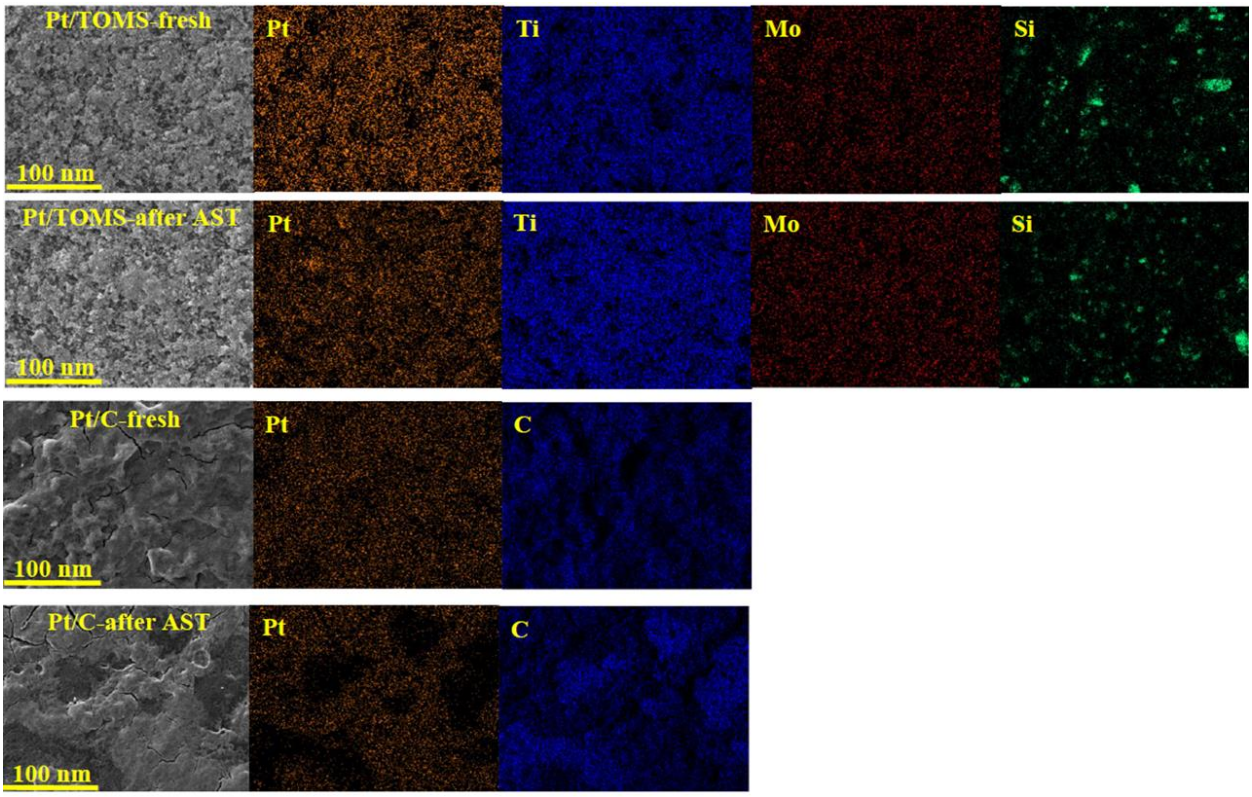

Figure 1.6. SEM images coupled with EDX mapping demonstrating the durability of the Pt/TOMS electrocatalyst before and after ASTs. A commercial Pt/C electrocatalyst was included for comparison. Reproduced from Esfahani et al. J. Mater. Chem. A. 6, 14805–14815 (2018). A fuel cell catalyst support based on doped titanium suboxides with enhanced conductivity, durability, and fuel cell performance. Reproduced with permission from the Royal Society of Chemistry.

1.4 Electrochemical Characterization Techniques

Analysis of these titanium suboxide support materials and electrocatalysts with electrochemical characterization techniques provides insight on the ECSA on which electrochemical reactions occur. They also make it possible to evaluate the overall performance and durability of these materials under various FC operating conditions. By comparing these

results with commercial electrocatalyst materials it is possible to determine the suitability of the titanium suboxide supports and electrocatalysts for fuel cell applications.

1.4.1 Cyclic Voltammetry

Cyclic voltammetry is a valuable technique that can be used to obtain both qualitative and quantitative information about the electrochemical processes occurring at the electrolyte/electrode interface. These processes include reaction reversibility, reaction mechanisms, electrochemical kinetics, and electrocatalytic processes. Cyclic voltammetry is often the first experiment performed when studying a material owing to its versatility.[83] These experiments are either performed *ex-situ* (outside of a fuel cell) or *in-situ* (inside a fuel cell). *In-situ* experiments involve an anode which serves as both the counter electrode (CE) and reference electrode (RE) to which H_2 gas is fed, and the cathode which is taken to be the working electrode (WE) and flushed with an inert gas (ie. N_2 gas).[84] *Ex-situ* experiments on the other hand, involve individual CE, WE, and RE immersed in a 3-electrode half-cell containing an electrolyte solution.

The ideal cyclic voltammetry response for conductive metal oxides is presented in Figure 1.7a with sharp transitions between the forward and reverse scans indicating ideal capacitance. During experimental conditions however, mass transport (ie. electrons and ions) and diffusion of ions in the electrolyte introduce series resistance to the system which causes the cyclic voltammogram (CV) response to deviate from ideality Figure 1.7b.[85,86] Furthermore, the double layer current is expressed as, I_{DL}, which presents as a 'baseline'. Increases in current above this established baseline, I_{Excess}, are attributed to the charge transfer that occurs at the electrode-electrolyte interface, particularly from the electrochemistry between the redox couple of the studied system.

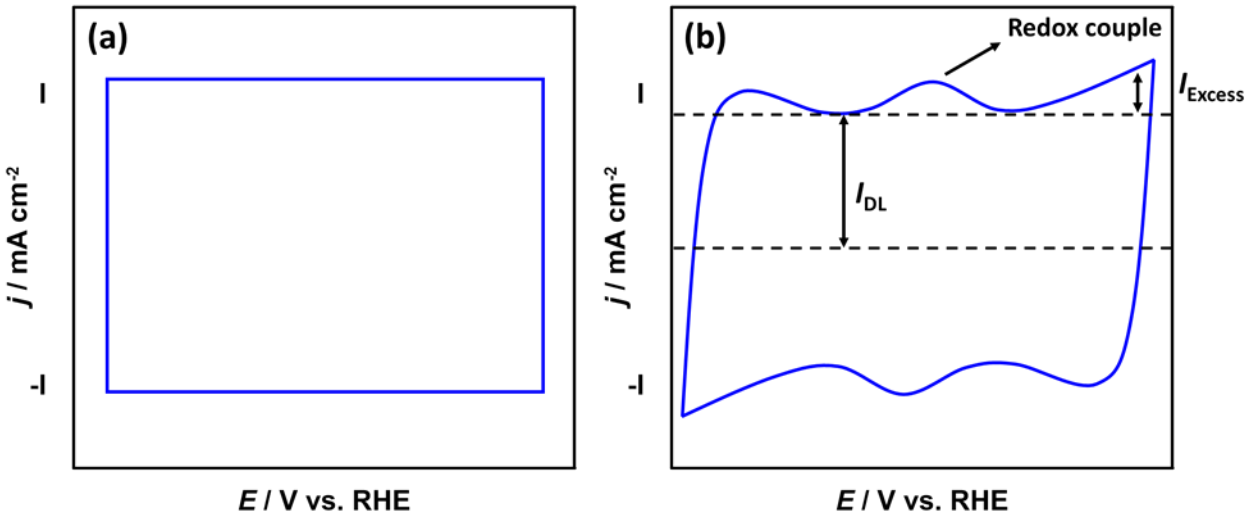

Figure 1.7. (a) Ideal half-cell CV response for conductive metal oxide. (b) Real (non-ideal) half-cell CV response which reflects series resistance and resistance due to mass transport.

1.4.2 Electrochemical Impedance Spectroscopy

Electrochemical impedance spectroscopy (EIS) is a powerful diagnostic tool that provides a wealth of information regarding the internal resistance and capacitance of electrochemical systems.[87–92] In principle, impedance is described as the AC response of an electrochemical system to an applied AC signal.[93] Simply put, it is the measure of a circuit's ability to resist the flow of an applied electric current. Resistivity is defined by Ohm's law as the relationship between voltage and current:

$$R = \frac{V}{I} \tag{1.7}$$

where R is resistance in Ohms (Ω), V is the voltage in volts (V), and I is the current in amperes (A).[92]

Real electrochemical systems have both resistive and capacitive properties. The response to a sinusoidally varying voltage is described by the impedance. The real part of the impedance

is the resistance, corresponding to the in-phase response, while the imaginary part of the impedance is proportional to the inverse of the capacitance, corresponding to the response 90 degrees out of phase. To consider resistance in terms of the AC component (sinusoidal voltage wave), Equation (1.7) must be rewritten as:

$$Z = \frac{V}{I} \tag{1.8}$$

where Z represents the impedance of electron flow due to the presence of a capacitor or resistor in the circuit. Applying the sinusoidal component to the voltage produces Equation (1.9):

$$V(t) = V_{max}\ sin\ \sin(\omega t + \theta) \tag{1.9}$$

where *V(t)* represents the instantaneous voltage at an instance of time *t* (s); V_{max} is the peak amplitude of the sinusoidal voltage in volts (V); ω represents the angular velocity (rad/s); and θ is the phase angle.[93] Since the angle revolves in one cycle at 2π radians, a substitution for ω can be made in Equation (1.9) to produce Equation (1.10):

$$V(t) = V_{max}\ sin\ \sin(2\pi f t + \theta) \tag{1.10}$$

By the same convention, the sinusoidal current can be written as:

$$I(t) = I_{max}\ sin\ \sin(2\pi f t + \phi) \tag{1.11}$$

where *I(t)* is the instantaneous current value at an instance of time *t* (s); I_{max} is the amplitude of the sinusoidal current (A); ϕ is the phase angle; and *f* is the frequency (Hz).[93] Now the electrical resistance of an AC circuit, AC impedance, can be written in the form of Ohm's law as follows:

$$Z = \frac{V(t)}{I(t)} \tag{1.12}$$

where V(t) and I(t) are the measure of potential and current within an AC system, respectively.[93]

In a sinusoidal, AC system, the AC impedance of a resistor, Z_{Res}, and a capacitor, Z_{Cap}, are expressed below:

$$Z_{Res} = R \tag{1.13}$$

$$Z_{Cap} = \frac{1}{i\omega C} \tag{1.14}$$

where *i* is an imaginary number $\sqrt{-1}$ and *C* is capacitance in Farads (F).[92,93] When considering total contribution of impedance, $Z_{R/C}$, to an electrochemical system from an AC resistor and AC capacitor in parallel, the following expression is obtained:

$$\frac{1}{Z_{\frac{R}{C}}} = \frac{1}{Z_{Res}} + \frac{1}{Z_{Cap}} \tag{1.15}$$

$$Z_{\frac{R}{C}} = R + \frac{1}{i\omega C} \tag{1.16}$$

$$Z = Z' + Z'' \tag{1.17}$$

where Z’ is the real impedance (resistive component) and Z’’ is the imaginary impedance (capacitive component).

The electrochemical interface between the PEMFC electrode and electrolyte can be considered as a collection of electrical elements, such as resistance, capacitance, and impedance, within an electric circuit.[93] To this effect, a simple finite transmission-line equivalent circuit was developed by the Pickup group to generate more insight toward the electrode-electrolyte interface (Figure 1.8).[41,86–90]

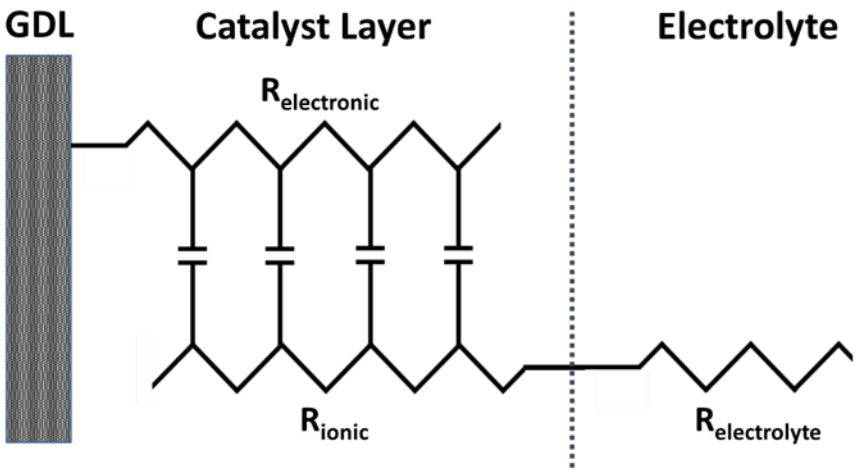

Figure 1.8. Diagram of the simple finite transmission-line equivalent circuit model to illustrate the electrochemical impedance of a PEMFC electrode.[87]

The equivalent circuit model describes ionic resistance, R_{ionic}, as the transport of ions through the catalyst layer, while describing electronic resistance, $R_{electronic}$, as the transport of electrons through the conductive catalyst support. Together, these two components serve as parallel resistive rails connected by capacitors (the catalyst sites) which are assumed to evenly distribute the capacitance across the catalyst layer. From here, two assumptions can be made: 1) $R_{electronic}$ is assumed to be negligible relative to R_{ionic} due to the highly conductive nature of the catalyst[91]; 2) resistance from the electrolyte, $R_{electrolyte}$, can be neglected since it would only shift the plot along the real axis[89]. If the total catalyst layer resistance, R_{Σ}, is equivalent to the sum of $R_{electronic}$ and R_{ionic} ($R_{\Sigma} = R_{ionic} + R_{electronic}$) and if the contribution of $R_{electronic}$ is considered negligible, then $R_{\Sigma} = R_{ionic}$ which allows the impedance response to be fit to any ionic conductivity profile.[89]

1.5 Polarization Curves

The standard electrochemical method for assessing fuel cell performance involves a plot of cell potential versus current density which is useful for characterizing performance losses in the PEMFC applications.[94] The electrical energy produced by a fuel cell is governed Gibbs free

energy, $\Delta G = -nFE^o$, where n is the number of electrons transferred per molecule during the reaction, F is Faraday's constant, and E^o is the standard cell potential.[94] Under standard conditions, the anode potential is 0.0 V (hydrogen oxidation reaction is zero at all temperatures)[95] and the cathode potential is 1.229 V. Under open circuit potential (OCV) conditions, when there is no current flowing, the difference between the anode and cathode potentials is 1.229 V. Under load conditions the cell potential is lower and influenced by cell operating conditions like temperature, gas flow rates and relative humidity. Practically speaking, this difference of 1.229 V shifts to much lower values between ca. 850 – 950 mV and continues to do so with increasing current density as illustrated by Figure 1.9. This initial potential drop observed in a polarization curve is primarily due to activation overpotential for the sluggish kinetics of the ORR at low current densities. These losses are also influenced by hydrogen crossover from the anode to the cathode and mixed potentials arising from Pt-O formation occurring at the cathode.[94]

Beyond the potential drop, several types of irreversible losses occur cause deviation from ideality. The first being activation losses or overpotential, which are a result of the sluggish kinetics observed for the ORR. Generally, these losses are not observed past 100 mA cm^{-2} and can be minimized by utilizing high surface area catalyst to facilitate the reactions and improve activity.[94–96] The second type is Ohmic loss which arises primarily from ionic resistance within the membrane however the electrocatalyst and support materials contribute to additional electronic resistance. To mitigate or minimize internal resistance, effective water management is required: not enough water will result in poor proton conduction, too much water will flood the catalyst layer inhibiting gas transport.[97] At higher current densities, performance loss is due to mass transfer where there is a deficiency of reactant transferred to the catalyst sites. Rather, the

reactant is consumed at the same rate it is transferred to the electrode surface. This typically results from restricted oxygen flow to the catalyst sites in the event of catalyst layer flooding and can be minimized by increasing oxygen flow rate.

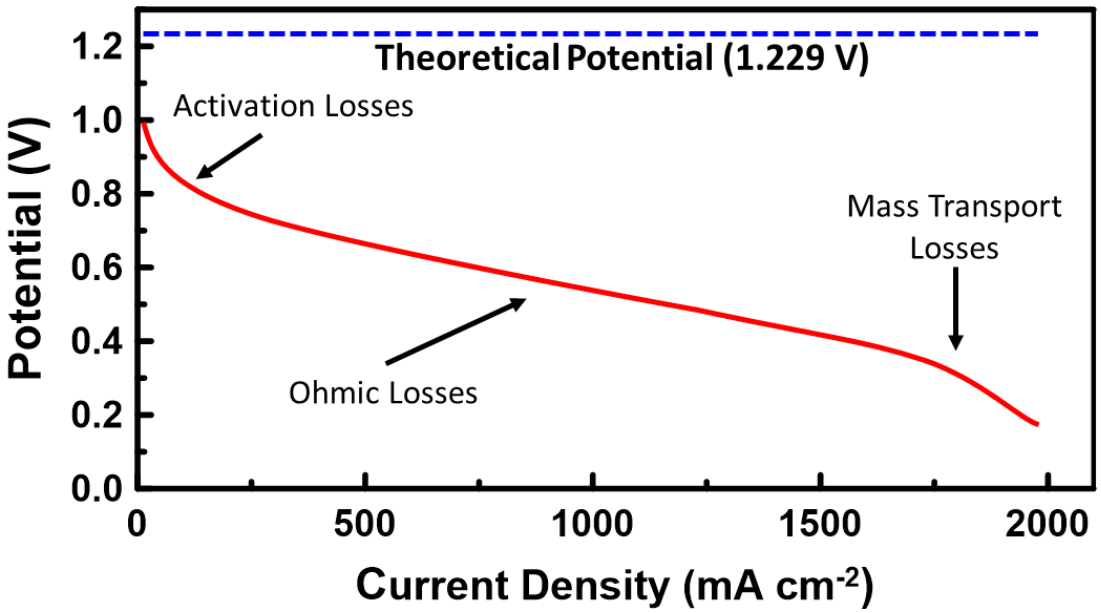

Figure 1.9. Typical Polarization Curve for PEMFCs showing the 3 main limitations affecting the overall performance, compared to the ideal polarization curve.

1.6 Thesis Objective

While metal oxides are not very conductive materials, they have demonstrated exceptional stability to corrosive environments and, through modification, improved electron conduction. As with the TOM support, it was shown that doping the TiO_2 structure with Mo could mildly reduce the band gap to 2.6 eV however, it remained a poor conductor of electricity making it nonideal for PEMFC applications. It was demonstrated through the TOMS support that the addition of Si reduced the band gap to 0.31 eV and was associated with a higher conductivity and improved catalytic activity. Considering that Si showed the greatest impact in lowering the bandgap of the TOMS support, one may question whether Mo is in fact needed or not to create

a conductive metal oxide support. Furthermore, while testing with TOMS did not show any leaching of Mo, the long-term oxidative stability of Mo is still a concern. In contrast, Si and SiO_2 have been shown to be highly corrosion stable.[96,98,99] Thus, the motivation of this thesis is to investigate the impact of Si-doped TiO_2, in the absence of Mo, to produce the Ti_3O_5-Si (TOS) support. This will allow us to better understand the influence of Si on the physical and electrochemical properties of the support materials.

This thesis consists of 5 chapters: Introduction, Materials/Methods, Results, Optimization of the TOS Support Surface Area, and Conclusions and Future Work. Chapter 1 consists of an introduction to FC technology, PEMFCs, and the challenges which must be overcome for commercialization of these devices. Various electrode support materials are explored thereafter with a focus on metal oxides as corrosion-resistant replacements for carbon supports commonly used for Pt-based catalysts. This section concludes with an introduction to doped metal oxides to serve as conductive catalyst supports which are the basis of this Master's research project. Chapter 2 describes the materials and methods necessary for synthesis and characterization of the TOS support and Pt/TOS catalysts. Chapter 3 reports the results of physical and electrochemical characterization of the TOS supports and Pt/TOS catalysts. The TOS supports are compared to previously synthesized TOM and TOMS supports whereas the Pt/TOS support is benchmarked against a commercial Pt/C catalyst with a variety of electrochemical tests including ADTs, ASTs, and ORR activity via RDE experiments. Chapter 4 involves refining the TOS support surface area through ball milling as well as a novel sol-gel synthetic approach to achieve higher surface area and better ORR activity. This dissertation concludes with Chapter 5 which is a summary of the results presented and discusses the results of a fuel cell station test on the final

Pt/TOS catalyst compared to Pt/TOMS, Pt/C, and a catalyst from literature, Pt/Nb-TiO_2.

Chapter 2: Materials and Methods

2.1 Chemicals

Titanium (IV) oxide, anatase (TiO_2, 325 Mesh), Titanium tetrachloride ($TiCl_4$) 99.9%, poly(ethylene glycol)-block-poly(propylene glycol)-block-poly(ethylene glycol) (Pluronic®123, average molar weight 5800), and Silicon powder (Si, 325 mesh) $\geq$ 98% were purchased from Sigma Aldrich. Isopropanol 99.50% purity (Fisher Scientific), Sulfuric acid (H_2SO_4) 95 – 98% purity (ACP Chemicals), Nafion® perfluorinated resin solution 5 wt% (DuPont), acetonitrile (CH_3CN) 99.8 wt%, 20% Pt on Vulcan XC-72 (Premetek). Compressed gases including H_2 (99.999%), N_2 (99.998%), and air (extra dry) were purchased from Praxair. All aqueous solutions were prepared using ultrapure water obtained from a Millipore Milli-Q system with resistivity >18 mΩ cm^{-1}.

2.2 Synthesis of TOS support and Pt/TOS catalyst

The titanium suboxide was prepared by doping commercial TiO_2 anatase with Si particles. TiO_2 was dispersed in a solution of ultrapure water and isopropanol (65:35 vol.%), to which 5wt% Pluronic® P123 surfactant was added. Resulting solution was left to stir for 5 h under ambient temperature, followed by the addition of appropriate ratio of Si to the solution. This solution was left to stir for 12 hours under ambient temperature to obtain a homogenous mixture and then left to air dry and evaporate off the solvents. Finally, this mixture was annealed at 1000 °C (heating rate of 10 °C min^{-1}) for 5 h in a reducing atmosphere of H_2:N_2 10:90 vol% to obtain a final powder product hereafter referred to as TOS.

The reaction scheme for the synthesis of the 20 wt% Pt/TOS catalyst is shown in Figure 2.1. The Pt/TOS catalyst was prepared by combining 100 mg of TOS support powder with 100 mL of ultrapure water which was left to stir for 1 h under ambient temperature to obtain a uniform

mixture. Meanwhile, a solution made from 42 mg $H_2PtCl_6 \cdot 6H_2O$ (corresponding to 20 wt% Pt) dissolved in 10 mL ultra-pure water was added dropwise to the TOS-containing solution. Following a stirring period of 2 h, the solution was purged with H_2 gas for 1 h and then sealed and left to stir for 24 h. The resulting mixture was filtered, washed, then dried at 80 $°C$ in an N_2 atmosphere to evaporate off the solvents. This was followed by heat treatment at 450 $°C$, at a heating rate of 5 $°C$ min^{-1}, for 4 h under a reducing atmosphere (H_2:N_2 10:90 vol%). The resultant product is hereafter referred to as Pt/TOS.

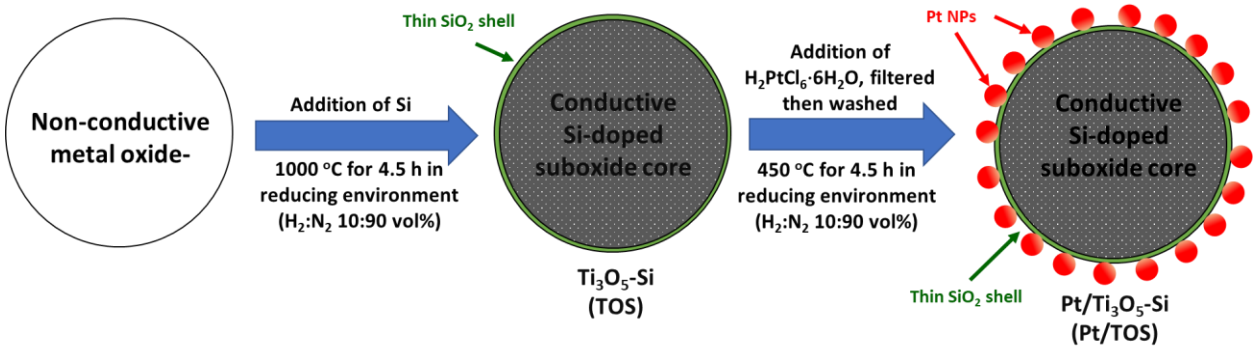

Figure 2.1. Reaction schematic for the synthesis of the TOS support and Pt/TOS catalyst.

2.3 Support and Catalyst Ink Preparation

The supports and catalysts were evaluated electrochemically as thin films and were obtained from the appropriate catalyst inks prepared as a mixture of 3:1 ultrapure water and isopropanol, a solution of 5 wt% Nafion®, and 5-7 mg of support/catalyst powder. This mixture was sonicated for 10 minutes until homogenous and then left to stir for 12 hours. To acquire the desired thin film, support and catalyst loadings of 0.020 mg cm^{-2} were deposited onto the surface of a GC electrode (0.07 cm^2) which was dried with a heat gun on low heat.

2.4 Physicochemical Characterization

2.4.1 X-Ray Diffraction

To identify the composition and crystalline phases of the catalyst supports, X-Ray diffraction (XRD) measurements were performed. Samples were scanned through 2θ = 10° to 100° and the XRD patterns were obtained using a Rigaku Ultima IV X-ray diffractometer with a Cu K_α radiation source (λ = 0.15418 nm). All data was analyzed using PANalytical X'Pert HighScore software. The Debye-Scherrer equation (Equation (2.1) was used to estimate catalyst crystalline size along (h k l) profile, d (in nm), based on the XRD scan. Where *k* is a dimensionless shape factor generally taken to be 0.9, λ is the wavelength of X-ray of Cu K_α radiation in nm, β is the full width at half maximum (FWHM) of the (h k l) peak in radians, and θ is the Bragg angle in radians.

$$d_{(h\,k\,l)} = \frac{k\,\lambda}{\beta\ cos\ cos\ \theta} \tag{2.1}$$

2.4.2 UV-vis Spectroscopy, Optical Band Gap, and Electronic Conductivity

To obtain the UV-vis spectra of the TOS support powder samples, a PerkinElmer Lambda 750S UV-vis Spectrophotometer equipped with a 60 mm integration sphere was used. The UV-vis absorption spectra were recorded using the Lambda 750S Scan software. The absorption spectra reveal information about the electronic transitions involved within the sample structure. Manipulating the absorbance spectra to obtain the diffuse reflectance, $R = 10^{-Absorbance}$, allowed for the Kubelka-Munk equation to be applied which, in its basic form shown below, describes the "diffuse illumination of the particulate coating" in paint coatings[100,101]:

$$F(R) = \frac{K}{S} = \frac{(1-R)^2}{2R} \tag{2.2}$$

where *F(R)* represents the Kubelka-Munk function, K is the absorption coefficient and S is the scattering coefficient.[101]

To describe the behaviour of light traveling inside metal oxide samples, the Kubelka-Munk equation can be applied in a similar fashion to paint coatings through modification by multiplying the energy of the excitation source, $h\nu$, scattered by the metal oxide particles to produce $(F(R) \cdot h\nu)^n$. The variable '*n*' represents the coefficient for the associated electronic transition (usually taken to have a value of 2 for semiconductors) and $h\nu = \frac{1240}{wavelength}$, where $h\nu$ is in eV and *wavelength* is in nm.[101] From this, a Tauc plot was obtained by plotting the modified Kubelka-Munk function against $h\nu$. The x-intercept of each Tauc plot was extrapolated and offered a good estimation of the optical band gap (in eV).

Electronic conductivity is the reciprocal of resistance and is the measure of a material's ability to conduct electric current across a given distance. To obtain the resistance data, the individual support powders were first pressed between two copper disks (12 mm diameter, 0.21 mm thickness) at 65 kg cm^{-2} for 90 s to form pellets with a thickness of 1.16 ± 0.2 mm. The pellets were then placed within a two-point probe and the resistance across the pellet was measured. The data was collected as a plot of potential along the independent axis and current density along the dependent axis. Due to the inverse relationship of the resistance and conductivity, the slope of the curve directly revealed the electronic conductivity across the TOS pellets. By dividing the electrical conductivity by the measured thickness of the pellets, the pellet electrical conductivity could be inferred. While these properties will appear to have a positive correlation, it is important to note the electronic conductivity is a measure of the interparticle/grain interactions within the

support and band gap energy is a property derived from the bulk material and diffuse reflectance of scattered light. In other words, the band gap energy is a measure of how well the material can conduct electrons, and the electronic conductivity quantifies the current flow through the material.

2.4.3 Scanning Electron Microscopy and Energy Dispersive X-Ray Spectroscopy

To probe the morphology and atomic composition of all support surfaces, Scanning Electron Microscopy (SEM) was performed using a Hitachi FlexSEM 1000 system coupled with an Energy Dispersive X-ray (EDX) spectroscopy analyzer. Powder samples were pressed onto a 1 cm^2 square of copper tape and adhered to a standard SEM stub. SEM images were collected at an accelerating voltage of 10 kV over a range of various magnifications at different sample sites.

2.4.4 Transmission Electron Microscopy

Transmission electron microscopy (TEM) images were obtained from Dr. Carmen Andrei (McMaster University) using a JEOL 2010F Field emission gun operated 200 kV and coupled with an Oxford Inca EDS system.

2.4.5 Brunauer-Emmett-Teller Surface Area Analysis

The Brunauer-Emmett-Teller (BET) surface area measurements of each sample were collected using a Quantachrome Instruments NOVA 1200e Surface Area & Pore Size Analyzer. All samples were degassed for 4 hours at 150 ^oC to remove any contaminants on the surface. After this period of degassing, samples were placed in the adsorption chamber of the BET instrument and subjected to a liquid N_2 atmosphere at 77 K. The nitrogen adsorption and desorption isotherms were obtained using 60 points and all data was analyzed with NovaWin software.

2.5 Half-cell Electrochemical Characterization

2.5.1 Cyclic Voltammetry for Accelerated Durability Tests

For the CV experiments, three-electrode half-cells were employed with a WE, CE, and RE. In the typical half-cell set up, the WE is an electrical conductor comprised of a glassy carbon or gold disk, encased in insulative material. It is critical to maintain the cleanliness of the electrode surface, where the electrochemical processes of interest occur. To ensure the electrode surface was clean, it was mechanically polished on a polishing pad with a water-alumina slurry; polishing in a figure-eight motion ensured the polishing, and ultimately the surface, remained even. After polishing, the electrode surface was sonicated in ultrapure water to remove any remaining particles. A potentiostat was used to modulate the external voltage applied through the WE to the electrode surface where the electrochemical processes of interest would occur. The RE provided a reference point against which the potential of the WE can be measured in an electrochemical cell. Since the RE material does not change, the potential was fixed which implied any potential changes in the system were related to processes occurring at the surface of the WE.[92] The CE served to complete the circuit when a voltage was applied to the WE.

CVs for the ADTs were collected on a Solartron 1470 Multichannel Potentiostat which was controlled using multistat software (Scribner Associates). To perform measurements, the WE was scanned from 0.05 to 1.25 V vs RHE (V_{RHE}) at a rate of 500 mV s^{-1} for 20,000 cycles. At the end of every 1000th cycle, 3 additional cycles were scanned between 0.05 – 1.25 V_{RHE} at a sweep rate of 200 mV s^{-1}, which were to be used for data analysis. This protocol, illustrated in Figure 2.2, was used assess support stability under extended duration of time.

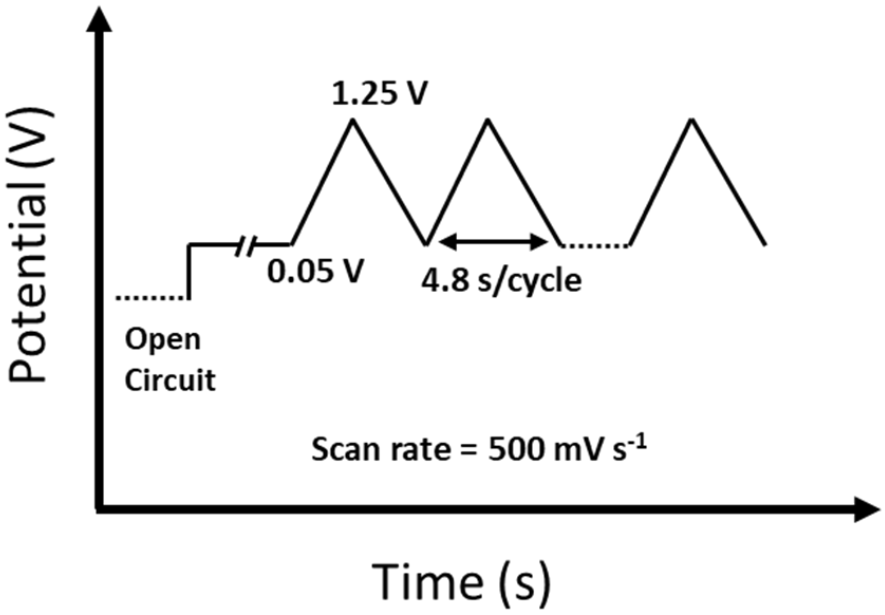

Figure 2.2. The ADT protocol used for the evaluation of catalysts and catalyst supports over 20,000 cycles, which employs a triangular waveform between 0.05-1.25 V_{RHE} at a scan rate of 500 mV s^{-1}.

The ADT protocols were conducted using three-electrode half-cells in which a glassy carbon electrode (area = 0.07 cm^2) was used as the WE, graphite rod as the CE and, a Mercury-mercurous sulfate (Hg/Hg_2SO_4) as the RE (Figure 2.3). These electrodes were placed in 0.5 M H_2SO_4 (aq) solution which was purged with N_2 (g) for 10 min to displace any oxygen. The RE was calibrated prior to the ADTs in H_2-purged 0.5 M H_2SO_4 and the potential was determined to be 0.695 V_{RHE}.

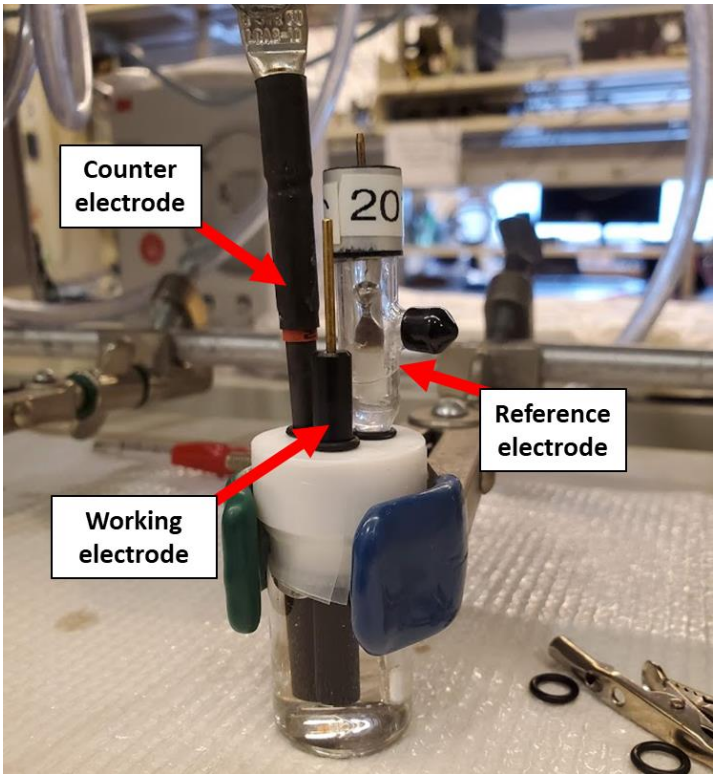

Figure 2.3. Three-electrode half-cell setup for the Solartron 1470 multichannel potentiostat with a working electrode, counter electrode, and reference electrode.

The ideal CV response for conductive metal oxides is presented in Figure 2.4a with sharp transitions between the forward and reverse scans indicating ideal capacitance. During experimental conditions however, mass transport (ie. electrons and ions) and diffusion of ions in the electrolyte introduce series resistance to the system which causes the CV response to deviate from ideality Figure 2.4b.[85,86] Furthermore, the double layer current is expressed as, I_{DL}, which presents as a 'baseline'. Increases in current above this established baseline, I_{Excess}, are attributed to the charge transfer that occurs at the electrode-electrolyte interface, particularly from the electrochemistry between the redox couple of the studied system.

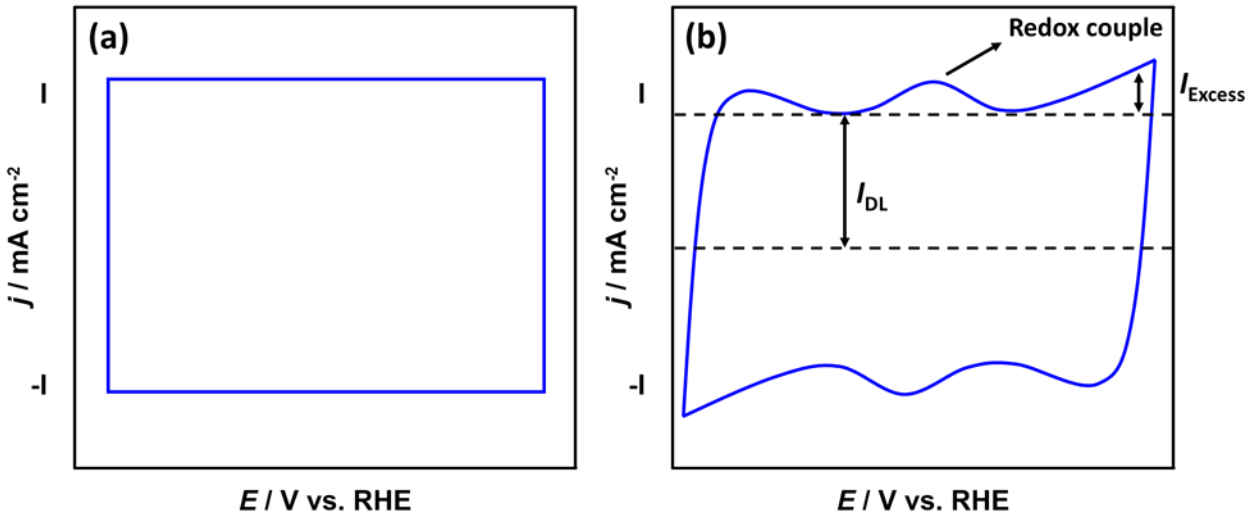

Figure 2.4. (a) Ideal half-cell CV response for conductive metal oxide. (b) Real (non-ideal) half-cell CV response which reflects series resistance and resistance due to mass transport.

Figure 2.5 represents characteristic features for the CV of Pt supported on TOS catalyst. In this figure, the regions labeled H_D and H_A represent characteristic peaks of hydrogen desorption and adsorption, respectively. The label DL refers to the double layer, Pt_{OX} refers to the Pt oxidation region where surface Pt atoms are oxidized to PtOH and finally to PtO, and Pt_{RED} refers to the PtO reduction to metallic Pt. Typically, the area under the H_D peak can be integrated to reveal total charge associated with hydrogen adsorption (it has been shown experimentally to reveal the same charge as that integrated above the H_A peak).[102] From this, the ECSA, or the amount of Pt available for electrochemical reactions, can be determined.[94] The ECSA ($m^2\ g^{-1}$) is calculated as follows[103,104]:

$$ECSA = \frac{Q_{des}}{(210 \mu C\ cm^{-2})(Pt\ loading)} \tag{2.3}$$

where Q_{des} represents the coulombic charge of hydrogen desorption ($\mu C\ cm^{-2}$), 210 µC cm^{-2} represents the coulombic charge required to oxidize one monolayer of hydrogen on the Pt surface, and Pt loading is the loading of metal on the surface of the electrode represented in mg

cm^{-2}. The ECSA is an important quantity because from it the electrode's ability to facilitate the ORR can be inferred. Generally, ECSA is measured with time to assess the durability of the Pt catalyst against degradation.

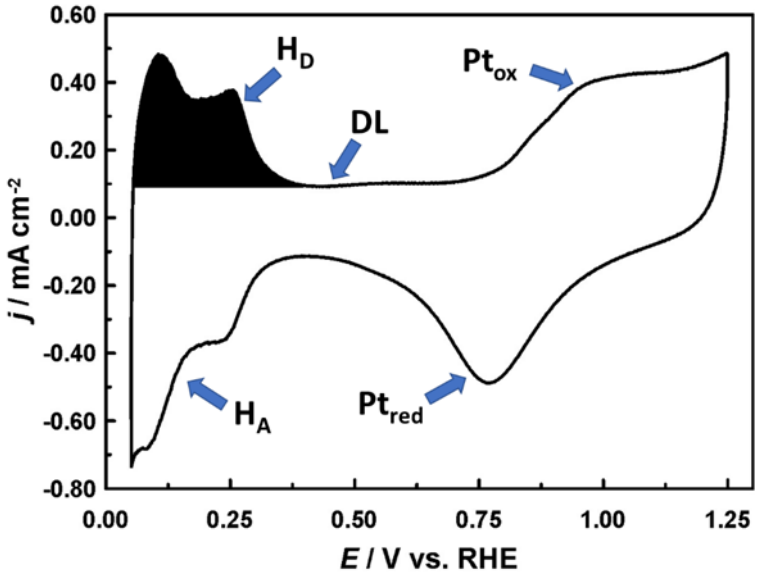

Figure 2.5. Half-cell CV of Pt supported on TOS (20 wt% Si) in 0.5 M H_2SO_4 (aq) solution. H_A and H_D represent regions of hydrogen adsorption and desorption, respectively, followed by DL which is the double layer in which no faradaic processes are expected to occur. Finally, Pt_{OX} and Pt_{RED} which correspond to the oxidation of Pt to form the PtO species and the subsequent reduction of PtO to Pt, respectively.

2.5.2 Accelerated Stress Tests

ASTs were conducted using the Solartron 1470 Multichannel potentiostat and involved an identical approach to the ADTs. In these experiments, a gold electrode (area = 0.03 cm^2) was used as the WE and 0.1 M H_2SO_4 (aq) was used as electrolyte. Following the DoE protocols[26], *ex-situ* load cycling ASTs and SU/SD ASTs were used to evaluate the integrity of the supports and Pt-supported catalysts under aggressive conditions. The load cycling AST (Figure 2.6a) involved simulating accelerated variations in the fuel cell load over the course of a drive cycle. This allowed

for evaluation of the integrity of the catalyst against Pt dissolution and agglomeration between 0.6 V (approaching maximum load conditions) and 1.0 V (near zero-load conditions). On the other hand, the SU/SD AST protocol (Figure 2.6b) simulated aggressive spikes in voltage between 1.0 and 1.5 V, during start-up and shutdown conditions. The SU/SD AST allowed for evaluation of accelerated support and catalyst corrosion during SU/SD conditions. Both AST protocols were performed *ex-situ* via a rectangular waveform, which was scanned from 1.0-1.5 V_{RHE} for 10,000 cycles with a retention time of 3 s in 0.1 M H_2SO_4. During each protocol, CVs were obtained every 1000th cycle and scanned from 0.05-1.25 V_{RHE} at a scan rate of 200 mV s^{-1} to assess any change to the catalyst layer.

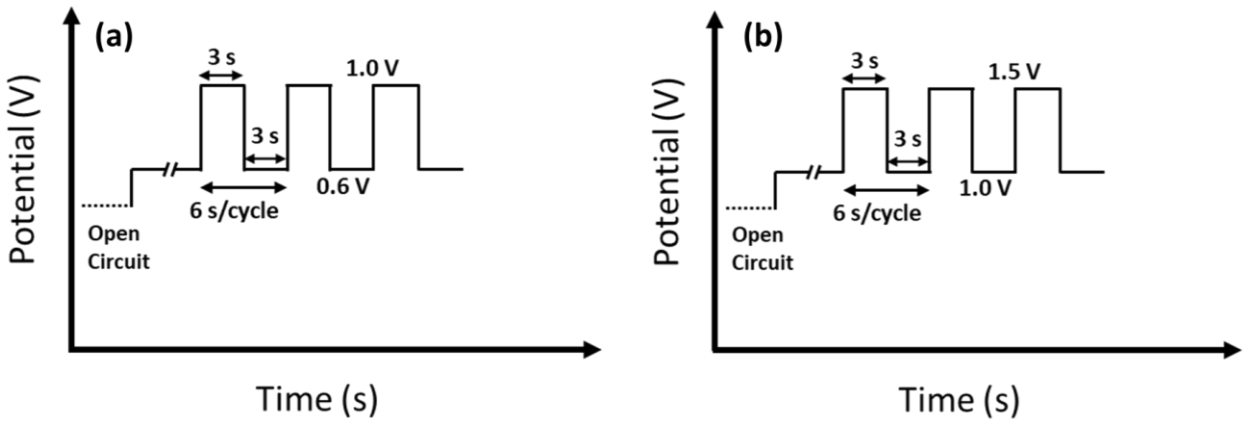

Figure 2.6. The (a) load cycling and (b) SU/SD AST protocols used to evaluate the stability and interactions between the catalyst and support.

2.5.3 Oxygen reduction reaction activity measurements

To investigate the activity of the Pt catalyst toward the ORR, rotating disk electrode (RDE) experiments were performed *ex-situ* with linear sweep voltammetry. The underlying principle of this technique is “forced convection” via rotation of the electrode to produce laminar flow of solution toward the surface of the electrode. This process is dependent upon the angular velocity

of the electrode which promotes controlled mass transport of the electrochemical redox species to the surface of the electrode. The redox species undergo their respective reduction and oxidation reactions at the electrode surface and the reaction kinetics in the presence of a varying electrode potential are revealed. Typical linear sweep voltammogram (LSV) response curves approach a limiting current which indicates the process is controlled by mass transport, as depicted by Figure 2.7.

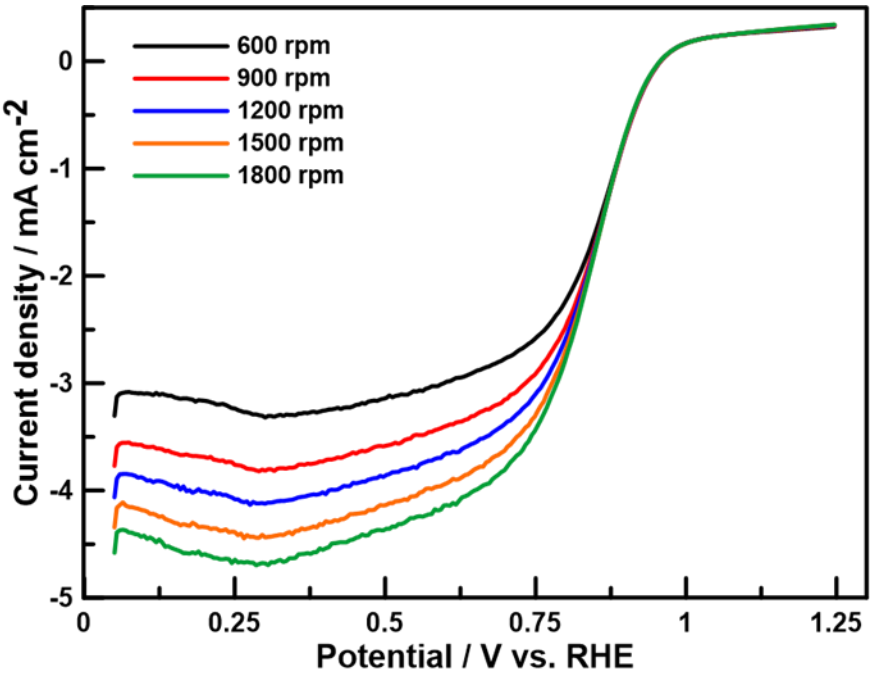

Figure 2.7. ORR LSV curves for Pt supported on carbon in saturated 0.5 M H_2SO_4 solution.

To investigate the activity of the Pt catalyst toward the ORR, rotating disk electrode linear sweep voltammetry was performed. These experiments were carried out using a Pine Instruments WaveDriver 20 bipotentiostat coupled with an MSR electrode rotator. Rotation of the rotating disc electrode (RDE) induced forced convection to control mass transport at the surface of the electrode. LSVs were recorded using 5 different rotation rates of 600, 900, 1200,

1500, and 1800 rpm in O_2-purged 0.5 M H_2SO_4 (aq).

2.5.4 Electrochemical Impedance Spectroscopy

EIS experiments were performed to understand the resistive and capacitive properties of the catalyst material. All electrochemical experiments were performed using a 1470 coupled to a 1260 Frequency Response Analyzer. The measurements were collected over a frequency range of 100 kHz to 0.1 Hz at a DC potential bias of 0.425 V_{RHE}. Under these conditions, it was possible to analyze the data via the finite transmission-line model which is useful for evaluating the durability of catalysts and catalyst supports.

Figure 2.8a is an experimental EIS response for the TOS support which shows a Nyquist plot constructed from the real impedance (Z') on the independent axis plotted against the imaginary impedance (Z'') on the dependent axis. Note the data begins near the origin of the figure at high frequencies and the Z' and Z" values increase, approaching lower frequencies. This is due to the nature of impedance which is a function of frequency which has an inverse relationship with time. Figure 2.9a shows the expansion of the Warburg region, or the mid-high frequency region, of the EIS response which ideally forms a 45° slope before increasing in Z'' toward a limiting capacitance, C_{lim}. The length of the Warburg region can be projected along the real impedance axis which is represented by $R_\Sigma/3$, where $R_\Sigma = R_{ionic}$, representing the total catalyst layer resistance. This is illustrated by the intersection of the dotted lines in Figure 2.9a.[93]

Using the Nyquist plots, a capacitance plot can be constructed, which is a function of resistance and is proportional to the ECSA of the electrode which is proportional to the ionic resistance of the electrode.[41,89] Recall, Equation (1.14), where the impedance of a capacitor in an AC system was expressed in terms of frequency and capacitance. Simple rearrangement of this

equation produces the expression for capacitance within an AC system:

$$C = -\frac{1}{\omega Z''} \tag{2.5}$$

This allows for capacitance to be plotted against the real impedance Figure 2.8b. The height of the curve, or where it begins to approach a limiting capacitance, is equal to the Warburg region when projected along the independent axis (represented by the dotted blue line in Figure 2.9b) which, more often than not, is easier to establish than with Nyquist plots.

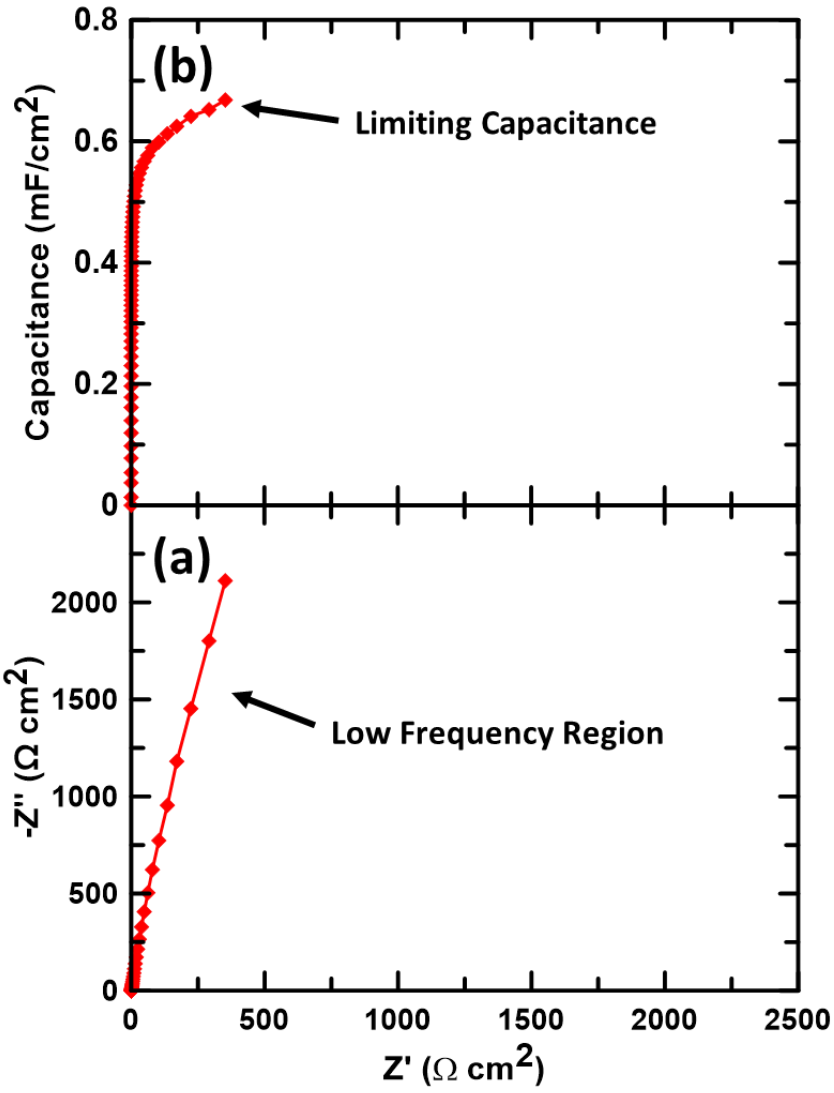

Figure 2.8. (a) Nyquist and (b) capacitance plots for the EIS response of the TOS support.

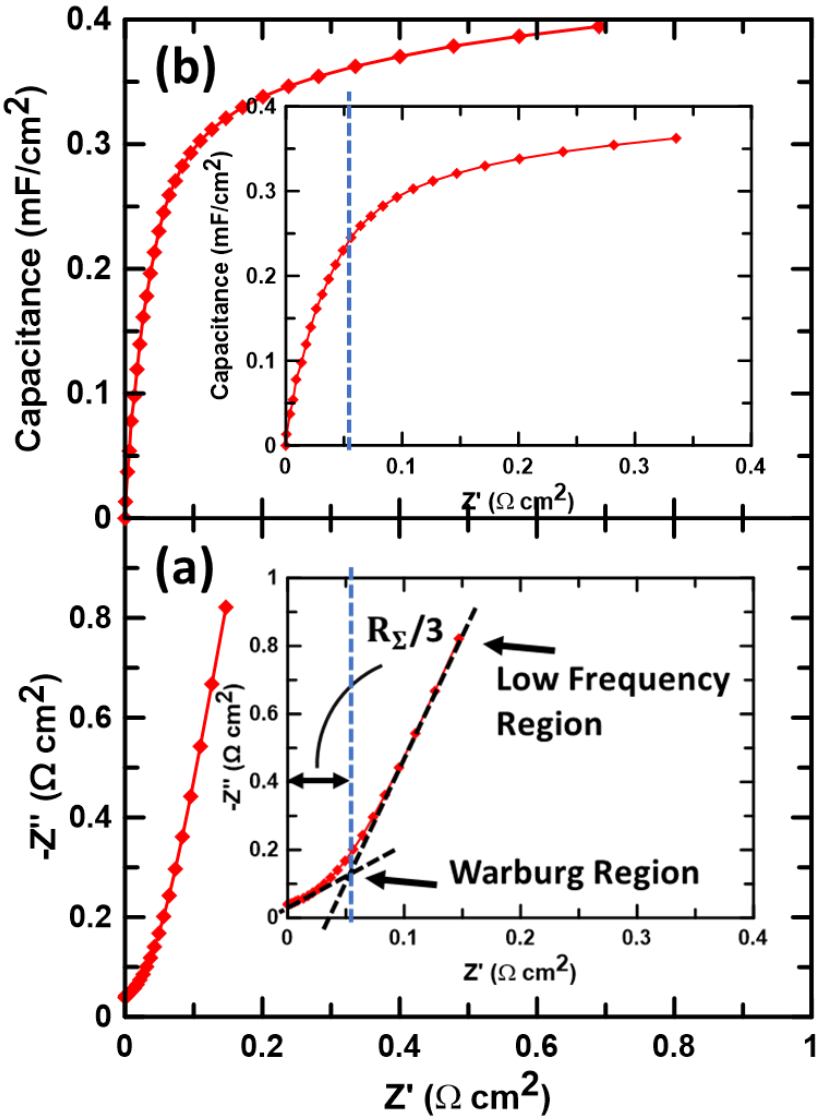

Figure 2.9. Expansion of the Warburg regions of the Nyquist (a) and capacitance (b) plots from Figure 2.8. The insets in (a) and (b) have been magnified on the real impedance axis to offer better visualization of the Warburg region. The intersection of the two black dotted lines (represented by the blue line) indicates the Warburg length.

2.6 MEA Fabrication and Single Cell Fuel Cell Testing

To evaluate the activity and performance of Pt/TOS, a MEA was fabricated and subjected to electrochemical testing in a single cell fuel cell test (FCT) station (Fuel Cell Technologies). MEA fabrication began with spray deposition of the catalyst inks onto separate carbon cloth gas

diffusion layers (ETEK ELAT) with target Pt loadings of 0.20 mg cm^{-2} and 30 wt% Nafion®. These gas diffusion electrodes (GDE) were then dried at 80 ^{o}C for 6 h and punched into 5 cm^2 sections. Finally, a Nafion® NRE-212 membrane was sandwiched between the two GDEs where the Pt/TOS GDE was used at the cathode side and the Pt/C GDE was used at the anode side. This assembly was set between two aluminum plates within a hot-press pre-set to 110 ^{o}C and then pressed at 150 kg cm^{-2} for 90 s. The resulting MEA was tested in a 5 cm^2 cell (Fuel Cell Technologies) using a Fuel Cell Technologies single cell test station and compared to a similar MEA with Pt/C GDE at both the anode and cathode. Reactant gases H_2 and O_2 were fed to the anode and cathode, respectively, while the backpressure of each was controlled via backpressure regulators installed at the outlet of each gas. Backpressure was maintained at 1 bar throughout all measurements and the flow rate of H_2 and O_2 were 100 and 200 mL min^{-1}, respectively and temperature was maintained at 80 ^{o}C. LabView software was deployed to control experimental parameters.

Chapter 3: Investigating Titanium Suboxide Supports Doped with Silicon

In this chapter, TiO_2 will be doped with varying concentrations of Si to assess the influence of Si on the resulting suboxide structure, in the absence of Mo. The resultant TOS supports will be optimized for Si content and characterized via physical and electrochemical characterization techniques. It is expected that an increase in Si concentration will promote the reduction of TiO_2 to its suboxide phases which are known to be more conductive and possess conductor-like band gaps. Once the Si concentration is optimized, the TOS support will be platinized, Pt/TOS and its performance toward the ORR and intensive AST protocols will be evaluated.

3.1 Materials Characterization

3.1.1 X-Ray Diffraction

To determine the crystallographic structure of the TOS supports as the Si content was increased, X-ray diffraction patterns were obtained (Figure 3.1). The patterns associated with the TOS supports containing 2 and 5 wt% Si were dominated by the semi-conductive rutile phase of TiO_2 (2θ = 27.87°) which is not ideal for electronic conduction. As the Si content was increased, the crystallographic structure favored the formation of Ti_3O_5 (ICDD Card 01-072-2101) with an intense reflection at 2θ = 25.45°. This phase transition typically occurs at temperatures well above 1000 °C, however, the presence of Si promotes the transition between 700-800 °C. This was to be expected since Ti_3O_5 is a polymorphic compound capable of several crystallization phases, one of which is an orthorhombic structure (*Cmcm* space group) in the {110} orientation and is achieved via reduction above temperatures of 480 K.[44,61,64,66,69,105,106] This reduction is expected to evoke metallic behavior within the suboxide according to semiconductor transition metal theory as seen in various metal oxide structures such as VO_2 and NbO_2.[61,105,107] The TOS 10

and 15 wt% Si supports contained a mixture of Ti_3O_5 and Ti_4O_7 (ICDD Card 001-071-1300) suboxide phases and retained the strong characteristic Ti_3O_5 reflection, while the TOS 20 wt% Si support primarily consisted of the Ti_3O_5 phase.

These data established titanium suboxide formation under a reducing environment in the increasing presence of Si. The stoichiometric reduction of Ti^{4+} to Ti^{3+} produced oxygen vacancies which can possess within them 2 electrons that exist in the band gap then delocalize into the conduction band contributing to the electrical conductivity of the suboxide.[108] Small amounts of metallic Si (ICDD Card 01-078-2500) and SiO_2 (ICDD Card 00-047-1300) existed throughout the Ti suboxide lattice structure and were identified by key reflections located at 2θ = 28.69° and 55.53°, respectively.

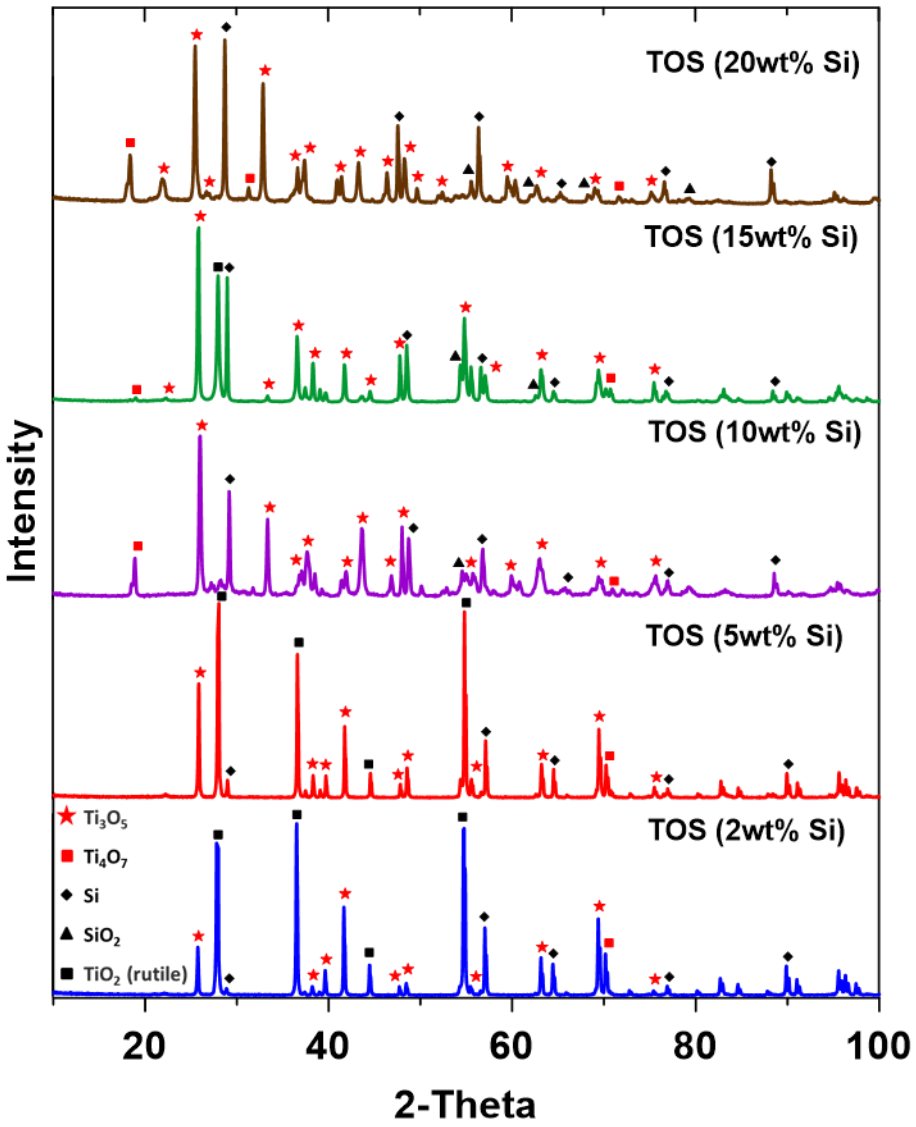

Figure 3.1. XRD patterns for the TOS supports with increasing Si content.

3.1.2 Optical Band Gap and Electronic Conductivity

To investigate the electronic properties of the TOS supports, the UV-Vis absorption spectra were measured. Through manipulation of the Kubelka-Munk equation[101,109–111], the absorption coefficients were obtained from the reflectance data and plotted against the energy of the excitation source to produce a Tauc plot. Figure 3.2 shows Tauc plots measured for commercial TiO_2 and the TOS supports of varying Si content. From the Tauc plot, band gap

energies could be visualized and estimated via the x-intercept of the linear fit.[100,112] As Si was introduced into the titania framework, the band gap of the TOS supports followed a slight narrowing trend, with as little as 2 to 5 wt% Si reducing the gap from 3.34 eV to 3.00 and 3.01 eV, respectively (Figure 3.3). While the 2 and 5 wt% Si supports possessed marginally lower band gap values relative to the TiO_2 precursor, they retained semi-conductive properties of the rutile phase, which is consistent with the XRD analysis. By increasing the Si concentration from 10 to 20 wt% Si, conductor-like band gap energies near that of pure Ti_3O_5 (ca. 0.50 eV) were achieved (Figure 3.3).[69] These band gap energies were substantially narrower than the measured band gaps of the commercial TiO_2 anatase and previously synthesized TOM support, 3.4 eV and 2.6 eV, respectively, while only marginally wider than the TOMS support band gap of 0.31 eV.[79,113] These narrow band gaps are a result of the oxygen vacancies that form within the crystalline lattice to serve as electron recombination centers.

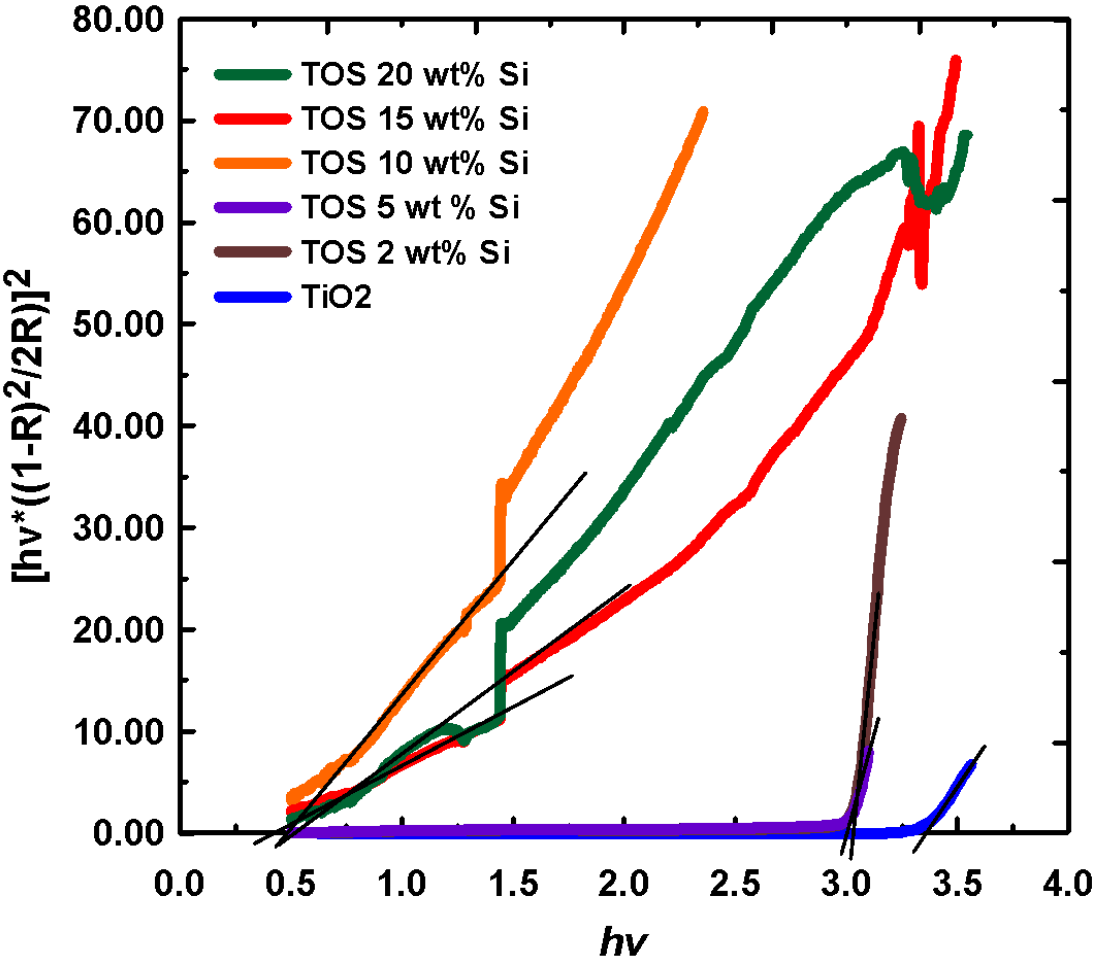

Figure 3.2. Tauc plot for the band gap energy determination of the TOS supports and commercial TiO_2.

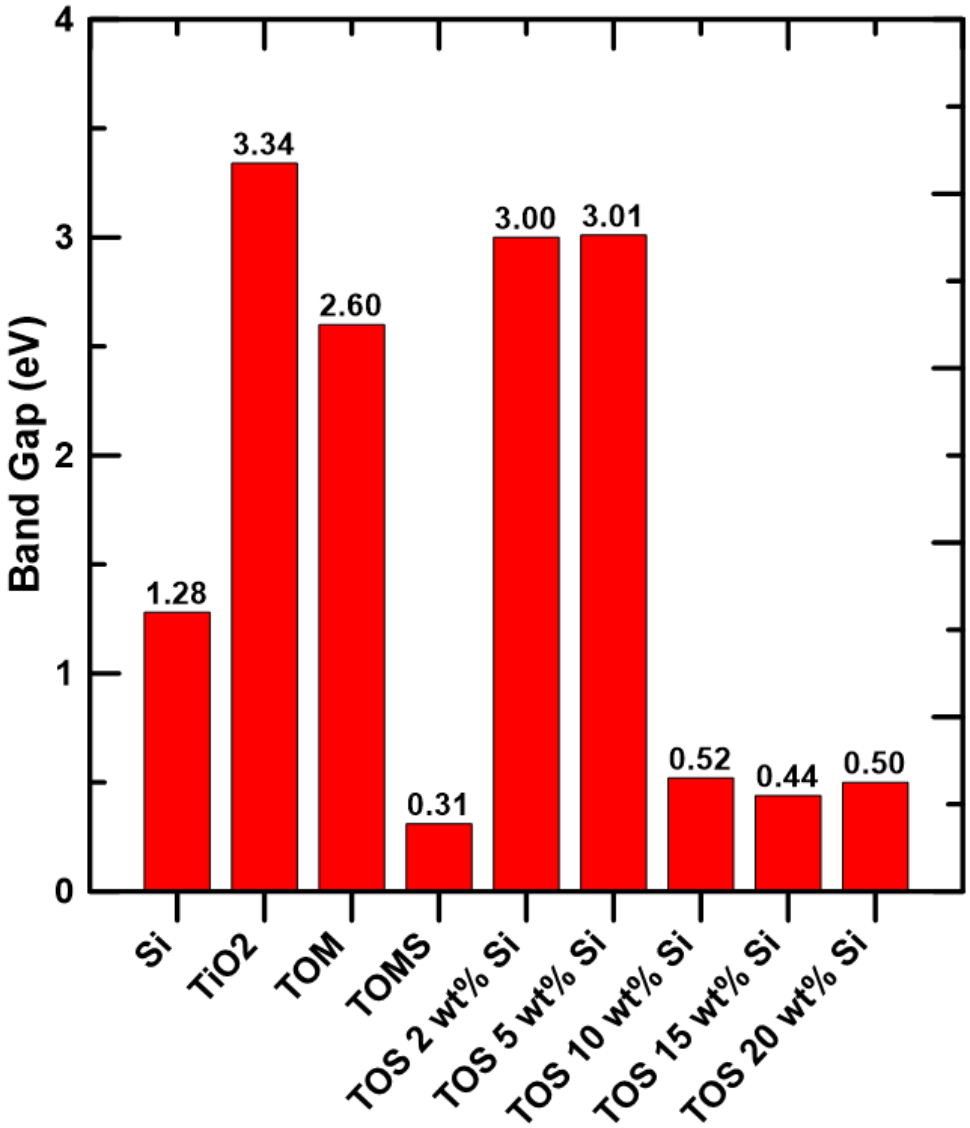

Figure 3.3. The band gap (in eV) measured against the varying amount of Si dopant introduced into the TOS support.

The electronic conductivity of sample pellets made from pressed powders was measured in a two-point probe. The electronic conductivity of the 2 and 5 wt% Si TOS supports was determined to be 1.52×10^{-10} and 7.20×10^{-10} S cm^{-1}, respectively, reflecting their wide band gap energies of ca. 3.0 eV (Figure 3.4). Generally, conductive supports should be greater than 5-10 times that of the membrane resistance, which can be around 0.1 S cm^{-1}. As such, materials

with conductivities below this threshold may not be suitable carbon replacements. The electronic conductivity of the TOS 10, 15, and 20 wt% Si supports was 0.79, 0.46, and 1.24 S cm^{-1}, respectively. This conductivity is a result of improved crystallinity owed to the successful transition from Ti^{4+} to Ti^{3+}, required for electron conduction, which can be recognized when the suboxide powder becomes black, or dark grey, in colour.[66,114] Additional literature has shown the successful incorporation of SiO_2 into the catalyst layer can enhance the conductivity.[115–118] These TOS supports display better electronic conduction than the previously synthesized TOM support (0.004 S cm^{-1}), while about one order of magnitude higher in conductivity than the TOMS support (0.11 S cm^{-1}) which indicates that Si as a single dopant is more effective than Mo. These conductivities indicate the support is approaching conductor-like conductivity, ie. carbon black (0.83 S cm^{-1})[20] and Ti_3O_5 (4.7 S cm^{-1})[69].

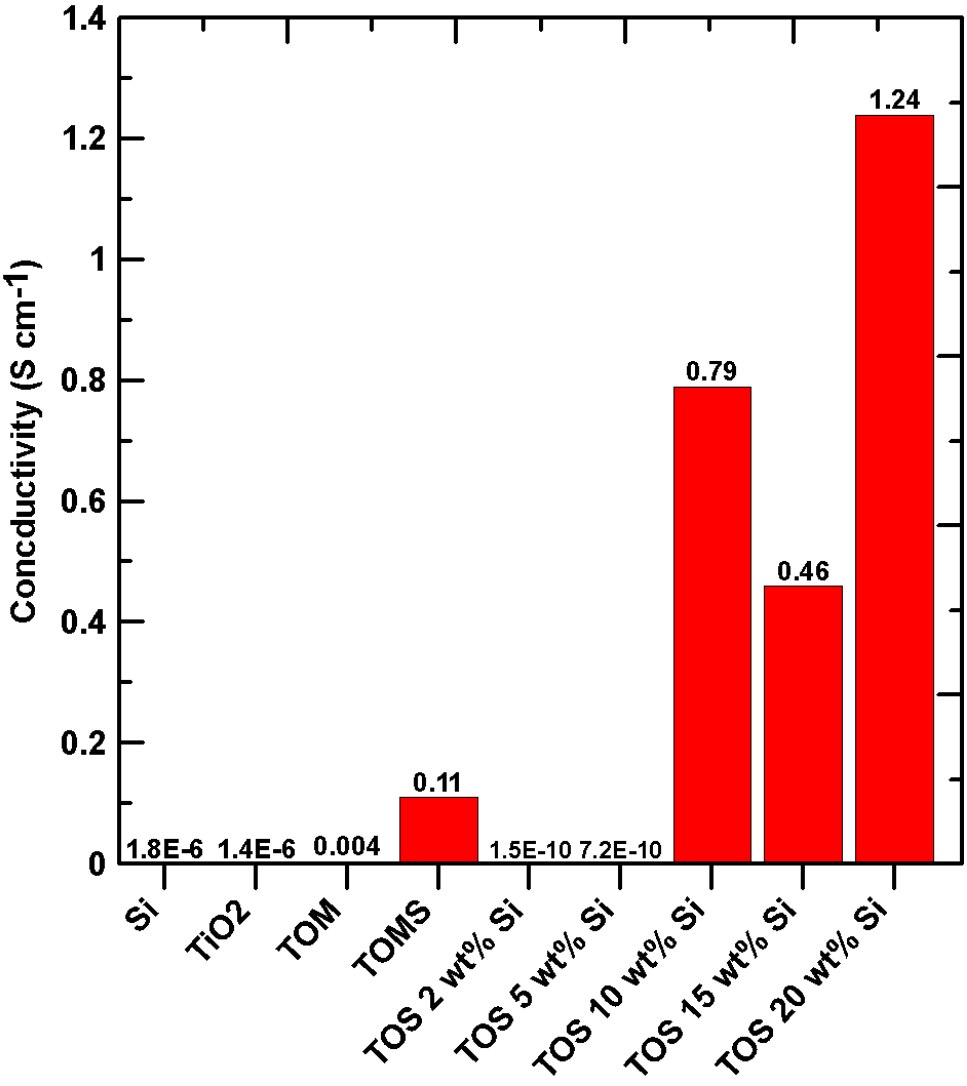

Figure 3.4. The electronic conductivity (in S cm^{-1}) measured against the varying amount of Si dopant introduced into the TOS support.

Table 3.1. Physical characterization of the TOS supports and precursor materials compared to the TOM, TOMS, and commercial Carbon black supports.

Support Material	Band gap (eV)	Conductivity (S cm^{-1})	Surface Area (m^2 g^{-1})	Cited Work
Carbon black	---	(0.83)[a]	232.2	[79]
Si	1.28	1.83×10^{-5}	5.5	This work
TiO_2	3.34	(1.4×10^{-6})[a]	13.2	[79]
Ti_3O_5	0.15	(4.7 – 30)[a]	---	[66,67,69]
Ti_4O_7	0.53	(1.03×10^{3})[a]	---	[68]
TOM	(2.6)[a]	(4.0×10^{-3})[a]	---	[119]
TOMS	(0.31)[a]	(0.11)[a]	---	[79]
TOS 2 wt% Si	3.00	1.52×10^{-10}	---	This work
TOS 5 wt% Si	3.01	7.20×10^{-10}	---	This work
TOS 10 wt% Si	0.52	0.79	29.8	This work
TOS 15 wt% Si	0.44	0.46	15.8	This work
TOS 20 wt% Si	0.50	1.24	17.8	This work

[a] *Referenced data*

3.1.3 Scanning Electron Microscopy, Transmission Electron Microscopy, and Energy Dispersive X-Ray Spectroscopy

To study the morphology and composition of the TOS supports, SEM in combination with EDX spectroscopy were deployed. The SEM images of the TOS 10, 15, and 20 wt% Si supports obtained in Figure 3.5 show surface homogeneity and even dispersion of Ti and O particles at ca. 5k magnification. However, the Si particles formed agglomerations as the concentration of Si was increased from 10-20 wt%. The EDX mapping in Figure 3.6 - Figure 3.8 accurately represent the TOS support elemental composition which presents with Si agglomerations (in green) ranging in sizes from 5-20 µm in diameter as the Si concentration was increased.

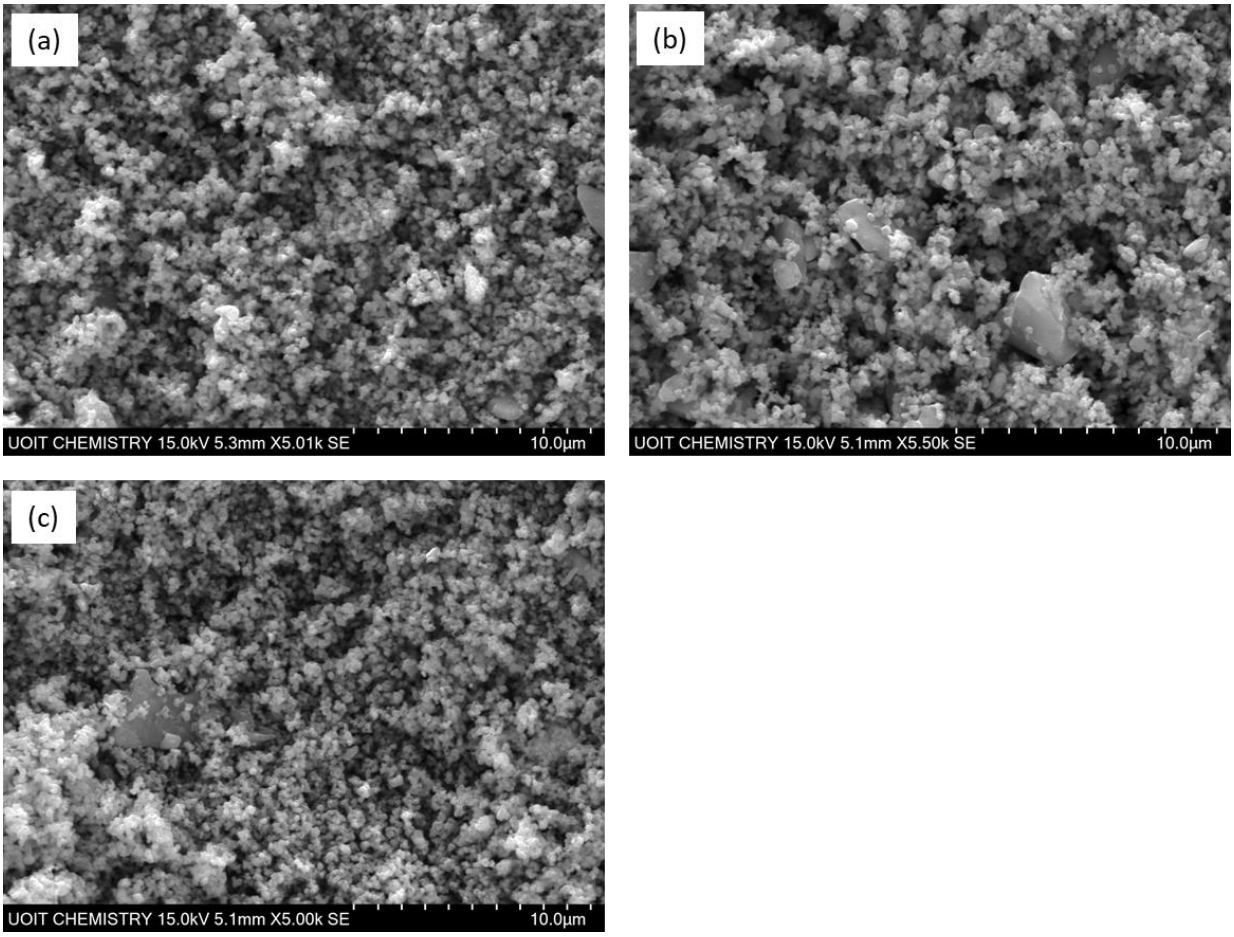

Figure 3.5. SEM images of the TOS supports with (a) 10 wt% Si, (b) 15 wt% Si, and (c) 20 wt% Si.

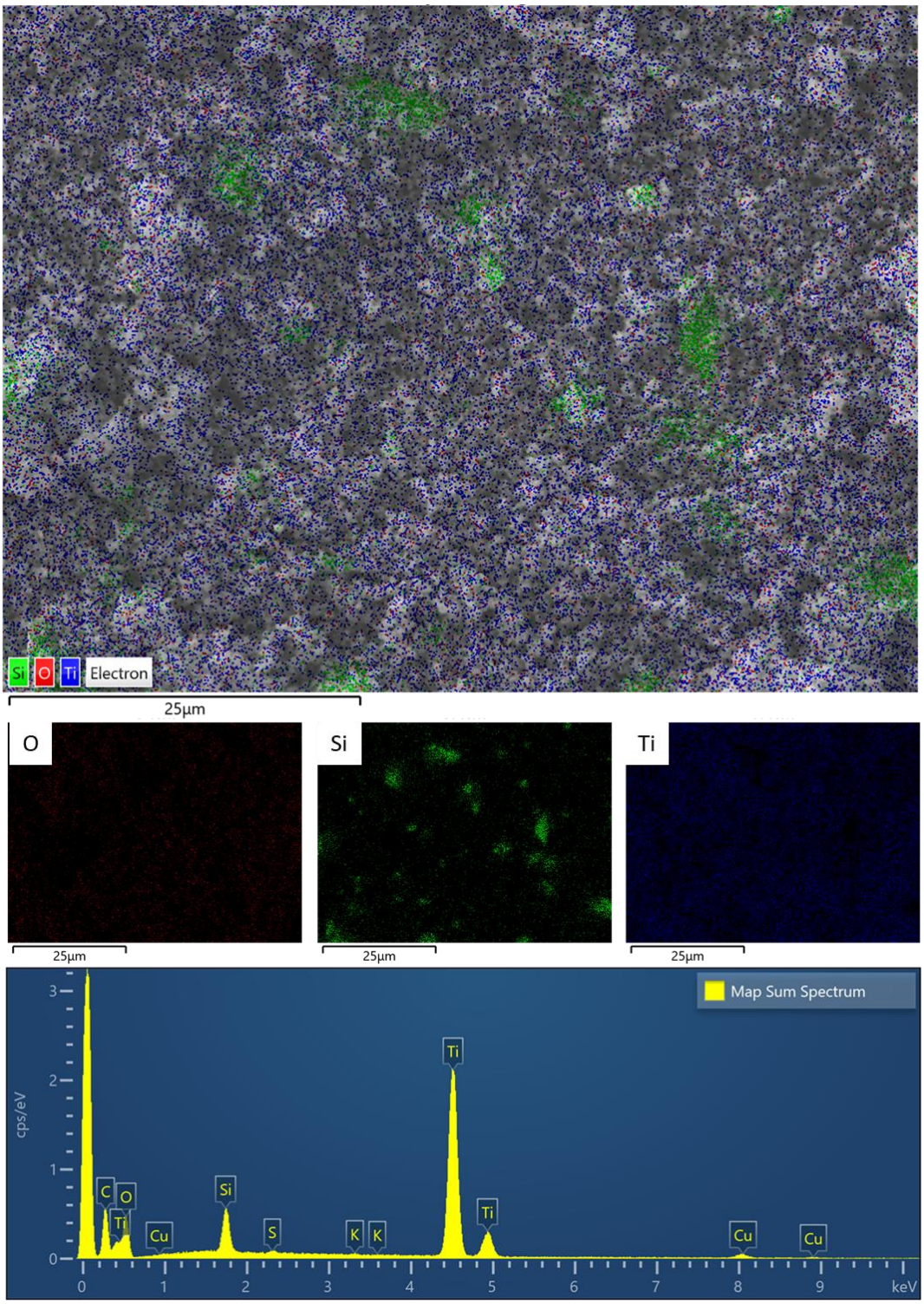

Figure 3.6. EDX analysis of TOS 10 wt% Si support represented as (a) overlay of EDX mapping on SEM image, (b) EDX mapping for individual elements, and (c) EDX elemental analysis.

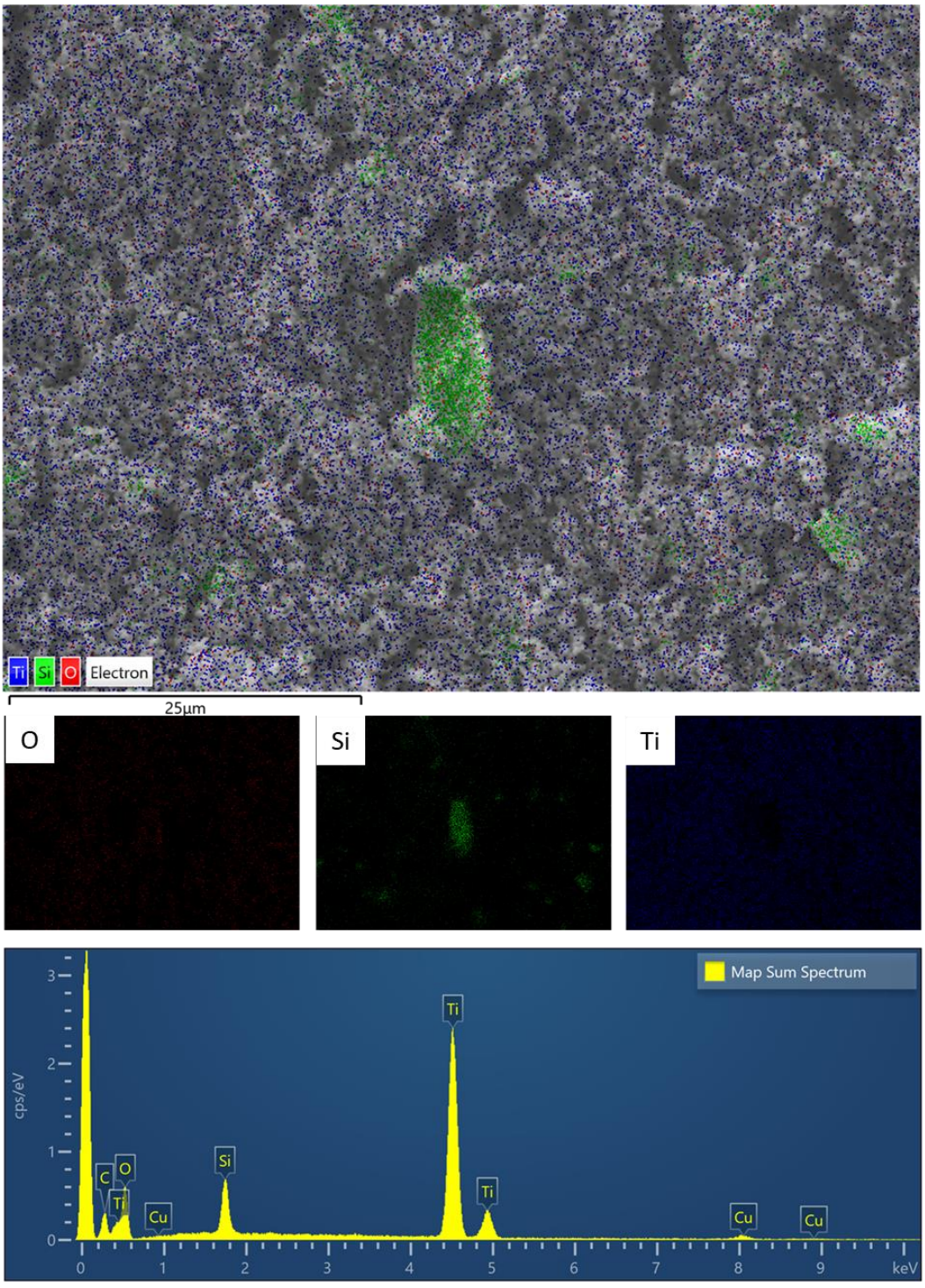

Figure 3.7. EDX analysis of TOS 15 wt% Si support represented as (a) overlay of EDX mapping on SEM image, (b) EDX mapping for individual elements, and (c) EDX elemental analysis.

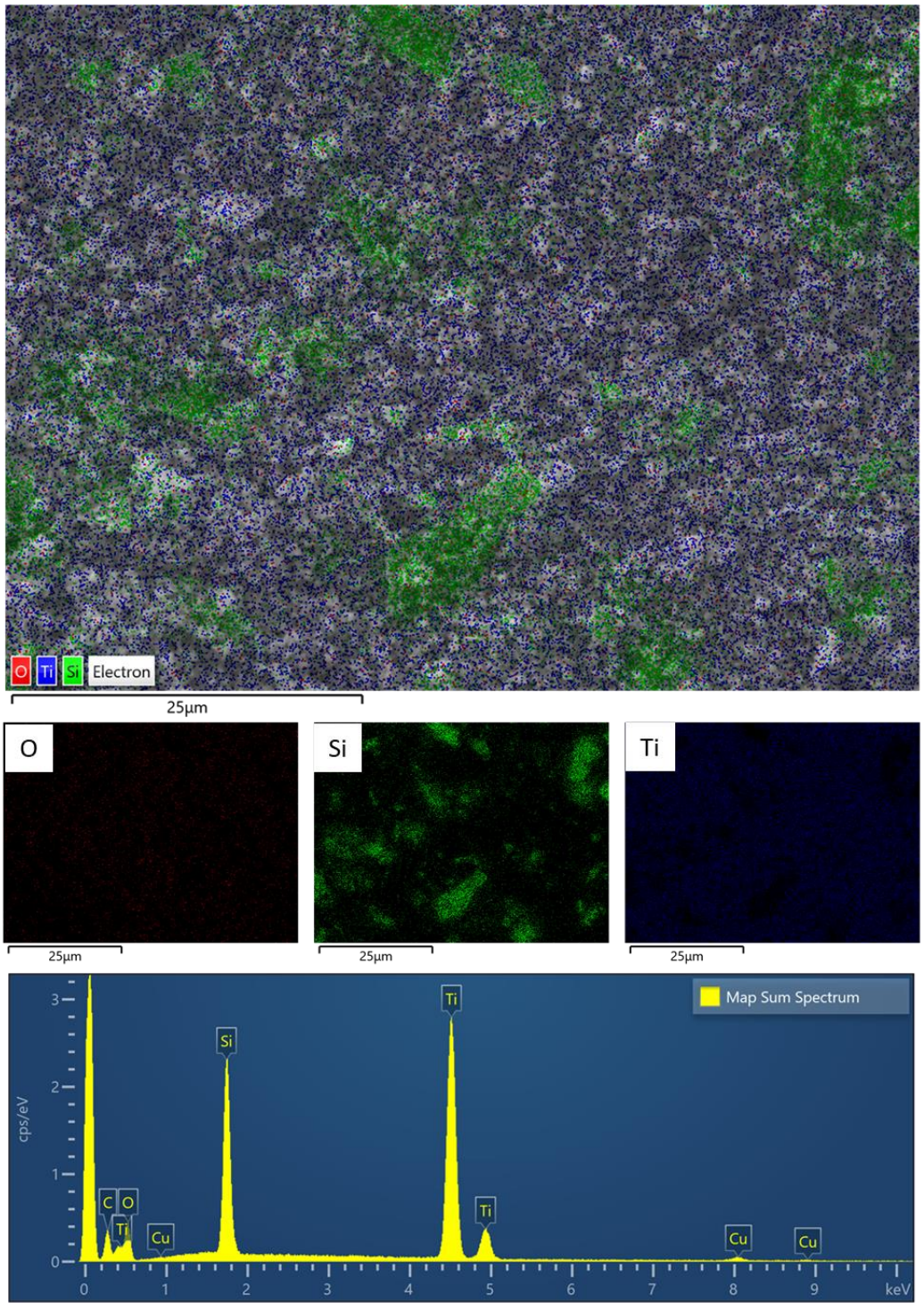

Figure 3.8. EDX analysis of TOS 20 wt% Si support represented as (a) overlay of EDX mapping on SEM image, (b) EDX mapping for individual elements, and (c) EDX elemental analysis.

To further probe the morphology of the TOS 20 wt% Si support, TEM images were

obtained at different magnifications (Figure 3.9). The TEM images confirmed the larger Ti_3O_5 particle sizes ranging from 100-200 nm and the Si agglomerations irregularly distributed across the surface which likely contributed to the low surface area of the support. EDX mapping results are shown in Figure 3.10 which confirms the homogeneity of Ti and O and the irregular dispersion and agglomerations of Si particles.

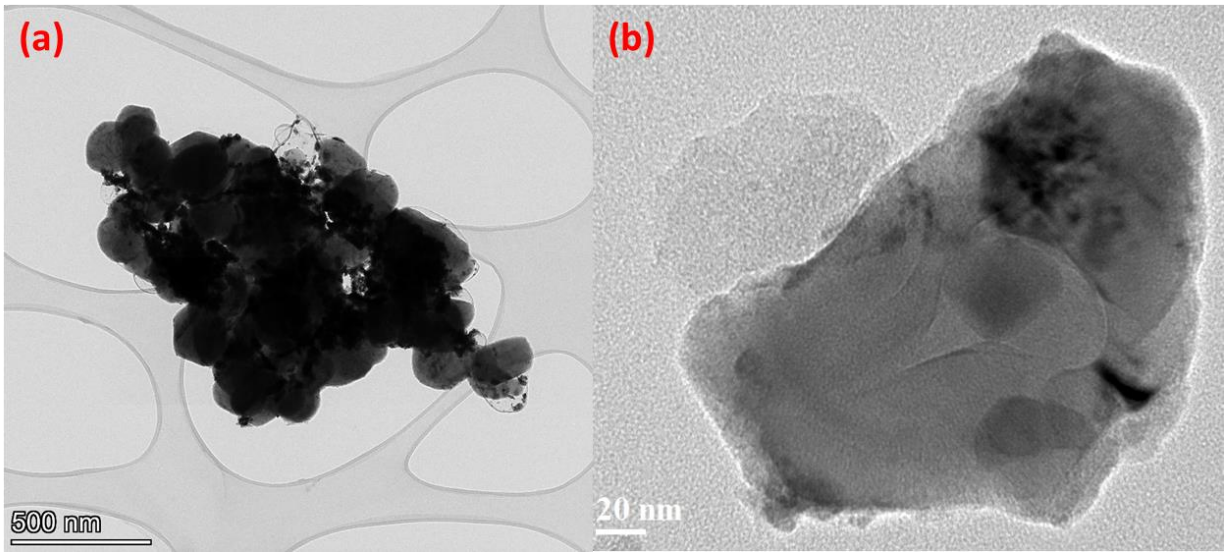

Figure 3.9. TEM images of the TOS 20 wt% Si support at (a) 500 nm and (b) 20 nm.

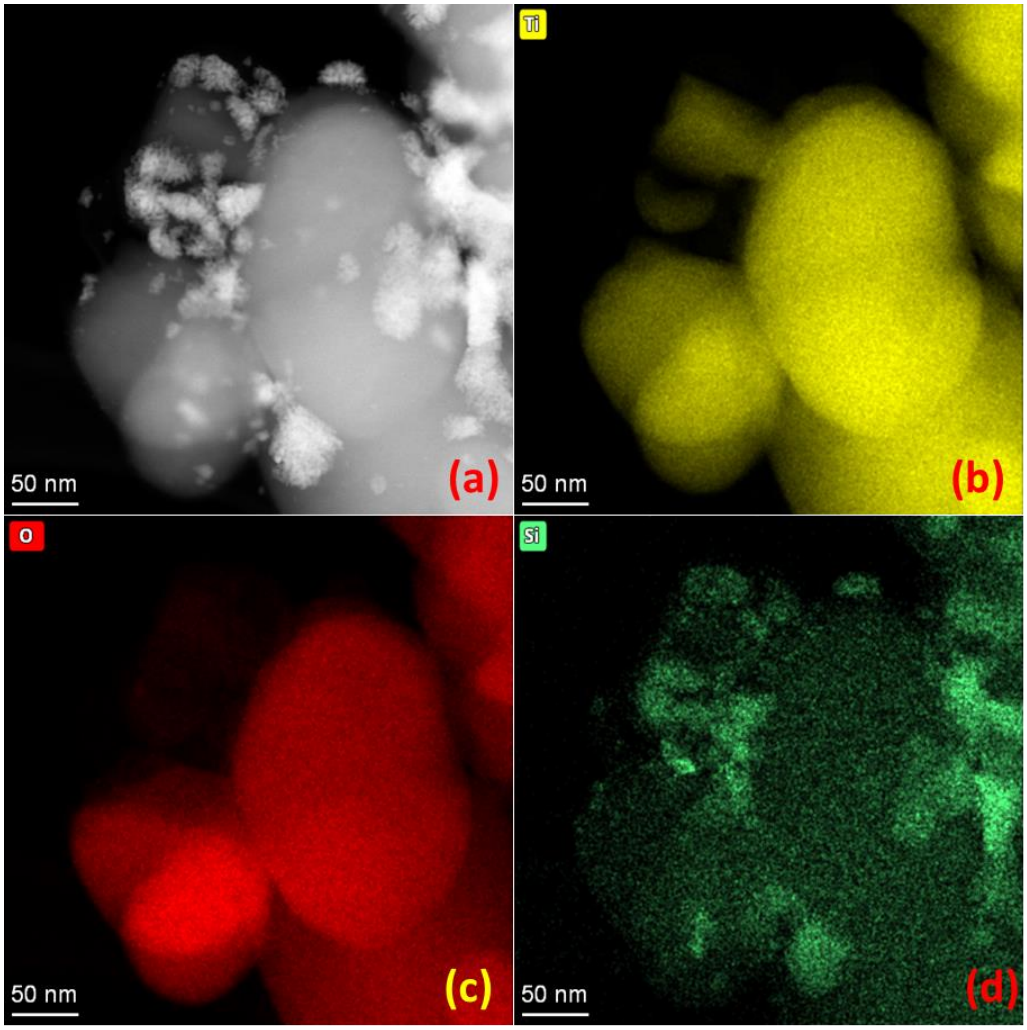

Figure 3.10. EDX analysis of TOS 20 wt% Si support represented as (a) TEM image and EDX mapping corresponding to the distribution of: (b) Ti, (c) O, and (d) Si.

3.1.4 Brunauer-Emmett-Teller Surface Area Analysis

The surface area of the TOS supports was measured by applying the BET nitrogen adsorption technique in which N_2 gas adsorbed onto the surface of the support materials producing N_2 adsorption-desorption isotherms. Figure 3.11 shows the N_2 adsorption-desorption isotherms which relate the volume of nitrogen per gram of material, in mL g^{-1}, to the relative pressure (P/P_0). These isotherms are classified as Type IV isotherms which describe monolayer physisorption of N_2 molecules onto mesoporous materials (pore sizes 2-50 nm).[120]

Table 3.1 summarizes the measured surface areas for TiO_2 and the TOS supports, obtained from the N_2 adsorption isotherms. The surface area for TiO_2 was relatively small yet, upon doping with Silicon, the surface area nearly doubled in size to ca. 30 $m^2 g^{-1}$ with 10 wt% Si, followed by a decrease in the surface area as the amount of Si was increased to 20 wt%. This agrees with the mean particle sizes of the precursor materials, TiO_2 and Si, with a mean particle size of ca. 40 μm. However, literature has shown that although incorporation of silicon material can improve electrochemical activity and electronic conductivity, it can decrease the surface area by blocking accessible pores within the support layer.[76,121]

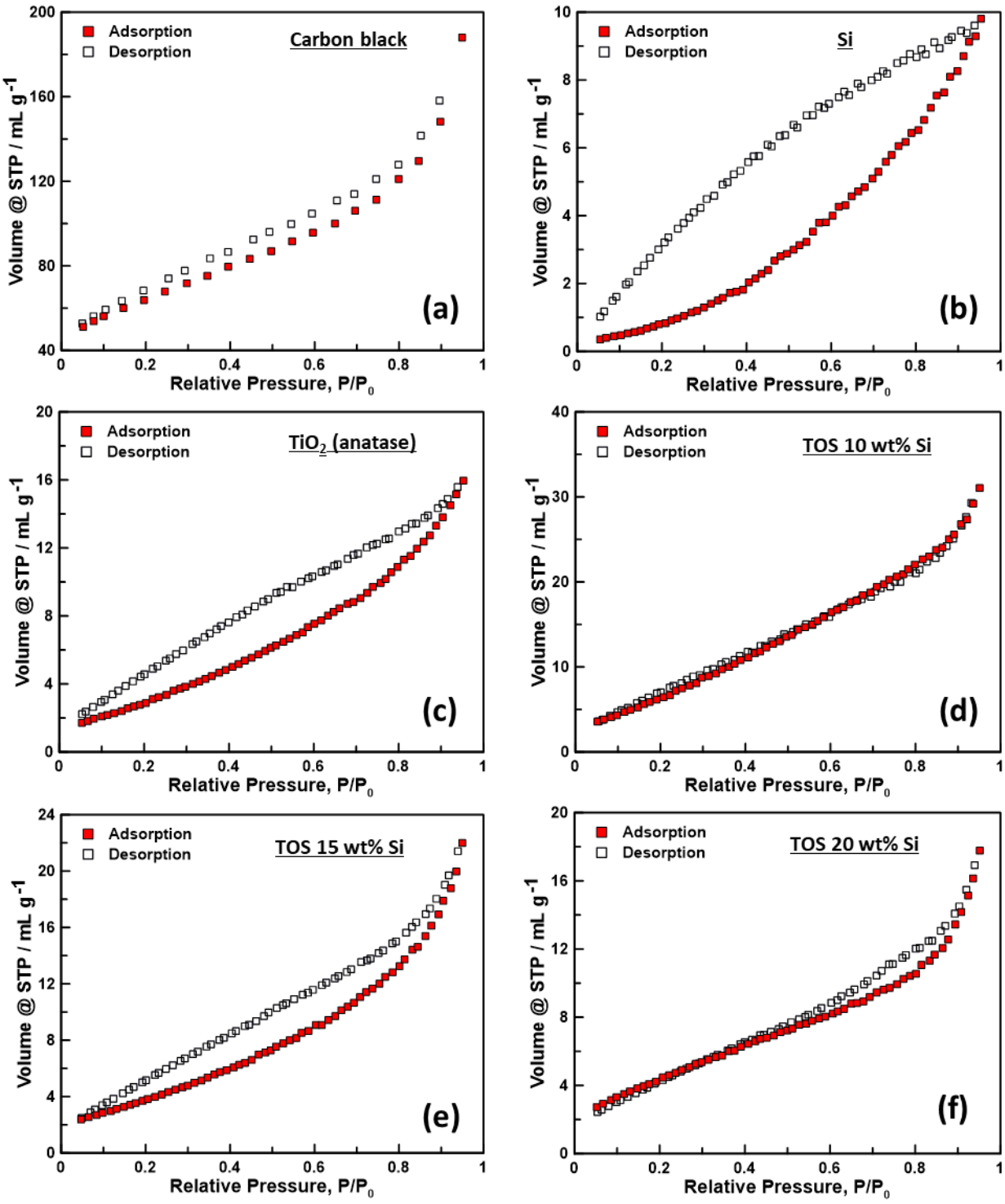

Figure 3.11. Nitrogen adsorption-desorption isotherms obtained during BET surface area analysis for (a) Carbon Black, (b) Si, (c) TiO_2, (d) TOS 10 wt% Si, (e) TOS 15 wt% Si, and (f) TOS 20 wt% Si.

3.2 Electrochemical Characterization

3.2.1 Cyclic Voltammetry and Electrochemical Impedance Spectroscopy

To assess the durability of the TOS supports, a 20,000 cycle ADT was employed. The ADTs were performed at 22 $\pm$ 3°C in N_2-saturated 0.5 M H_2SO_4 solution and scanned at 500 mV s^{-1} over a potential range of 0.05 – 1.25 V_{RHE}. The initial and final CV responses to this ADT are presented in Figure 3.12a - Figure 3.16a, obtained at a scan rate of 200 mV s^{-1} across the usual potential range of 0.05-1.25 V_{RHE}. Overall, the TOS supports displayed remarkable stability, indicating no support corrosion (ie. loss of Ti, Si). Small redox peaks were observed ca. 0.55-0.65 V_{RHE} which are often observed for these pseudocapacitive materials, in this case, attributed to the Ti^{3+}/Ti^{4+} redox couple.[122–124]. However, the TOS 10 wt% Si support did exhibit mild decay in stability during the ADT. At 2-5 wt% Si, the CV shapes deviated from the ideal box-like response, indicating ohmic resistance due to poor electronic conductivity. There was slight change at lower potentials owing to the adsorption and desorption of H^+. Increasing the Si content to 10-20 wt% Si produced CV responses with the desired box-like shape which is indicative of a conductive material.

Further examination of the TOS supports involved thorough EIS analysis which was obtained at an applied DC potential bias of 0.425 V_{RHE} (Figure 3.12b - Figure 3.16b). It has been shown that that this potential was optimal as it lies within the double layer region where faradaic processes are not expected to occur.[86,125] As such, the underlying mass transport properties (ie. electronic and ionic conductivity) can be obtained for the studied support. When regarding the obtained EIS plots, the impedance of each support remained quite stable over the duration of the durability tests which is consistent with the known stability of titanium oxides and SiO_2.[47,126,127] The overall impedance scale was quite large for the 2 and 5 wt% Si supports which

equates to a great deal of ohmic resistance. This was expected due to the low electronic conductivity measured for these supports and confirmed that 2 and 5 wt% Si was not enough to yield the ideal conductive metal oxide support. Inspection of the high frequency region of the Nyquist plot for TOS 2 wt% Si (inset of Figure 3.12b) revealed a Warburg-type response which deviated from the expected 45^{o} slope, confirming the poor conductivity of the support. Projection of this Warburg length on the real axis provided insight toward total resistance in the support layer which is equivalent to the ionic resistance. This is a consequence primarily due to the presence of TiO_2 (rutile) within the suboxide lattice structure. Similar trends were observed with the TOS 5 wt% Si, however, the high frequency region (inset of Figure 3.13b) was very short and increased vertically which would suggest good ionic conductivity however, the overwhelmingly large scale of the real and imaginary impedance axes indicates that the support still possesses high resistivity. As the content of Si is increased to 10-20 wt% Si, the EIS response revealed no change in Warburg lengths which indicates no changes to the ionic resistance however changes in the low frequency region were observed. Changes at low frequency would suggest a change in support surface area which, along with conductivity, can be better represented by plotting series capacitance ($-1/\omega Z''$) against the real axis (Z') to obtain capacitance plots.

To get a better picture of overall support conductivity, capacitance plots were obtained (Figure 3.12c - Figure 3.16c) and offer simultaneous visualization of the conductivity and active surface area of the support. Within these capacitance plots, an initial steep slope is observed which relates the conductivity of the support to its surface area. As such, a larger limiting capacitance indicates larger portions of the surface are accessible. For the TOS 2 and 5 wt% Si

supports, there is an increase in limiting capacitance which is likely a result of SiO_2 agglomeration on the surface of the support as the ADT progressed. Yet, the capacitance was still low, which was a result of the low surface area of the TOS support. Meanwhile, the opposite case is seen for the TOS 10-20 wt% Si supports which display a decrease in limiting capacitance. It is noted that the scale of the limiting capacitance is approximately 1 order of magnitude greater than that of the supports with 2 and 5 wt% Si. The TOS 10 wt% Si support displayed a fair amount of decay (ca. 20%) in limiting capacitance over the course of ADT attributing to a decay in surface area. Compared to the TOS 10 wt% support, the TOS 15 and 20 wt% Si supports displayed small changes in limiting capacitance indicating minimal changes to support surface area. As the Si content was increased to 15 and 20 wt%, the limiting capacitance was observed to decrease with increasing Si content which makes sense – as Si content increases, the accessible surface for the titanium suboxide will decrease. According to this data, the TOS 20 wt% Si support was chosen for platinization due to the promising electronic conductivity and durability it exhibited.

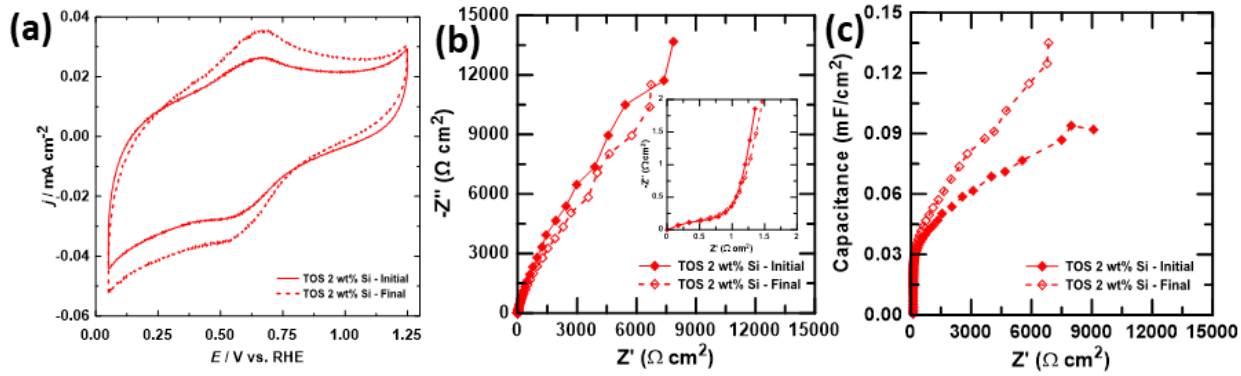

Figure 3.12. (a) Half-cell CV response for the TOS 2 wt% Si support under ADT conditions in N2-saturated 0.5 M H_2SO_4 solution. Complimentary EIS responses are presented as (b) Nyquist and (c) Capacitance plots, obtained at an applied DC bias potential of 0.425 V_{RHE}. Inset of (b) shows the expansion of the Warburg region.

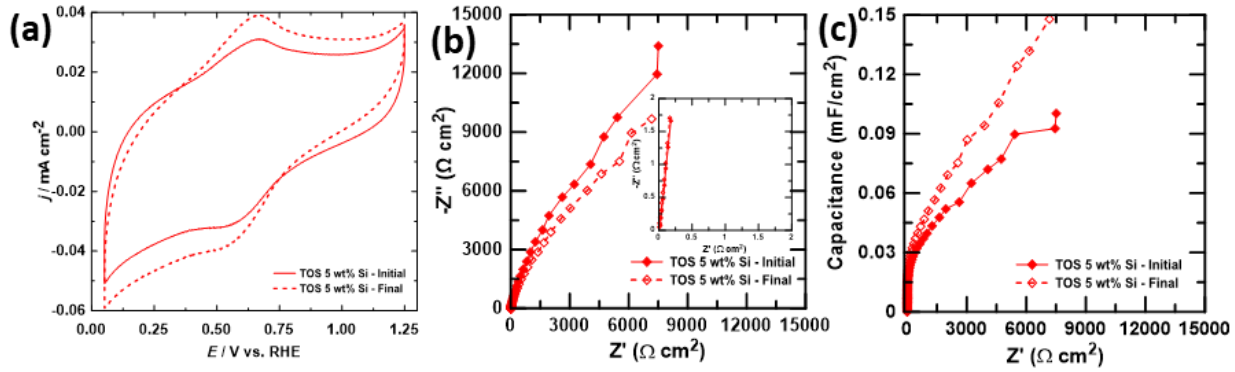

Figure 3.13. (a) Half-cell CV response for the TOS 5 wt% Si support under ADT conditions in N_2-saturated 0.5 M H_2SO_4 solution. Complimentary EIS responses are presented as (b) Nyquist and (c) Capacitance plots, obtained at an applied DC bias potential of 0.425 V_{RHE}. Inset of (b) shows the expansion of the Warburg region.

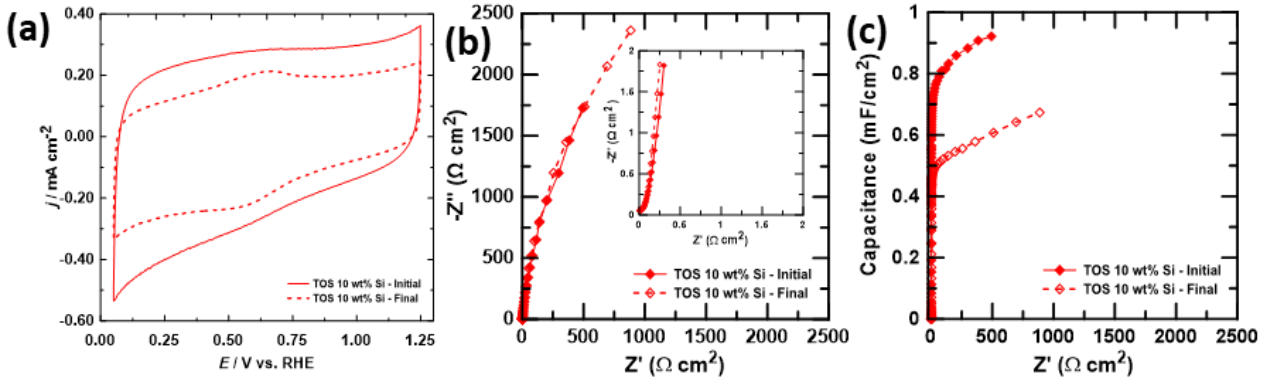

Figure 3.14. (a) Half-cell CV response for the TOS 10 wt% Si support under ADT conditions in N_2-saturated 0.5 M H_2SO_4 solution. Complimentary EIS responses are presented as (b) Nyquist and (c) Capacitance plots, obtained at an applied DC bias potential of 0.425 V_{RHE}. Inset of (b) shows the expansion of the Warburg region.

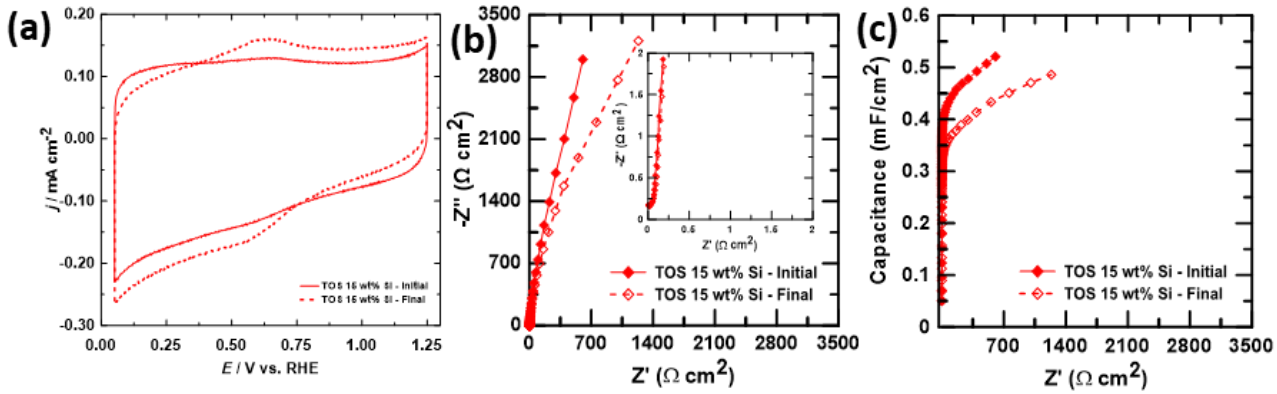

Figure 3.15. (a) Half-cell CV response for the TOS 15 wt% Si support under ADT conditions in N2-saturated 0.5 M H_2SO_4 solution. Complimentary EIS responses are presented as (b) Nyquist and (c) Capacitance plots, obtained at an applied DC bias potential of 0.425 V_{RHE}. Inset of (b) shows the expansion of the Warburg region.

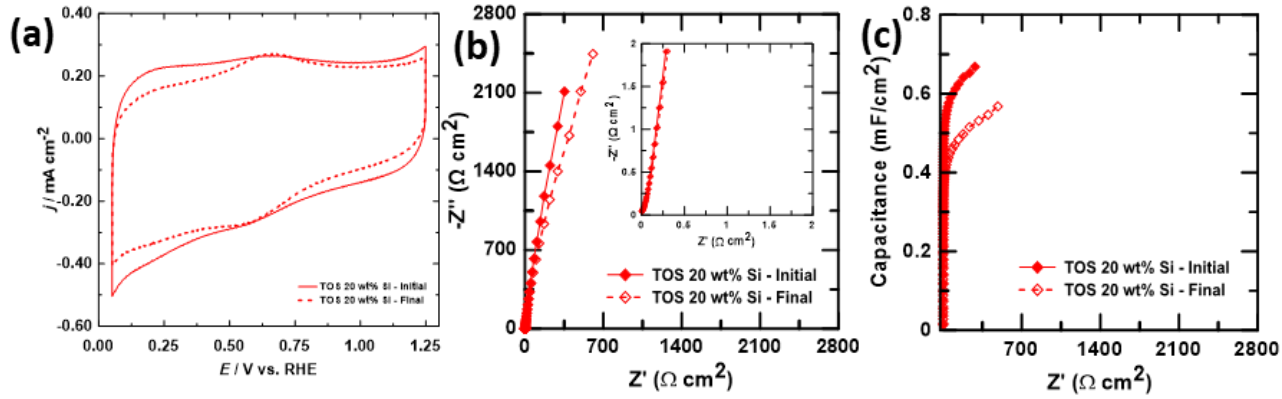

Figure 3.16. (a) Half-cell CV response for the TOS 20 wt% Si support under ADT conditions in N_2-saturated 0.5 M H_2SO_4 solution. Complimentary EIS responses are presented as (b) Nyquist and (c) Capacitance plots, obtained at an applied DC bias potential of 0.425 V_{RHE}. Inset of (b) shows the expansion of the Warburg region.

3.3 Materials Characterization for the Platinized TOS 20 wt% Si Support (Pt/TOS)

3.3.1 X-Ray Diffraction for Pt/TOS catalyst

To investigate the crystallographic structure of the platinized TOS 20 wt% Si support, Pt/TOS 20 wt% Si, XRD patterns were obtained (Figure 3.17) and compared to a commercial Pt/C catalyst. The key Pt reflections (ICDD Card 01-087-0640) were observed at 2θ = 39.98° {111},

46.51° {200}, 67.69° {220}, 81.60° {311}, and 86.27° {222}, corresponding to metallic Pt with a face-centered cubic structure. The peak at 2θ = 39.98° was broad and intense which suggested the Pt NPs favored orientation in the Pt {111} plane which is known to possess stability and high activity toward the ORR.[128] The average Pt crystallite size for the Pt/TOS and Pt/C catalysts was determined from the Debye-Scherrer formula using the peak position and full-width half-maximum of the Pt grains in {311} and {222} orientation. Table 3.2 shows the average Pt grain size was determined to be 2 and 7 nm for the Pt/C and Pt/TOS catalysts, respectively.

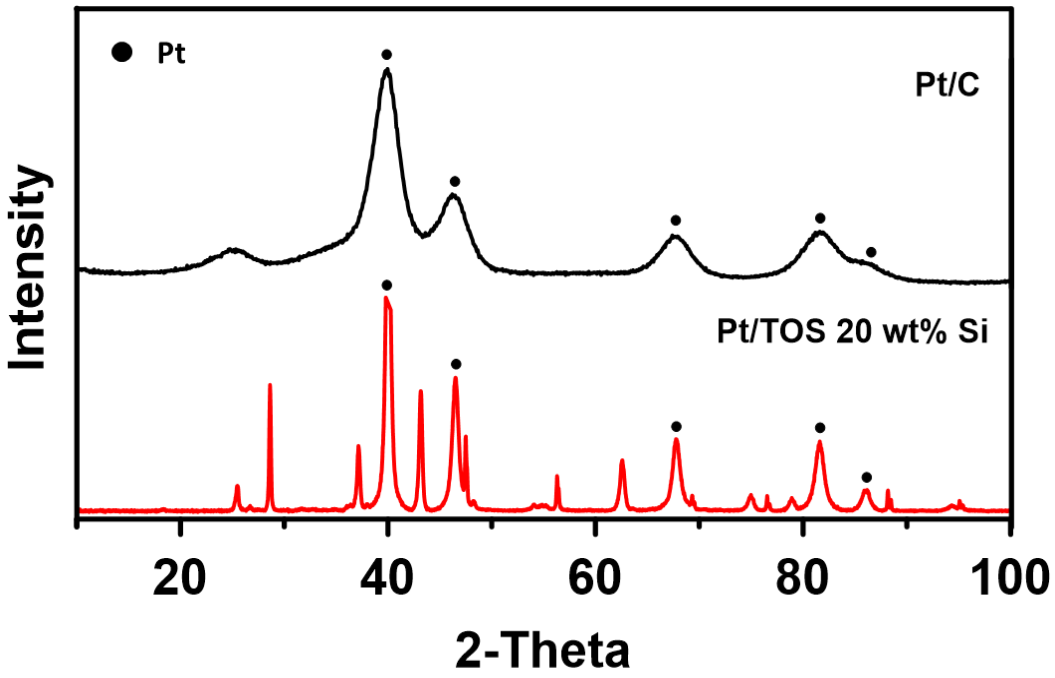

Figure 3.17. XRD patterns obtained for the Pt/TOS 20 wt% Si catalyst compared against a commercial Pt/C catalyst. The black dots represent the Pt reflections. An XRD pattern for the TOS 20 wt% Si support is shown for reference.

Table 3.2. Summary of Pt grain sizes and ECSA.

Catalyst material	Pt Grain Size (nm)	BOL ECSA ($m^2\ g^{-1}$)
Pt/C	2	80.7
Pt/TOS	7	13.5

3.3.2 Transmission Electron Microscopy

To confirm the grain size and dispersion of platinum NPs over the TOS support, TEM images were obtained for the Pt/TOS electrocatalyst (Figure 3.18). The Pt grain size on the TOS support agreed with XRD analysis which determined the average grain size to be between 4-8 nm. The dispersion of Pt NPs on the TOS support surface was inadequate which resulted in the low ECSA. Moreover, the Pt NPs existed in irregular agglomerations on the surface of the support. Through EDX mapping (Figure 3.19), it was evident that the Pt agglomerations formed where Si agglomerations existed on the TOS support surface. This would suggest that surface -OH groups attached to the Si particles served as nucleation sites for the Pt NPs in addition to anchoring the NPs to the surface.[129,130]

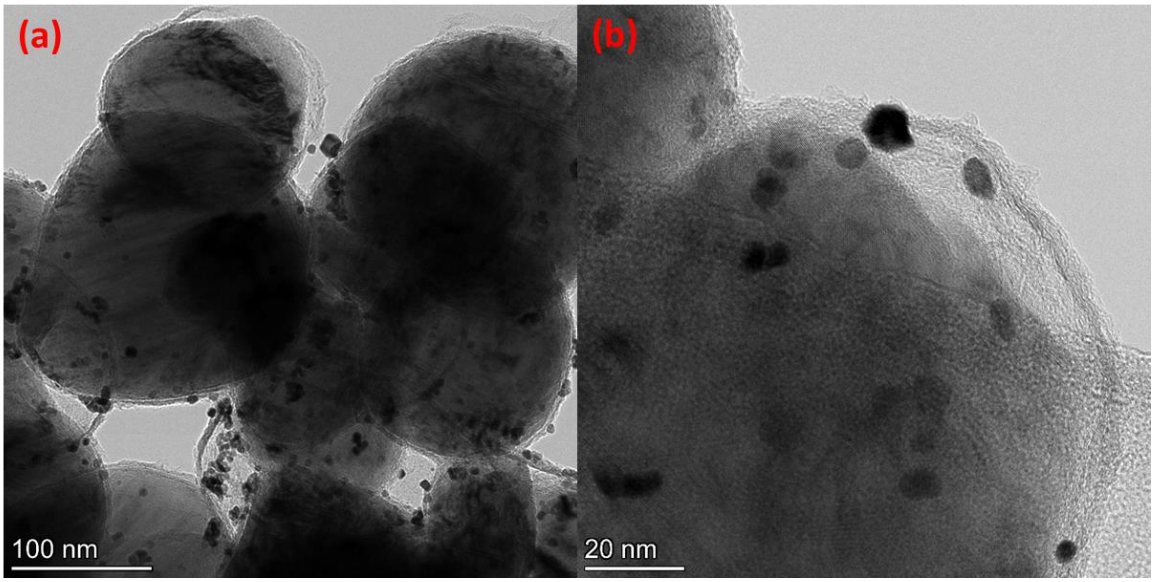

Figure 3.18. TEM images corresponding to the Pt/TOS electrocatalyst.

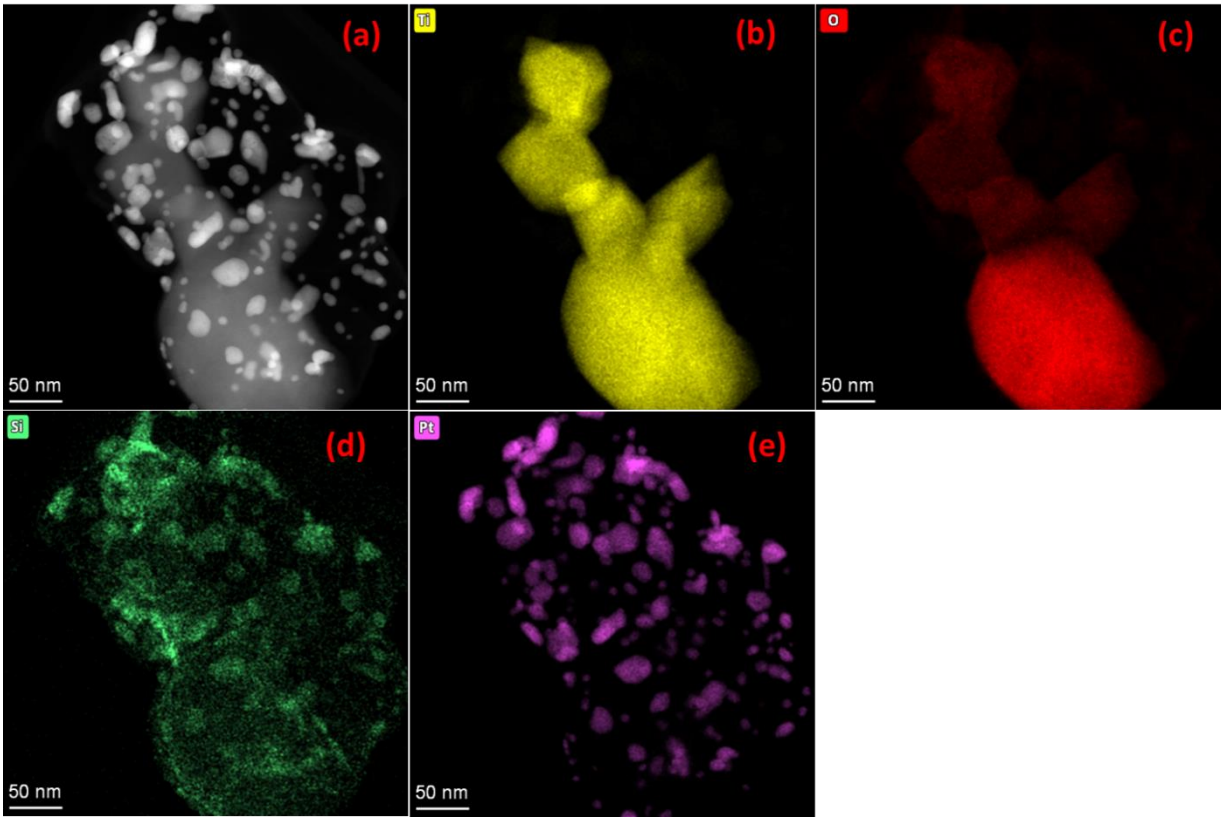

Figure 3.19. EDX analysis of the Pt/TOS electrocatalyst represented as (a) TEM image and EDX mapping corresponding to the distribution of: (b) Ti, (c) O, (d) Si, and (e) Pt.

3.4 Electrochemical Characterization of Pt/TOS

3.4.1 Cyclic Voltammetry and Electrochemical Impedance Spectroscopy

To study the durability, stability, and the interactions between the TOS support and Pt catalyst NPs, a 20,000 cycle ADT was performed. Figure 3.20a shows the initial CV response to the ADT for the Pt/TOS and Pt/C catalysts by scanning over a potential range of 0.05 – 1.25 V_{RHE} in 0.5 M H_2SO_4 solution. The Pt/TOS and Pt/C catalysts produced peaks in the 0.05 – 0.30 V_{RHE} region which are characteristic of Pt-H adsorption and desorption. A stable capacitive current was observed between ca. 0.35 – 0.80 V_{RHE} indicating the absence of redox processes. Pt-O formation can be observed on the forward scan from 0.85 – 1.25 V_{RHE} and the reduction process is observed on the reverse scan from 1.25 – 0.60 V_{RHE}. The variation in ECSA of Pt over

the course of the ADT is shown in Figure 3.20c, which was obtained from the integration of the Pt-H desorption peak, in nitrogen. The ECSA at the beginning of life (BOL) of the ADT was revealed to be 13.54 $m^2 g^{-1}$ for Pt/TOS while the BOL ECSA for Pt/C was found to be 80.70 $m^2 g^{-1}$. The ECSA of the Pt/TOS was smaller likely due to the low surface area of the support in addition to the thin SiO_2 layer in the TOS support which has been shown by Eastcott and Easton (2009) to inhibit and cover Pt active sites in the catalyst layer.[121] Despite possessing a low ECSA, the Pt/TOS catalyst did possess greater stability during the ADT, during which it only experienced a loss in ECSA of ca. 25% after 20,000 cycles compared to a significant loss of ca. 90% for the Pt/C catalyst (Figure 3.20c,d). While the low ECSA is less than desirable for Pt/TOS, it displays remarkable durability exhibited a decline in ECSA of ca. 10% for the first 5,000 cycles of the ADT compared to ca. 70% for the Pt/C catalyst. This exemplified the ability of titanium suboxide supports to strongly anchor the Pt NPs through SMSI which prevent Pt dissolution or agglomeration compared to the commercial Pt/C catalyst.

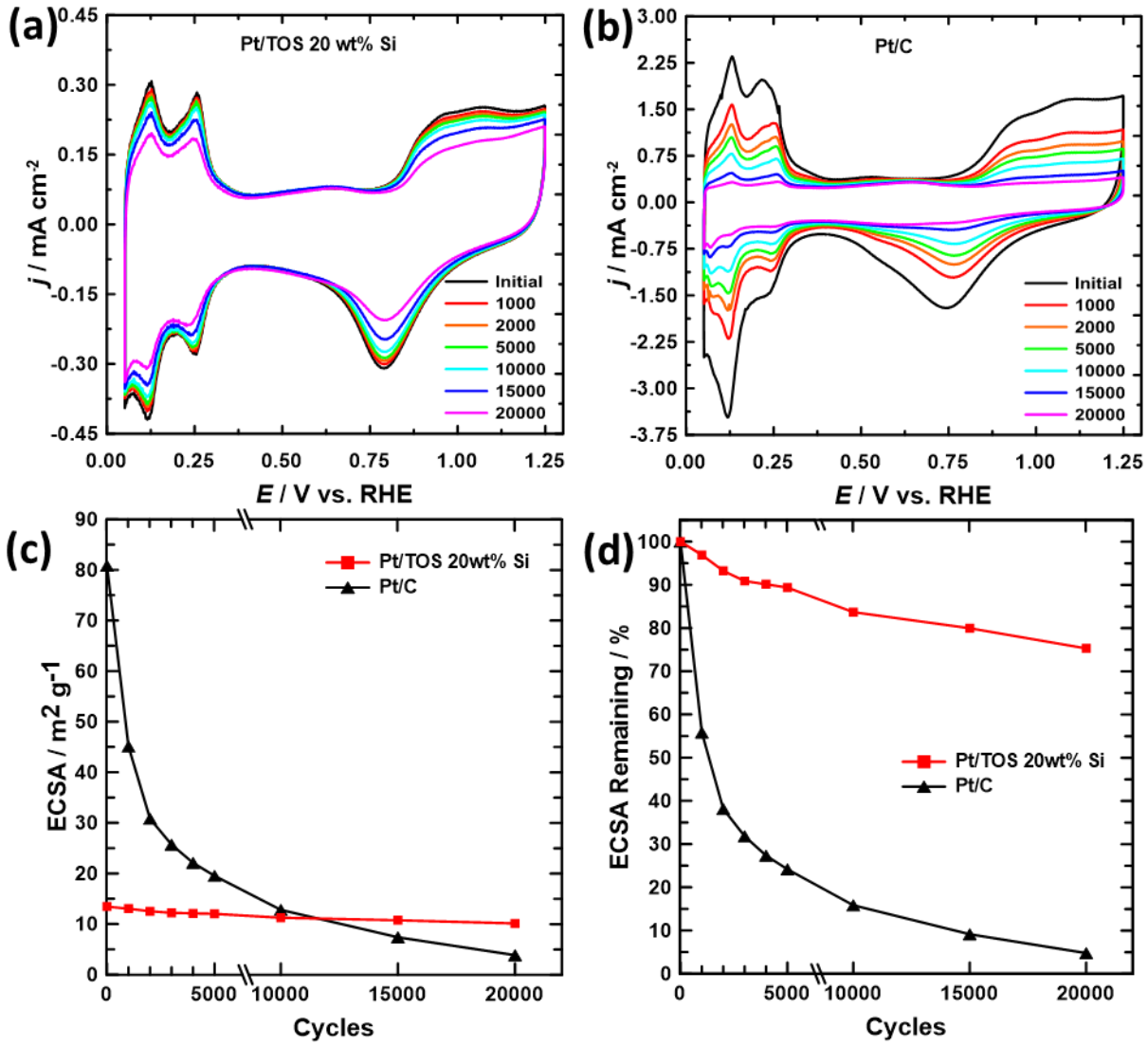

Figure 3.20. Comparisons of the CV responses obtained for the (a) Pt/TOS and (b) Pt/C catalysts in N2-purged 0.5 M H_2SO_4 solution over a potential range of 0.05-1.25 V_{RHE} for 20,000 potential cycle ADT. (c) The variation in ECSA and (d) the ECSA remaining (%) are shown for the Pt/TOS and Pt/C catalysts over the course of the ADT.

To further investigate the ECSA and the behavior between the TOS support and Pt NPs, EIS experiments were performed and presented as Nyquist and capacitance plots (Figure 3.21). These plots monitor the EIS response for the Pt/TOS and Pt/C catalyst layers throughout the 20,000 cycle ADT, obtained at an applied DC bias potential of 0.425 V_{RHE}. The Nyquist and

capacitance plots for Pt/TOS, combined with the expansion of their high-frequency regions (insets of Figure 3.21a,b), remained virtually constant which indicates no significant changes to electronic conductivity and the absence of support corrosion with increasing cycle number. By similar convention, there were no significant changes in the Nyquist plot or the high-frequency region which suggested the electronic conductivity within the Pt/C catalyst remained constant (Figure 3.21c,d). Despite this however, the limiting capacitance for Pt/C deteriorated by ca. 33% which is consistent with a decrease in Pt surface area via Pt size growth.[91,103,131] Through these plots, a clear understanding of the relationship between ECSA and EIS was conveyed which showed that higher total catalyst layer resistivity correlated with a lower ECSA.

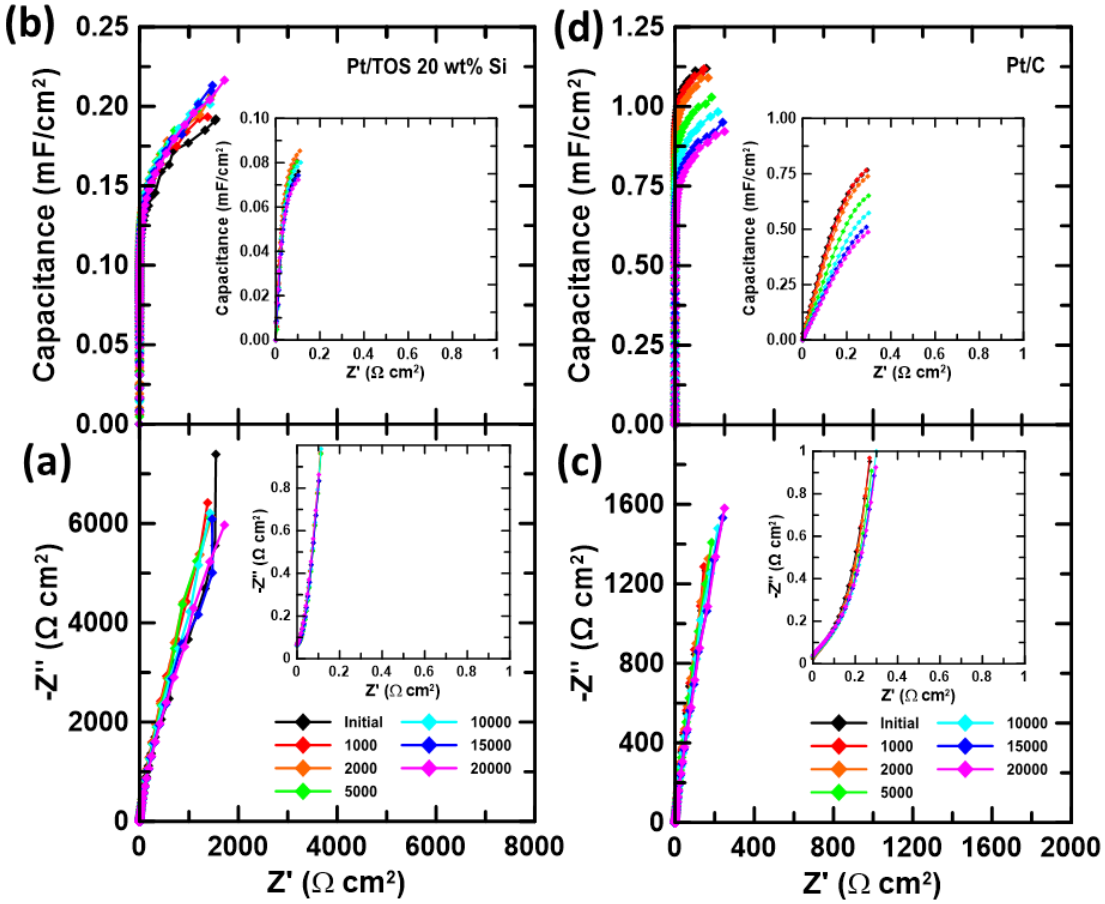

Figure 3.21. EIS response curves for the Pt/TOS and Pt/C catalysts obtained at an applied DC bias potential of 0.425 V_{RHE} before and after the ADT. The Pt/TOS data is presented as (a) Nyquist plot and (b) capacitance plot. The Pt/C data is presented as (c) Nyquist plot and (d) capacitance plot. The insets of each figure represent the corresponding expansion of the Warburg region.

3.4.2 Electroactivity Toward Oxygen Reduction Reaction

The electroactivity of the Pt/TOS catalyst toward the oxygen reduction reaction (ORR) was examined before (BADT) and after (AADT) a 5,000 potential cycle ADT, using the RDE setup, in oxygen-saturated 0.5 M H_2SO_4 solution and obtained at 1200 rpm. The ORR experimental data are summarized in Table 3.3. Figure 3.22a shows the LSV response for the Pt/TOS and Pt/C catalysts before and after an ADT protocol of 5,000 potential cycles measured over a potential range of 0.05 – 1.25 V_{RHE}. The Pt/TOS catalyst exhibited mild ORR activity showing onset potential

which, as a general guideline, was taken to be the potential at 5% of the limiting current, or of 0.88 V_{RHE}. To assess the change in activity of the Pt/TOS catalyst toward ORR before and after the ADT, the half-wave potential ($E_{1/2}$) was monitored. The $E_{1/2}$ was determined to be 0.77 V_{RHE} and the current produced at 0.9 V_{RHE} was 0.15 mA cm^{-2} (Table 3.3). After the durability test, $E_{1/2}$ showed almost no changes which demonstrates the durability of Pt/TOS toward the ORR, however the poor activity is a result of the low utilization of Pt indicated by the ECSA. The Pt/C catalyst possessed a high onset potential of 0.92 V_{RHE} and produced 0.59 mA cm^{-2} at 0.9 V_{RHE} prior to the AST. After the AST, $E_{1/2}$ decreased by 90 mV as a result of Pt corrosion. Generally, catalysts with high surface area and the number of available active catalyst species correlates with ORR performance.[47]

The initial CV response of each catalyst was obtained before the 5,000 cycle AST which shows good reversibility and the 2 characteristic peaks of in the Pt-H formation and reduction regions indicative of an even dispersion of Pt NPs over the support surface (Figure 3.22b). The ECSA and loss in ECSA were monitored over the course of the AST between RDE measurements (Figure 3.22c,d). The ECSA for Pt/TOS demonstrated almost no variation with increasing cycle number – only a 2.8% loss in ECSA was observed. Meanwhile, the rate of decay in ECSA for Pt/C was extensive and corresponded to ca. 31.6% ECSA remaining indicating an underlying degradation mechanism is involved (ie. Pt dissolution/agglomeration).[20,30,91,103]

Table 3.3. ORR activity of Pt/TOS and commercial Pt/C catalysts.

Catalyst	Pt loading (mg cm^{-2})	I @ 0.9 (mA cm^{-2})	$E_{1/2,intial}$ (V_{RHE})	$E_{1/2,final}$ (V_{RHE})	BOL ECSA (m^2 g^{-1})	ECSA Remaining (%)	Electrolyte, Cycles, Scan rate (mV s^{-1})
Pt/TOS	0.020	0.15	0.77	0.76	11.8	97.2	0.5 M H_2SO_4, 5000, 10
Pt/C	0.025	0.60	0.83	0.74	81.3	31.6	0.5 M H_2SO_4, 5000, 10

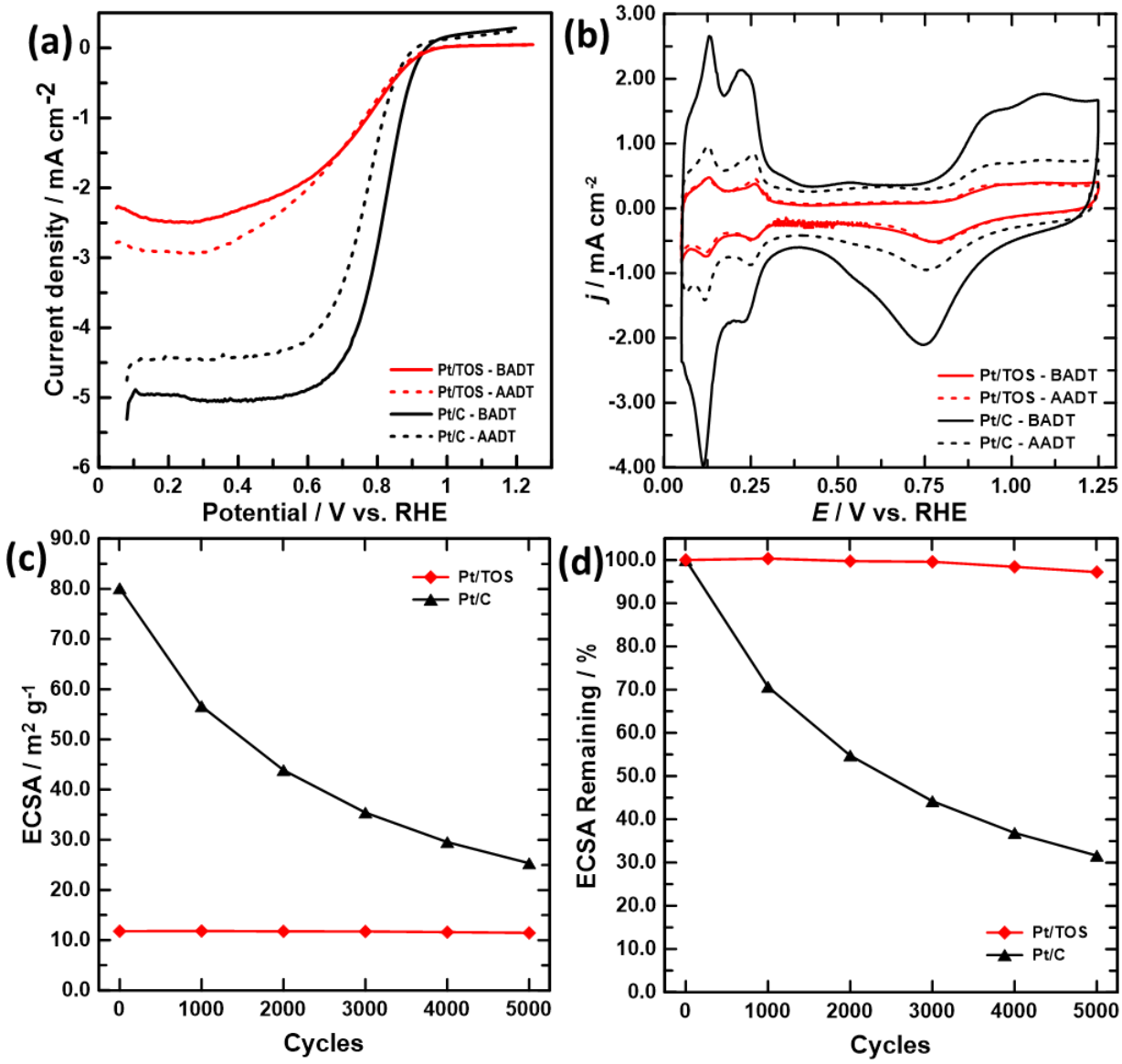

Figure 3.22. (a) LSVs representing the ORR activity for the Pt/TOS and commercial Pt/C catalysts recorded at 10 mV s^{-1} in O_2-saturated 0.5 M H_2SO_4 (1200 rpm). The variation in (b) CV response and (c) ECSA, and (d) the ECSA remaining (%) for the catalysts during the 5,000 potential cycle ADT, were recorded in N_2-saturated H_2SO_4.

3.4.3 Accelerated Stress Tests: Load Cycling

Load cycling is a protocol designated by the US Department of Energy (DoE) to assess the stability of the Pt/TOS catalyst against Pt dissolution and agglomeration during normal fuel cell operation.[132–135] This test involved load cycling the catalysts for 10,000 cycles using a rectangular-wave form, from 0.6-1.0 V_{RHE}, with a retention time of 3 s. 0.6 V_{RHE} is close to the maximum power and approaches full load conditions, whereas 1.0 V_{RHE} is close to the open circuit potential and approaches no-load conditions. The initial CV response for the Pt/TOS and Pt/C catalysts are shown in Figure 3.23a, both showing good reversibility and the characteristic peaks for hydrogen adsorption/desorption, and Pt-O formation and reduction. The change in ECSA (Figure 3.23b) was monitored across the 10,000 cycle AST, with the Pt/TOS and Pt/C catalysts showing a decay of 11.4% and 22.3% in ECSA, respectively. The minimal loss in ECSA for Pt/TOS is attributed to the strong interactions between the TOS support and Pt NPs preventing agglomeration and dissolution. Finally, catalyst conductivity and support stability were probed with EIS measurements presented as total resistance within the catalyst layer, R_{Σ}, and the limiting capacitance at low frequencies, C_{LIM}, in Figure 3.23c,d. The Pt/TOS catalyst showed minimal variation in R_{Σ} and C_{LIM} indicating no support corrosion or catalyst degradation. While on the other hand, the Pt/C catalyst exhibited small decrease to C_{LIM} and a 25% loss in R_{Σ}. The loss in ECSA and capacitance were consistent with an underlying Pt dissolution/agglomeration mechanism.[91]

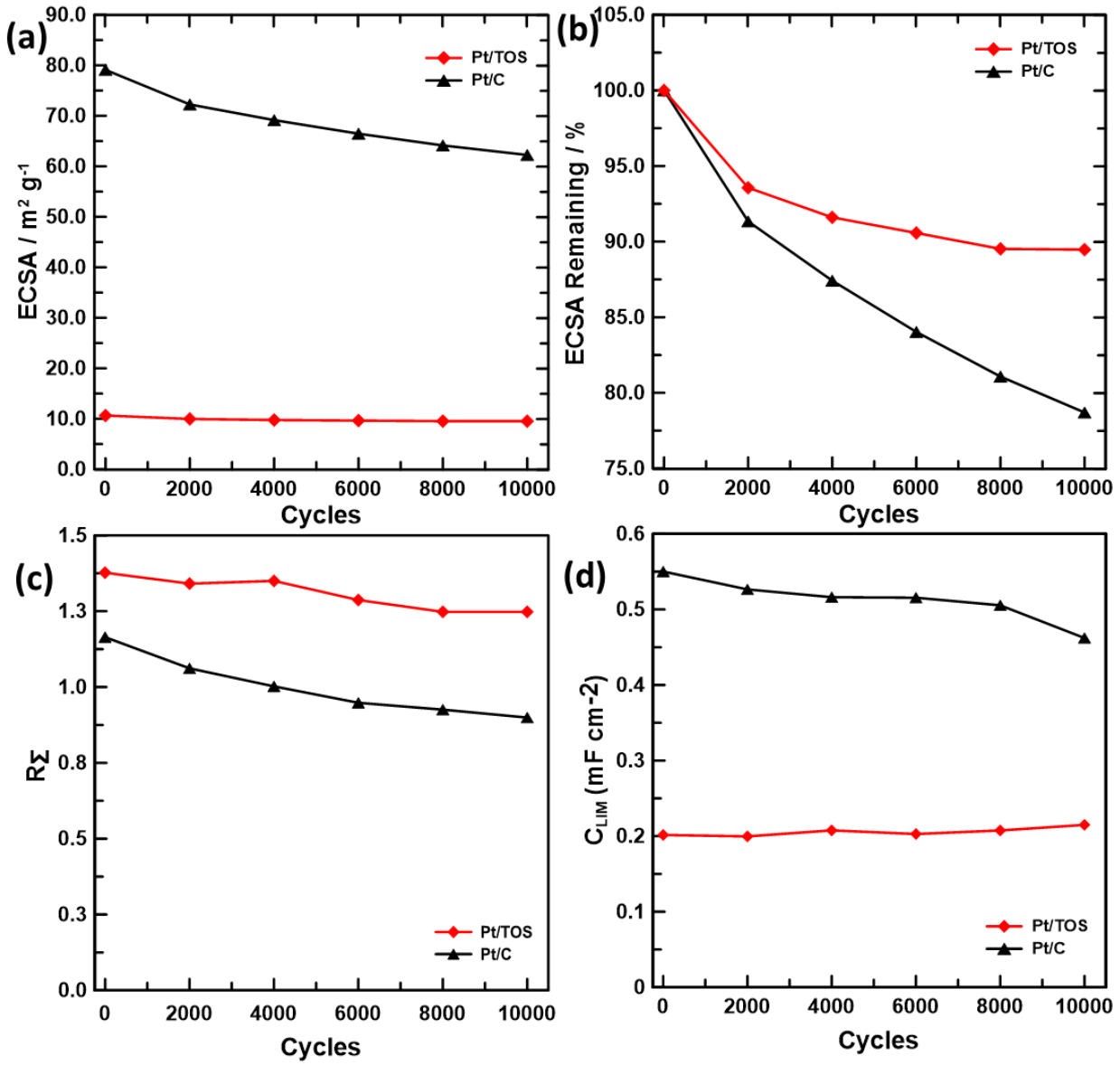

Figure 3.23. (a) LSVs representing the ORR activity for the Pt/TOS and commercial Pt/C catalysts recorded at 10 mV s^{-1} in O_2-saturated 0.5 M H_2SO_4 (1200 rpm). The variation in (b) CV response and (c) ECSA, and (d) the ECSA remaining (%) for the catalysts during the 5,000 potential cycle ADT, were recorded in N_2-saturated H_2SO_4.

3.4.4 Accelerated Stress Tests: Startup/Shutdown

Further assessment of catalyst stability involved aggressive startup/shutdown conditions which probed support/catalyst corrosion and Pt NP degradation via dissolution, growth, or agglomeration.[132,136] Similar to the load cycling protocol, a potential-square waveform was cycled

10,000 times between 1.0-1.5 V_{RHE} with a retention time of 3 s in 0.1 M H_2SO_4 solution (Figure 3.24). The Pt/TOS catalyst indicated no signs of substantial degradation within the double layer region or the support. The ECSA was observed to decrease ca. 28% while the EIS response was relatively constant for R_Σ and C_{LIM}. However, the Pt/C catalyst experienced substantial loss in ECSA of ca. 90% while R_Σ was observed to increase rapidly over the course of the AST. The C_{LIM} response initially increased after 2,000 cycles and then followed a steady decay profile until the end of the AST. The initial increase in C_{LIM} was attributed to the formation of redox species forming on the surface of the carbon support. These results are primarily consistent with carbon support corrosion and increased degradation of the Pt NPs via dissolution.[137,138]

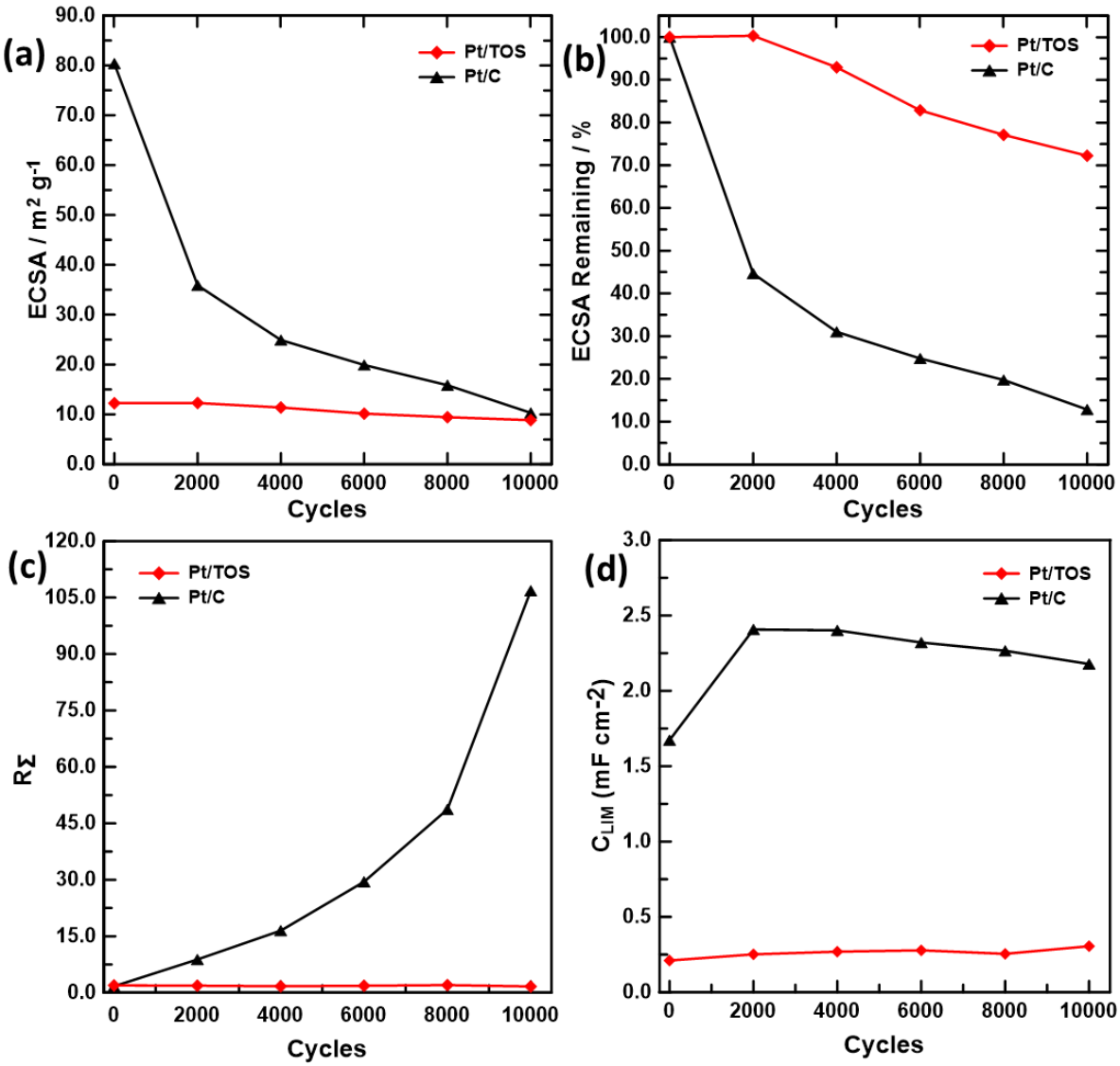

Figure 3.24. AST Startup/shutdown protocol for the Pt/TOS 20 wt% Si catalyst showing (a) variation in ECSA and (b) ECSA remaining over the course of the AST, (c) R_{Σ} and (d) C_{LIM} both obtained at a DC bias potential of 0.425 V_{RHE}.

3.5 Summary

This chapter provided a thorough investigation on the impact of doping TiO_2 with varying Si concentrations. Through heat treatment under a reducing environment, a Ti_3O_5 suboxide support doped by Si was successfully synthesized with a narrow band gap, high electronic conductivity, remarkable durability, and exceptional stability toward the ORR. Through XRD

analysis, it was determined that 2-5 wt% Si was not enough to drive the complete reduction of Ti^{4+} to Ti^{3+} as the supports were dominated by the semiconductive TiO_2 (rutile) phase. As the concentration of Si was increased to 10-20 wt%, the desired Ti^{3+} suboxide phases became more prevalent and the semiconductive phases subsided suggesting higher concentrations of Si dopant would lead to more conductive support materials. The electronic conductivity and band gap of these supports were confirmed with the 10-20 wt% Si supports possessing narrow band gaps and conductor-like conductivities due to the presence of the conductive titanium suboxide phases, Ti_3O_5 and Ti_4O_7, which were absent in the 2-5 wt% Si supports. Overall, the TOS support was optimized for 20 wt% Si and achieved slightly higher conductivity compared to the previously synthesized TOMS support and well exceeded that of the TOM support. This was also reflected in the band gap energies with the TOM support possessing a moderately wide gap value of 2.6 eV, TOMS with a band gap of 0.31 eV, and the most conductive TOS support possessing a near-TOMS band gap value of 0.50 eV.

Rigorous electrochemical tests for the TOS supports confirmed the poor conductivity for the TOS 2-5 wt% Si supports whereas the TOS 10-20 wt% Si supports displayed remarkable durability and stability in response to vigorous durability testing which was on par with the TOM and TOMS supports. Further EIS analysis revealed no signs of support corrosion/leaching of Si or Ti into the electrolyte, or changes to electronic conductivity indicating the TOS 20 wt% Si was a viable candidate as a conductive support for the Pt catalyst.

Once optimized for 20 wt% Si, the TOS support was platinized and continued to demonstrate remarkable durability and stability compared to the commercial Pt/C catalyst which can be attributed to the strong electronic interactions (ie. SMSI) between the TOS support and

Pt. Unfortunately, the Pt/TOS catalyst possessed a small ECSA (11.8 $m^2 g^{-1}$) due to a low support surface area which resulted in low Pt utilization. Through TEM imaging, it was determined that the low ECSA was a result of the unevenly distributed Si agglomerations which served to anchor the Pt NPs to the support surface via surface -OH groups. The ECSA was nearly half of that determined for the Pt/TOM catalyst (22.3 $m^2 g^{-1}$) and almost 10 times less that the ECSA for Pt/TOMS (89.6 $m^2 g^{-1}$).[119,139] The low ECSA resulted in poor activity toward the ORR, however, the Pt/TOS catalyst performed considerably well when subjected to aggressive *ex-situ* load cycling and SU/SD AST protocols. No significant changes were observed within the Pt/TOS catalyst meanwhile the Pt/C exhibited typical decay profiles for carbon support corrosion and Pt NP size growth via dissolution/agglomeration.

While the performance of the TOS support was impressive, the performance of the Pt/TOS catalyst and its low ECSA were not ideal for fuel cell application. This suggests co-doping TiO_2 with Si and Mo is more effective in enhancing the ECSA through increased support surface area. Thus, the next section serves to exploit the exceptional durability of the Si-doped TOS support while optimizing the surface area of the support to enhance the ECSA of Pt.

Chapter 4: Optimization of Surface Area for TOS Support

Chapter 3 determined the optimal Si content within the TOS support to be 20 wt% Si, however, this support was reported with a very small surface area of ca. 18 m^2 g^{-1} which was observed to produce a low ECSA and resulted in poor activity toward the ORR. This section investigates the optimization of the TOS 20 wt% Si support surface area through incorporation of precursor materials with smaller particle size. The conventional TOS support involved relatively large TiO_2 and Si particles on the order of ca. 40 μm in particle size. The first method discussed involves ball milling Si powder to refine the Si particle size and enhance particle distribution. The silicon powder was ball milled using a Planetary Ball Mill, with steel balls, over various time intervals to optimize the ball milling time with respect to Si surface area. Ball milling was performed up to 72 h and the particle size was assessed via SEM. A second method is also explored that involves a novel ball milled Si NPs encapsulated by *in-situ* grown TiO_2, creating a support with a larger surface area. This higher surface area is expected to result in a more uniform dispersion of catalyst particles on the support surface and improve ECSA and ORR activity.

4.1 Investigating Ball Milled Silicon as precursor for TOS Support

4.1.1 Materials Characterization

SEM images were obtained of the Si powder before ball milling, and after periods of 4 h, 24 h, and 72 h of ball milling (Figure 4.1). Before ball milling, the Si particles were large and irregularly shaped ranging in size from 0.5 – 10 μm. As the duration of ball milling was increased, the Si particles were observed to decrease by at least one order of magnitude and became more uniform in shape. In Figure 4.1c,d the red boxes highlight areas where particles smaller than 0.1 μm exist.

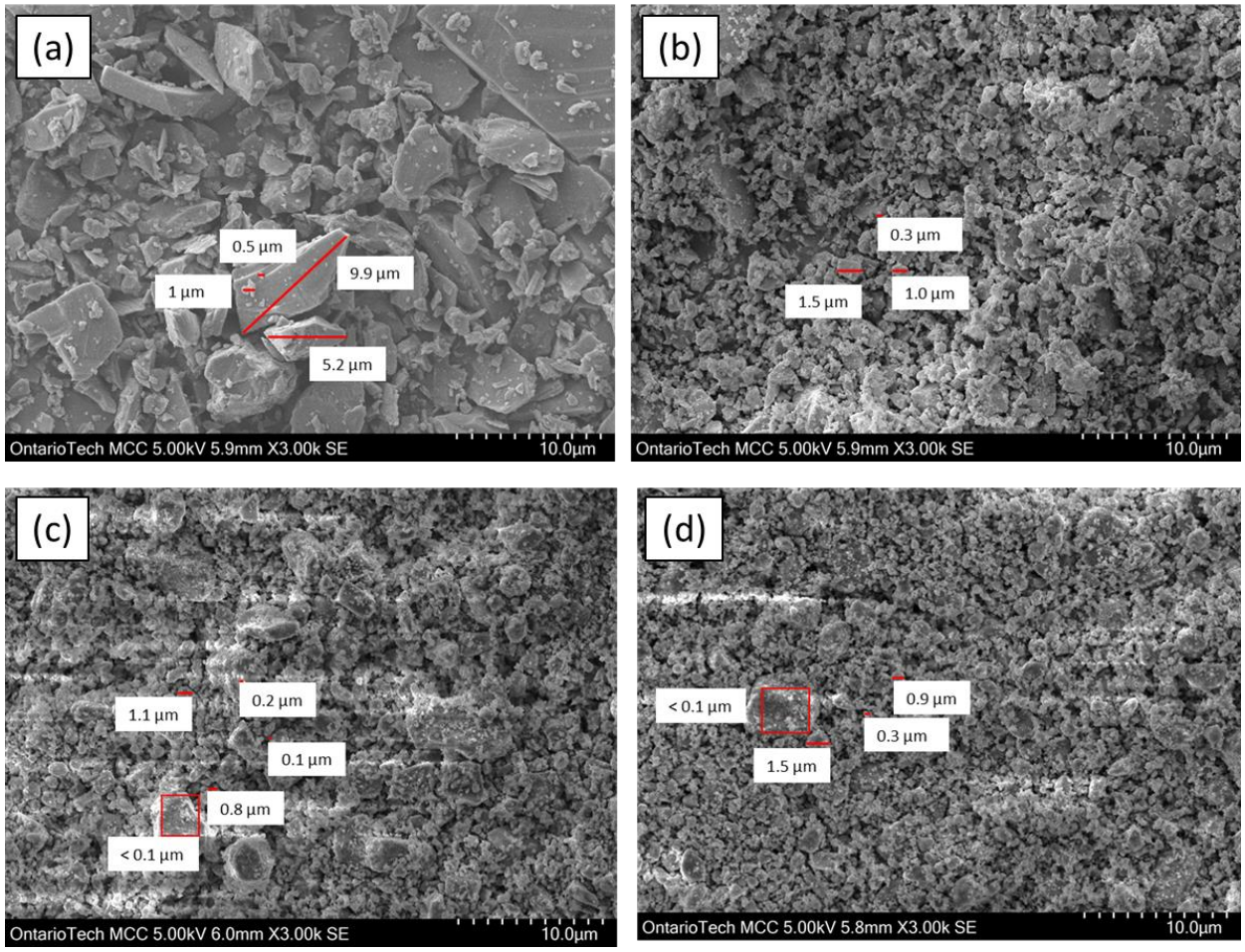

Figure 4.1. SEM images obtained for fresh Silicon powder (a), and Silicon ball milled for 4h (b), 24h (c), and 72h (d).

BET was employed to investigate the influence of varying Si particle size on the overall TOS support surface area, where the results are presented in Table 4.1. As ball milling duration increased up to 72 h, the surface area of the Si powder was observed to increase due to smaller particle size. Ball milling was ceased after 72 h due to the surface area approaching a plateau at ca. 19 $m^2 g^{-1}$ (Table 4.1).

A new TOS support was synthesized from this optimized Si powder (ball milled for 72 h) combined with TiO_2 anatase to produce the TOS (Si BM 72 h) support. This support possessed a surface area of 6.5 $m^2 g^{-1}$ which was reduced from 17.8 $m^2 g^{-1}$ observed for the conventional TOS

support. This decrease was attributed to the smaller Si particles blocking and inhibiting the pores of the larger Ti particles (mesh size 325 or up to 40 µm). The isotherm for this support is shown in Figure 4.2 which shows a type V isotherm which is indicative of weak gas-solid interactions.[120]

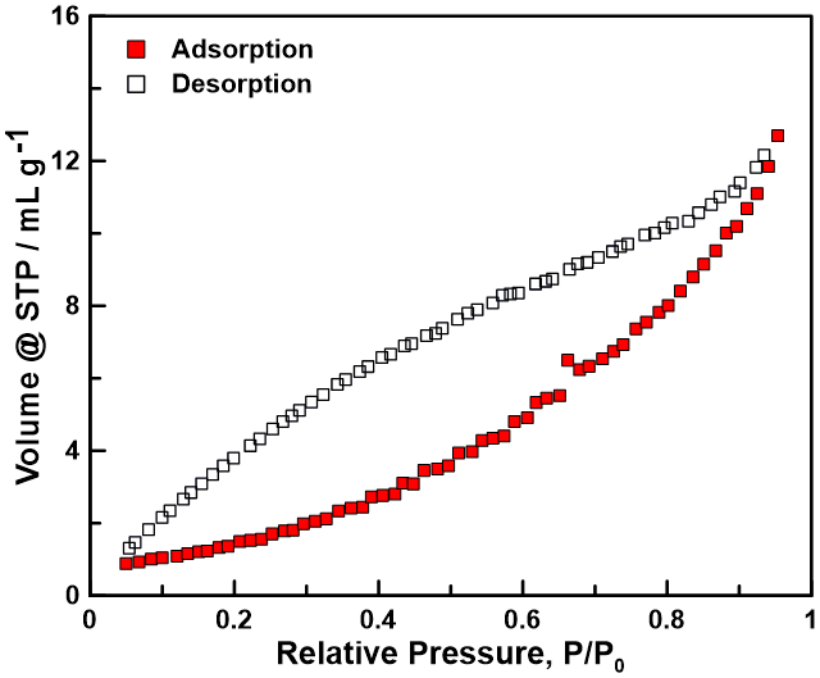

Figure 4.2. Nitrogen adsorption-desorption isotherms obtained during BET surface area analysis for the TOS 20 wt% Si (Si BM 72 h) support.

Table 4.1. Physical characterization for the ball milled Si samples and TOS (Si BM 72 h) support.

Sample	**Surface Area ($m^2 g^{-1}$)**	**Band Gap (eV)**	**Conductivity ($S cm^{-1}$)**
No Ball Milling	5.5	---	---
Si Ball milled – 4 h	11.4	---	---
Si Ball milled – 24 h	15.2	---	---
Si Ball milled – 72 h	18.9	---	---
TOS 20 wt% Si (Si BM 72 h)	6.5	0.68	1.48×10^{-2}

Crystallographic analysis was performed on the TOS 20 wt% Si (BM 72 h) support and compared with the previously synthesized TOS support. XRD patterns in Figure 4.3 indicate the Ti_3O_5 phase was the only suboxide phase present with the key reflection at 2θ = 53.43°. Metallic Si and stoichiometric SiO_2 were also observed with key reflections at 28.69° and 55.53°. There was a slight broadening observed for the Si and SiO_2 reflections which corresponded to the decrease in particle size as a result of ball milling.

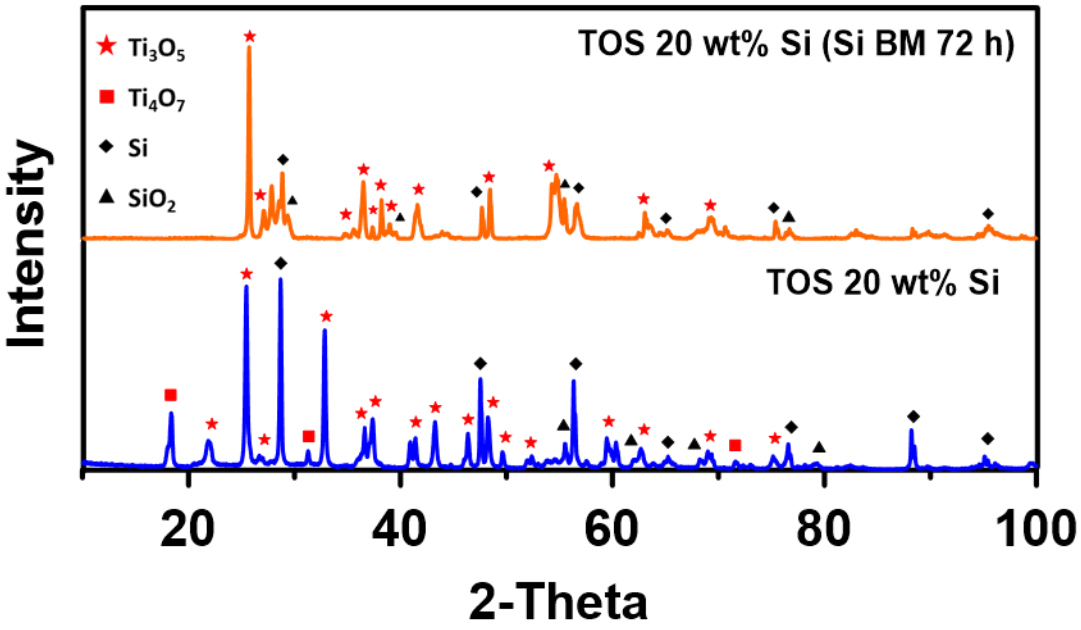

Figure 4.3. XRD patterns for the TOS support with Si powder ball milled for 72 h compared to the conventional TOS support.

To investigate electronic properties of the TOS (Si BM 72 h) support, a Tauc plot (Figure 4.4) was constructed to estimate the band gap energy. The TOS (Si BM 72 h) support possessed a band gap of 0.68 eV (Figure 4.5a) which was slightly wider than the 0.50 eV band gap observed for the conventional TOS support. The measured electronic conductivity for the TOS (Si BM 72 h) support was 1.48×10^{-2} S cm^{-1} (Figure 4.5b), compared to the 1.24 S cm^{-1} measured for the

conventional TOS support. The decrease in conductivity was attributed to the smaller grain boundaries associated with the ball milled Si particles through the titania lattice which impede electronic conductivity. This is in agreement with literature where it has been reported that smaller grain boundaries possess a variety of defects/vacancies which can impede electronic conductivity within the material, in other words, the mean free path of electrons is reduced.[140]

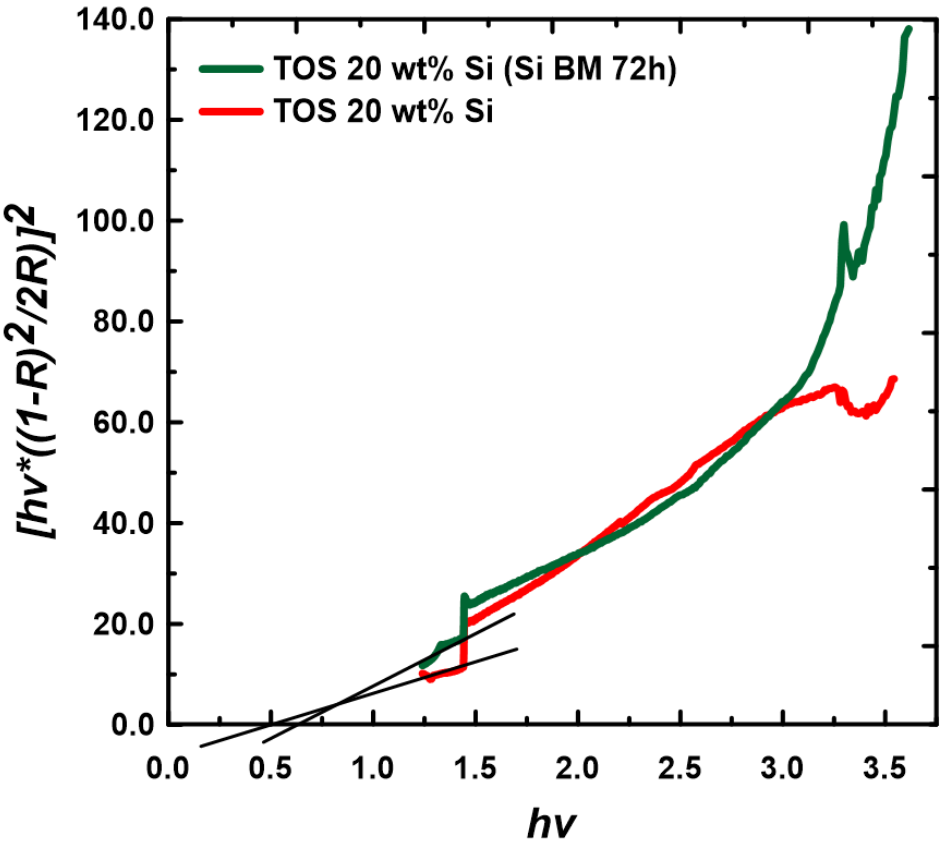

Figure 4.4. Tauc plot for the determination of band gap energies for the TOS (Si BM 72h) support with the Tauc plot for the conventional TOS support as reference.

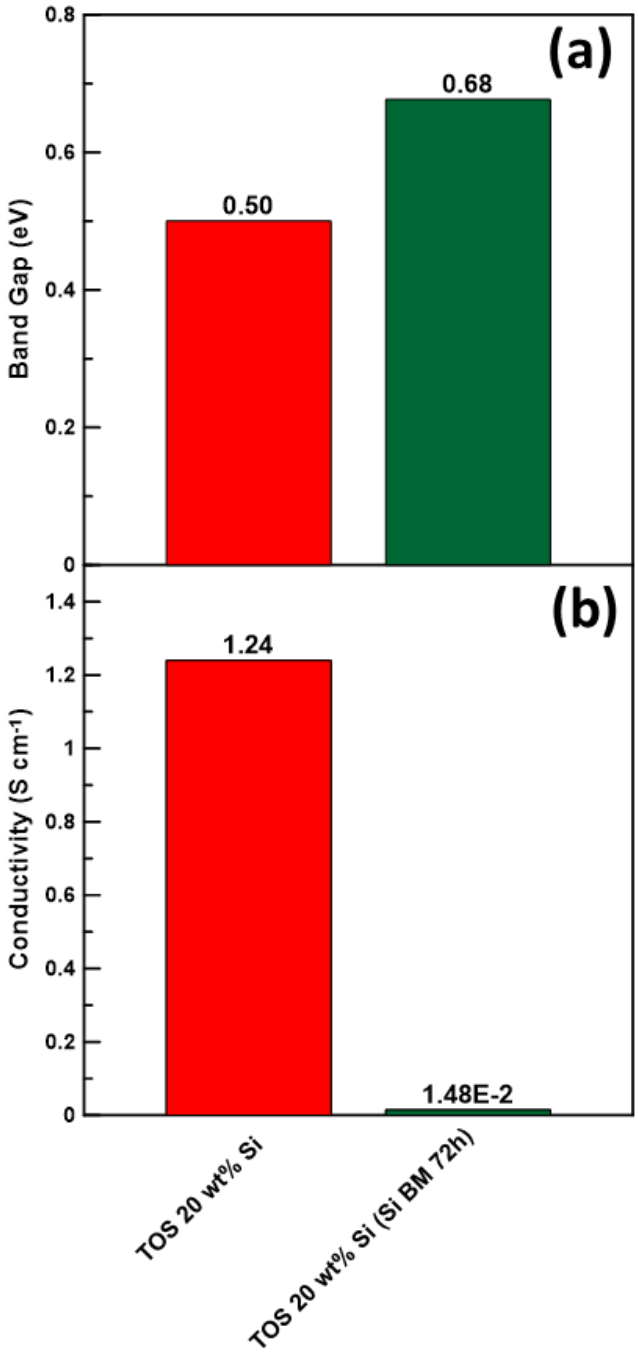

Figure 4.5. (a) The obtained band gap energy and (b) the electronic conductivity for the TOS (Si BM 72h) support with the conventional TOS support as reference.

4.1.2 Electrochemical Characterization

The durability of the TOS (Si BM 72 h) support was characterized via electrochemical testing. Support ink was prepared as a mixture of 3:1 ultrapure water and isopropanol, 5 wt% Nafion® solution, and 5-7 mg of support powder. Once sonicated for 10 min and stirred for 12 h, the resulting ink was deposited on the electrode surface and heated to achieve a thin film. A 20,000 cycle ADT was performed in N_2-saturated 0.5 M H_2SO_4 solution and scanned over the range of 0.05 – 1.25 V_{RHE} at 500 mV s^{-1} (Figure 4.6-Figure 4.9). The TOS (Si BM 72 h) support displayed good durability and no signs of corrosion during the test. The typical redox peaks formed between 0.55-0.65 V_{RHE} indicative of the Ti^{4+}/Ti^{3+} redox couple. However, compared to the conventional TOS support, the initial CV profile of the TOS (Si BM 72 h) support deviated from the ideal box-like profile which is a feature of the low electronic conductivity (Figure 4.7).

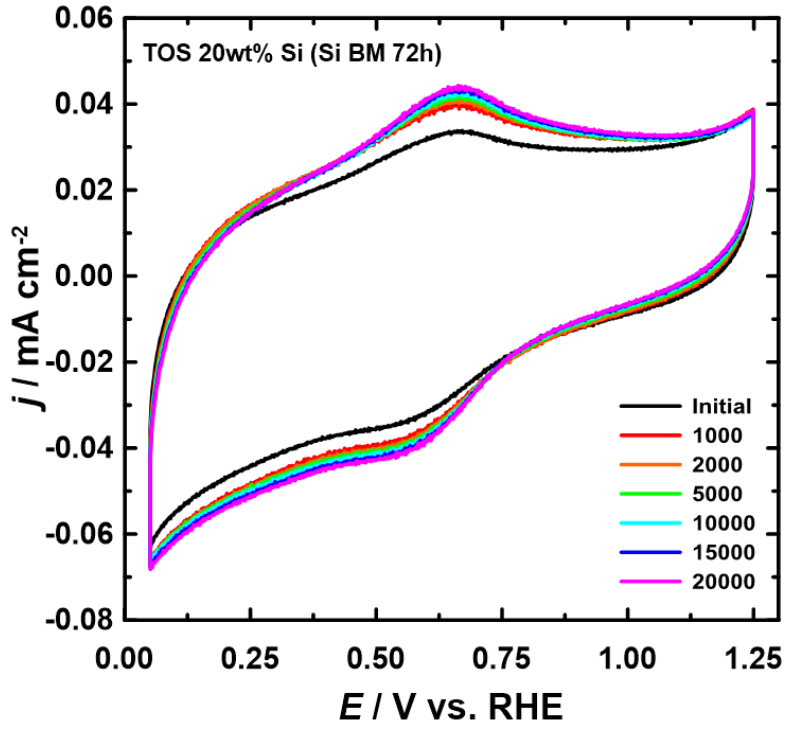

Figure 4.6. (a) Half-cell CV response for the TOS 20 wt% Si (Si BM 72h) support to a 20,000 potential cycle ADT in N_2-saturated 0.5 M H_2SO_4 solution, recorded at 200 mV s^{-1} at 22 $\pm$3°C.

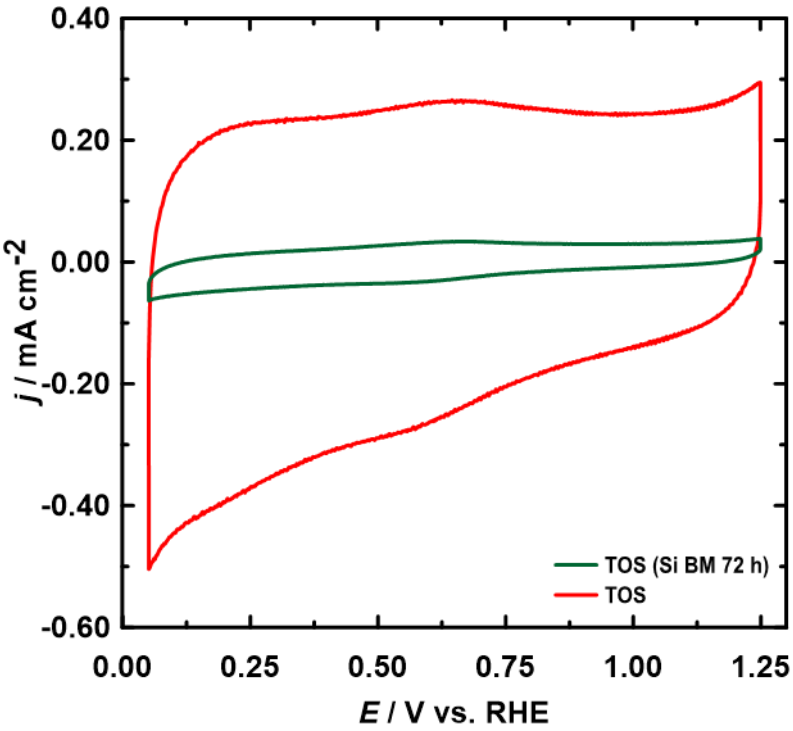

Figure 4.7. Initial half-cell CV response of the TOS (Si BM 72 h) support compared to the conventional TOS support under ADT conditions.

EIS analysis was performed on the TOS support at a DC bias potential of 0.425 V_{RHE} with the data represented as Nyquist and capacitance plots (Figure 4.8a,b). The Nyquist plot in Figure 4.8a showed little variation with respect to cycle number and expansion of the high frequency region (Figure 4.8c) revealed a longer Warburg length relative to the conventional TOS support (Figure 4.9a,c) which is a sign of higher electronic resistance within the support layer due to the smaller Si particles dispersed throughout the Ti_3O_5 lattice structure impeding electron mobility. The capacitance plot showed a slight increase in capacitance from the initial cycle of the ADT and then remained stable over the course of the test which indicated that the surface area of the support remained unchanged (Figure 4.8b,d). The capacitance was observed to be quite low for this support compared to the conventional TOS support (Figure 4.9b,d). This was due to greater dispersion of the smaller Si particles throughout the Ti_3O_5 structure which block the pores of the

suboxide and limit access to the electrolyte, effectively reducing the accessible surface area of the support.

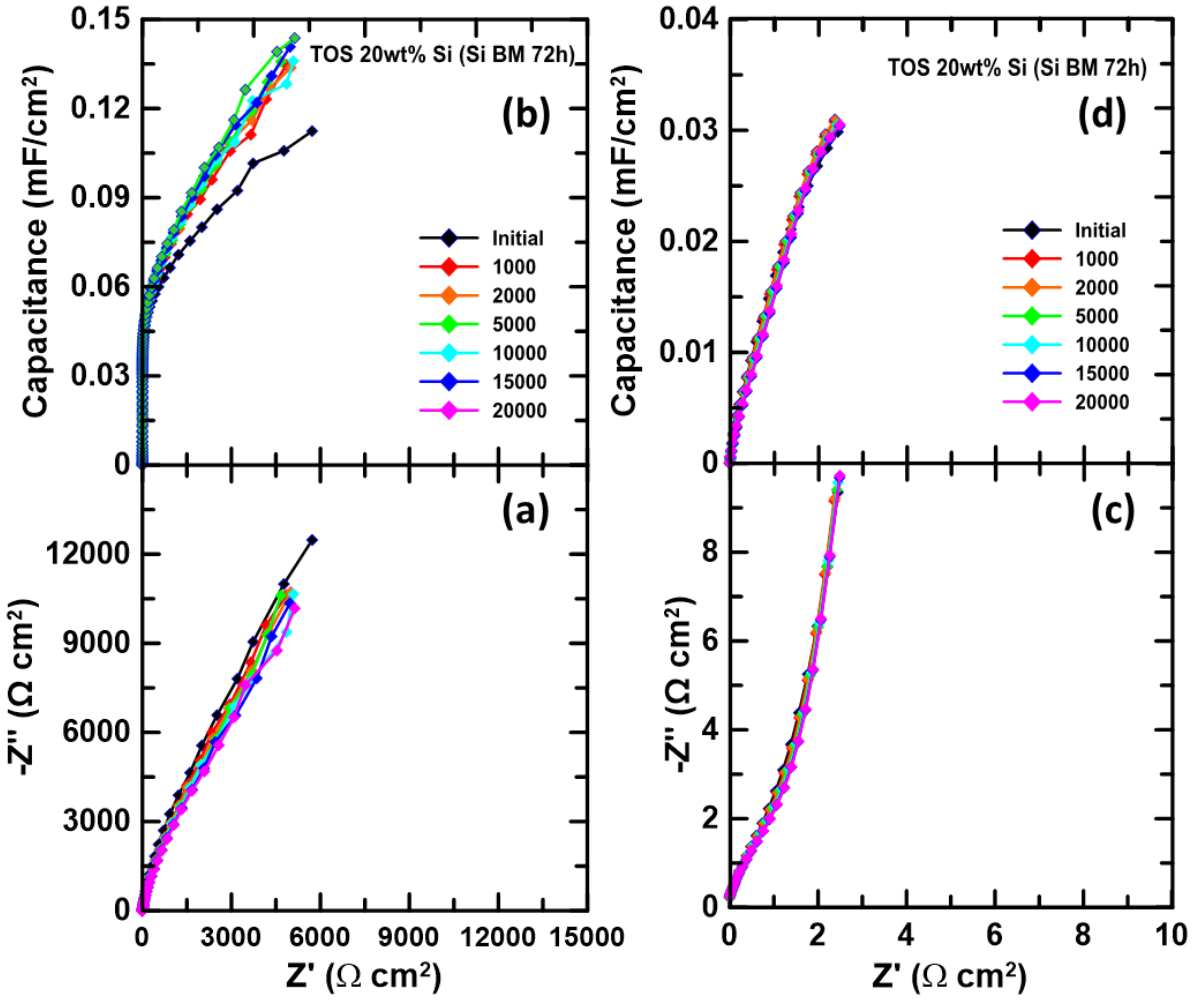

Figure 4.8. EIS response to a 20,000 potential cycle ADT for the TOS 20 wt% Si (Si BM 72 h) support. Data presented as Nyquist (a) and capacitance (b) plots obtained at a DC potential bias of 0.425 V_{RHE}. The expansion of the Warburg region within the Nyquist and capacitance plots is shown in (c) and (d), respectively.

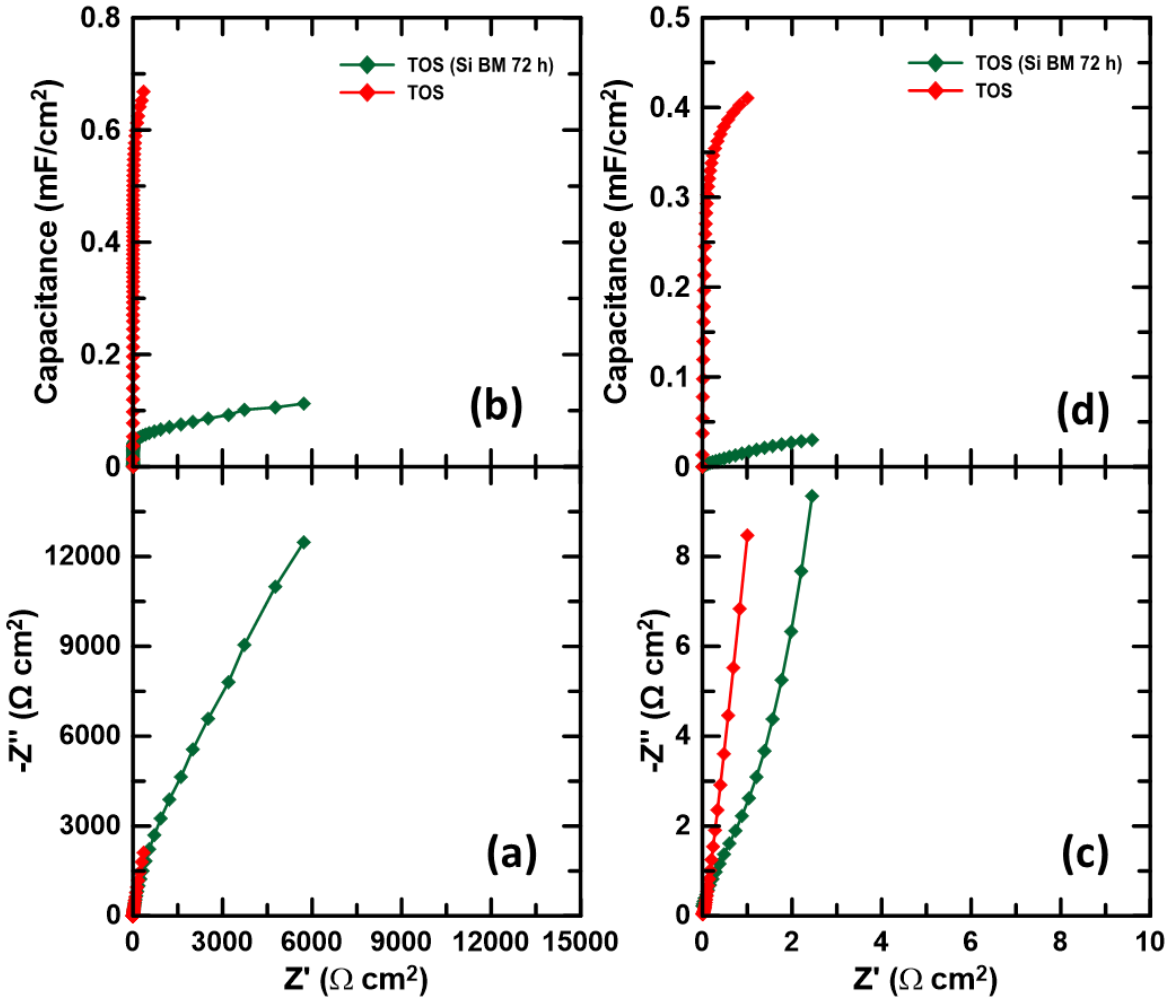

Figure 4.9. Initial EIS responses for TOS (Si BM 72 h) compared to the conventional TOS support presented as (a) Nyquist and (b) capacitance plots. The expansion of the Warburg region within the Nyquist and capacitance plots is shown in (c) and (d), respectively.

Through the combination of physical and electrochemical characterization techniques, the TOS (Si BM 72 h) support was determined to be a non-practical support for FC application. While possessing an acceptable band gap, the conductivity was 2 orders of magnitude lower than that of the conventional TOS support. BET measurements revealed the surface area of the support was much lower than that of the TOS support as a result of the Si NPs blocking access to the pores. The low support surface area and conductivity (ie. high electronic resistivity) were confirmed with the capacitance and Nyquist plots, respectively. Thus, it was necessary to seek

another method to achieve a TOS support with acceptable conductivity and surface area.

4.2 Investigating TiO_2 Nanoparticles as Precursor for TOS support

The previous section involved the incorporation of smaller Si particles into the TOS framework however, it was evident the reduced particle size in relation to the larger Ti particles impeded electronic conductivity. This section will explore the use of *in-situ* grown TiO_2 nanoparticles, 15-20 nm in size, in combination with the ball milled Si NPs to produce the TOS_{SG} support with a high surface area. In contrast to the conventional TOS support synthesis which possessed a metal suboxide core, this sol-gel process yields a Si core encapsulated by *in-situ* grown TiO_2 (Figure 4.10). It is expected that as particle size is reduced, the surface area will increase, in addition to a variety of other improvements to electrochemical performance.

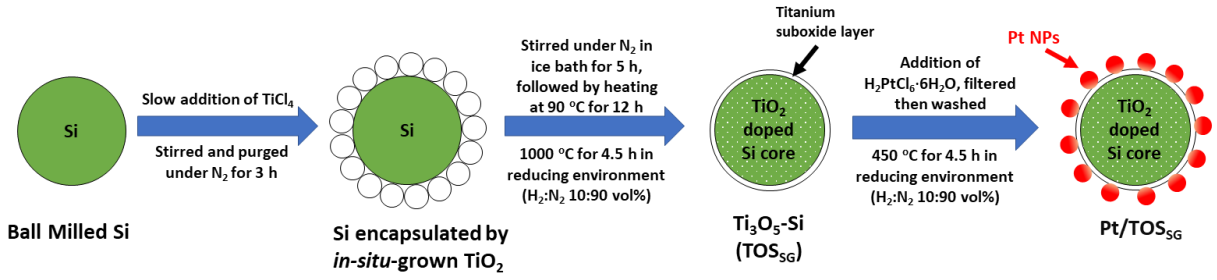

Figure 4.10. Reaction schematic for the synthesis of the TOS_{SG} support and Pt/TOS_{SG} catalyst.

4.2.1 Materials Characterization

4.2.1.1 X-Ray Diffraction

To investigate the crystallographic structure of the TOS_{SG} support, XRD patterns were obtained and compared with the previously synthesized TOS support (Figure 4.11). The support structure was comprised primarily of the Ti_3O_5 phase with the key reflection at 2θ = 54.66°. Si was also present in both the metallic (Si) and metal oxide (SiO_2) phases with key reflections at 2θ

= 28.69° and 29.05°, respectively.

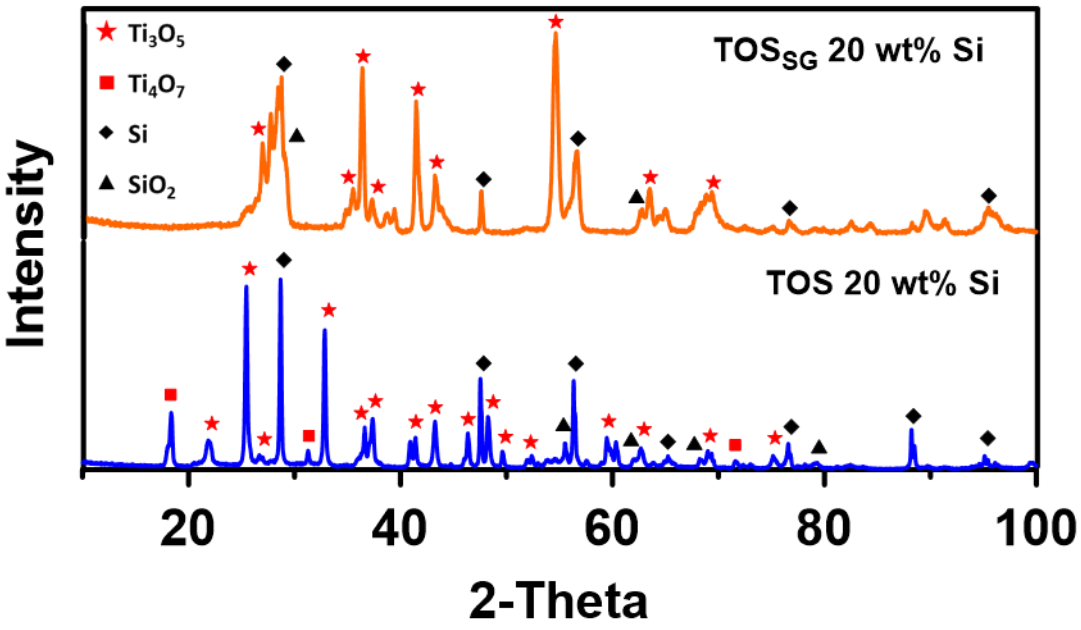

Figure 4.11. XRD pattern obtained for the optimized TOS_{SG} support with the conventional TOS support XRD pattern for reference.

4.2.1.2 Transmission Electron Microscopy

To investigate the morphology of the TOS_{SG} support, TEM images were obtained at different magnifications (Figure 4.12). The sol-gel process resulted in spherical TOS_{SG} particles which were observed with better distribution of Ti, O, and Si NPs compared to the Si agglomerations observed for the conventional TOS support. This contributed to the larger surface area determined for the TOS_{SG} support. Better particle distribution is expected to increase the concentration of surface -OH groups that Pt NPs adsorb onto, which should lead to better Pt utilization in the catalyst.

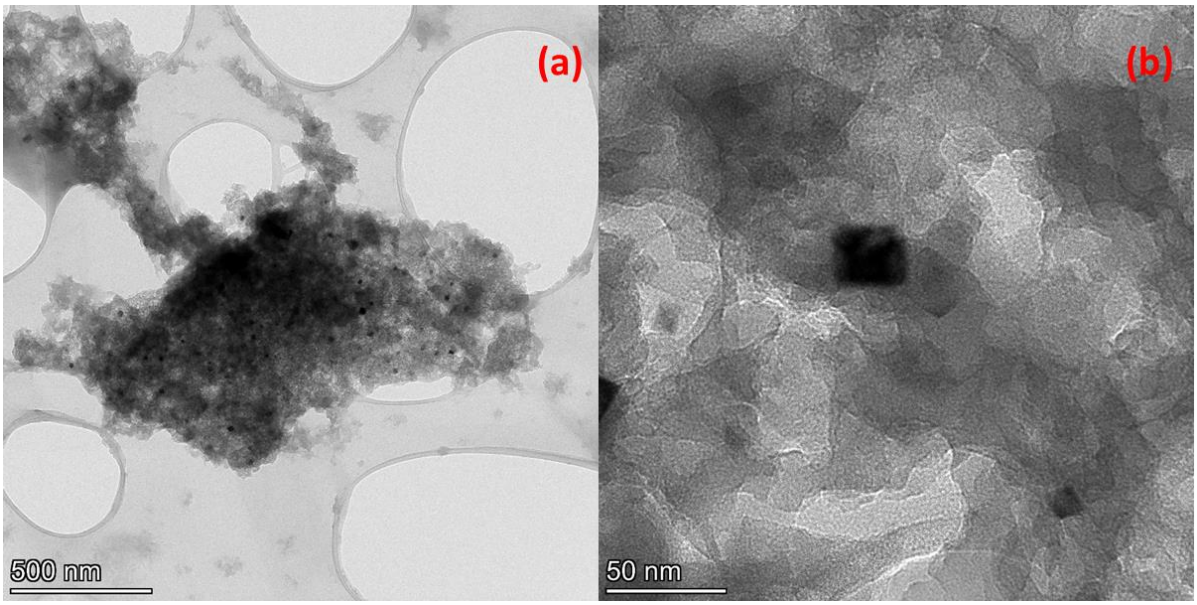

Figure 4.12. TEM images of the TOS_{SG} 20 wt% Si support at (a) 500 nm and (b) 50 nm.

4.2.1.3 Brunauer-Emmett-Teller Surface Area Analysis

BET analysis was also performed to confirm whether the combination of *in-situ* grown TiO_2 and ball milled Si influenced the surface area of the TOS_{SG} support. The surface area of TOS_{SG} was measured to be 139.9 $m^2\ g^{-1}$ which was a substantial increase in surface area from the conventional TOS support synthesized from precursor materials with mesh sizes of 325 (up to 40 µm in size). This demonstrated the successful increase in TOS support surface area resulting from smaller precursor materials and a novel sol-gel approach. Figure 4.13 shows a type IV isotherm for the TOS_{SG} support which indicates the support is mesoporous.[141] The material characterization results for the TOS_{SG} support are summarized in Table 4.2.

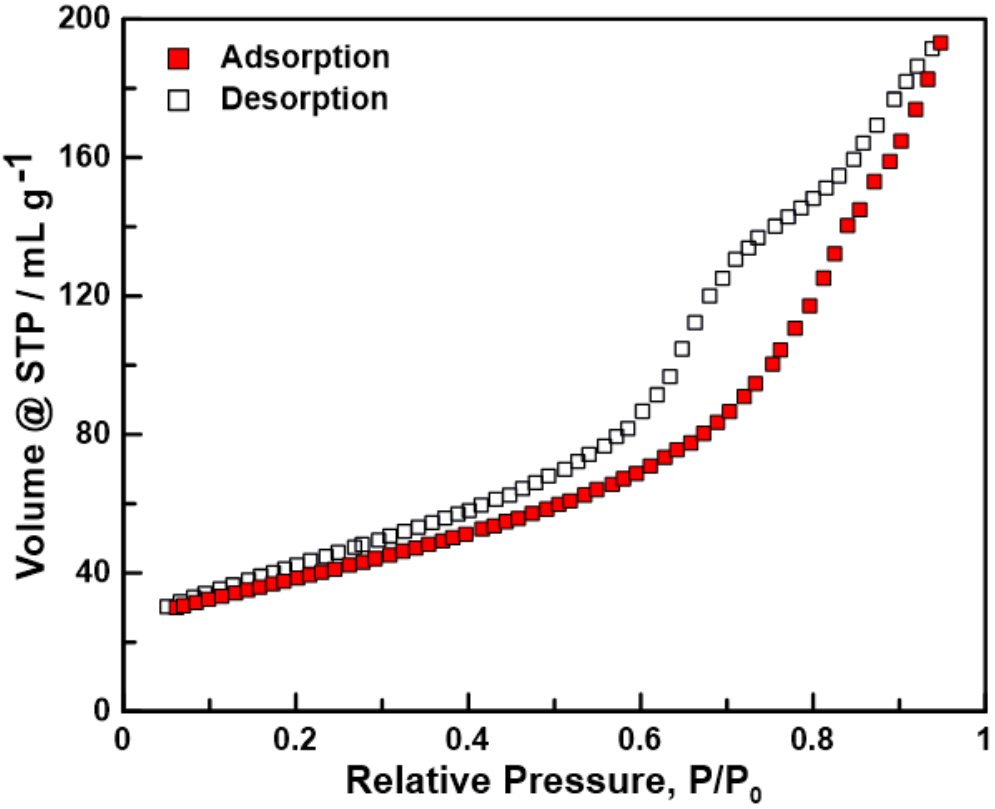

Figure 4.13. Nitrogen adsorption-desorption isotherms obtained during BET surface area analysis for the TOS_{SG} 20 wt% Si support.

Table 4.2. Summary of material characterization tests performed on the TOS_{SG} support.

Support	Surface Area (m^2 g^{-1})	Band Gap (eV)	Electronic Conductivity (S cm^{-1})
TOS_{SG} 20 wt% Si	13.9 x 10^1	0.30	0.31

4.2.1.4 Optical Band Gap and Electronic Conductivity

To investigate electronic properties of the TOS_{SG} support, a Tauc plot was constructed to estimate the band gap energy (Figure 4.14). The TOS_{SG} support possessed a band gap of 0.30 eV (Figure 4.15a) which was narrower than the 0.50 eV band gap observed for the conventional TOS support. This demonstrated the relationship between support particle size and physical properties of the bulk material indeed influences the band gap size. The band gap of crystalline

semiconductors has been reported to be a function of particle size.[142–144] As the threshold from bulk to nanoparticle properties is approached by reducing the particle size, the concentration of surface defects increases. One such defect includes the oxygen vacancies that form within thermally annealed metal oxides and serve as electron recombination centers within the band gap. This simultaneously reduces the band gap and promotes electron migration between the valence and conduction bands. The measured electronic conductivity for the TOS_{SG} support was 0.31 S cm^{-1} (Figure 4.15b), compared to the 1.24 S cm^{-1} measured for the conventional TOS support. The decrease in conductivity was attributed to the smaller grain boundaries between the ball milled Si particles and smaller Ti particles.

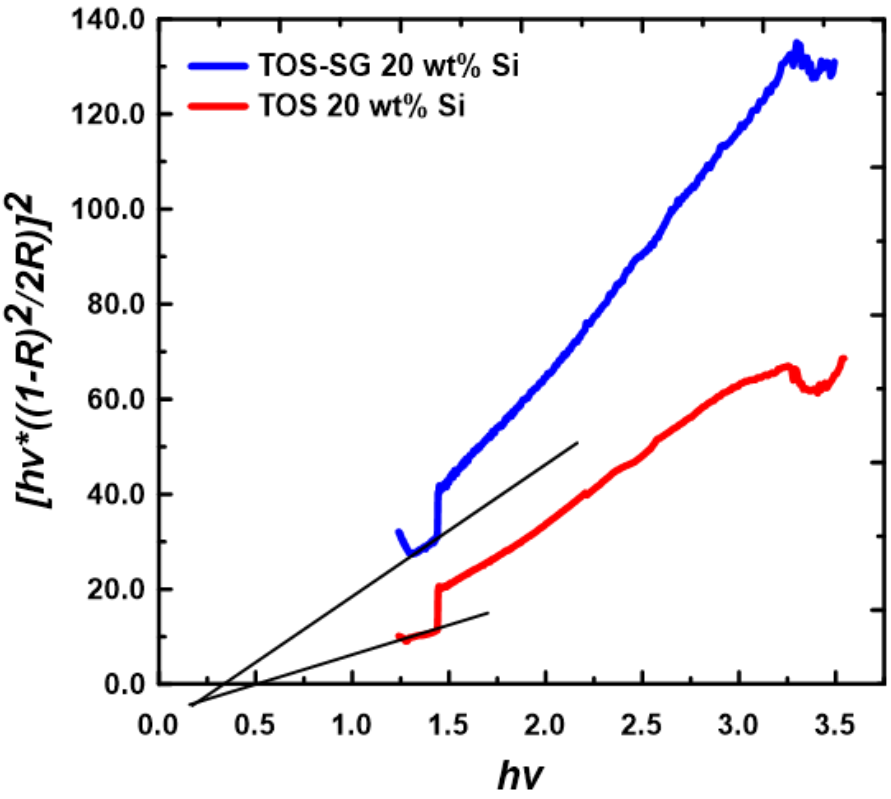

Figure 4.14. Tauc plot for the determination of the band gap energy of the TOS_{SG} support with the conventional TOS support as reference.

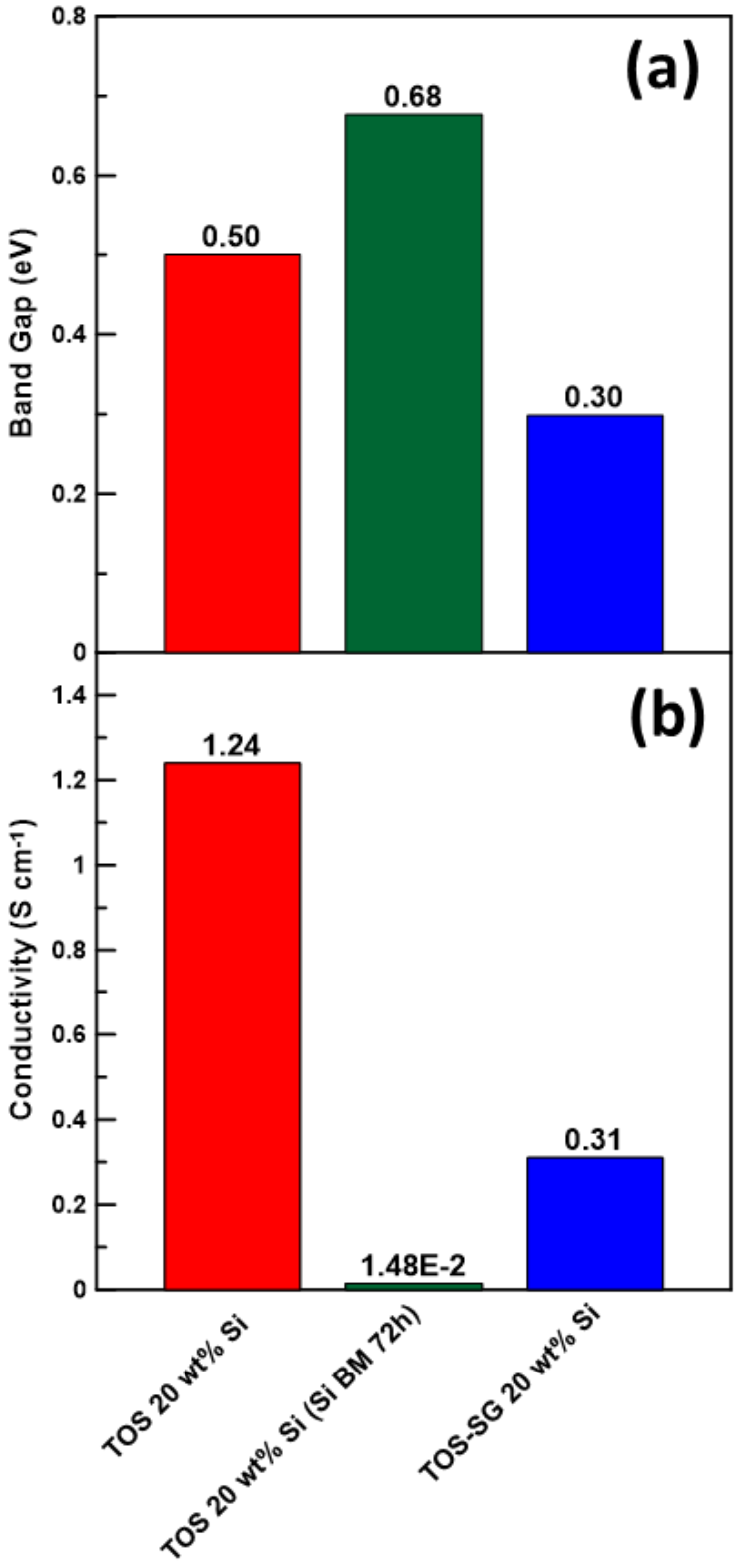

Figure 4.15. (a) The band gap (in eV) and (b) the measured electronic conductivity (in S cm^{-1}) for the TOS_{SG} support with the conventional TOS support as reference.

4.2.2 Electrochemical Characterization

4.2.2.1 Cyclic Voltammetry and Electrochemical Impedance Spectroscopy

The durability of the TOS_{SG} support was characterized via electrochemical testing. Support ink was prepared as a mixture of 3:1 ultrapure water and isopropanol, 5 wt% Nafion® solution, and 5-7 mg of support powder. Once sonicated for 10 min and stirred for 12 h, the resulting ink was deposited on the electrode surface and heated to achieve a thin film. The durability of the TOS_{SG} support was assessed using the 20,000 potential cycle ADT under N_2-saturated 0.5 M H_2SO_4 solution and scanned over the range of 0.05 – 1.25 V_{RHE} at 500 mV s^{-1} (Figure 4.16). Compared with the conventional TOS support, the TOS_{SG} support demonstrated good durability, high capacitance, and displayed no signs of corrosion; initial cycles for the ADT for each support are compared in Figure 4.17. Typical Ti^{4+}/Ti^{3+} redox peaks were observed between 0.55-0.65 V_{RHE} and the CV profile displayed a box-like shape which indicated good electronic conductivity and a high surface area.

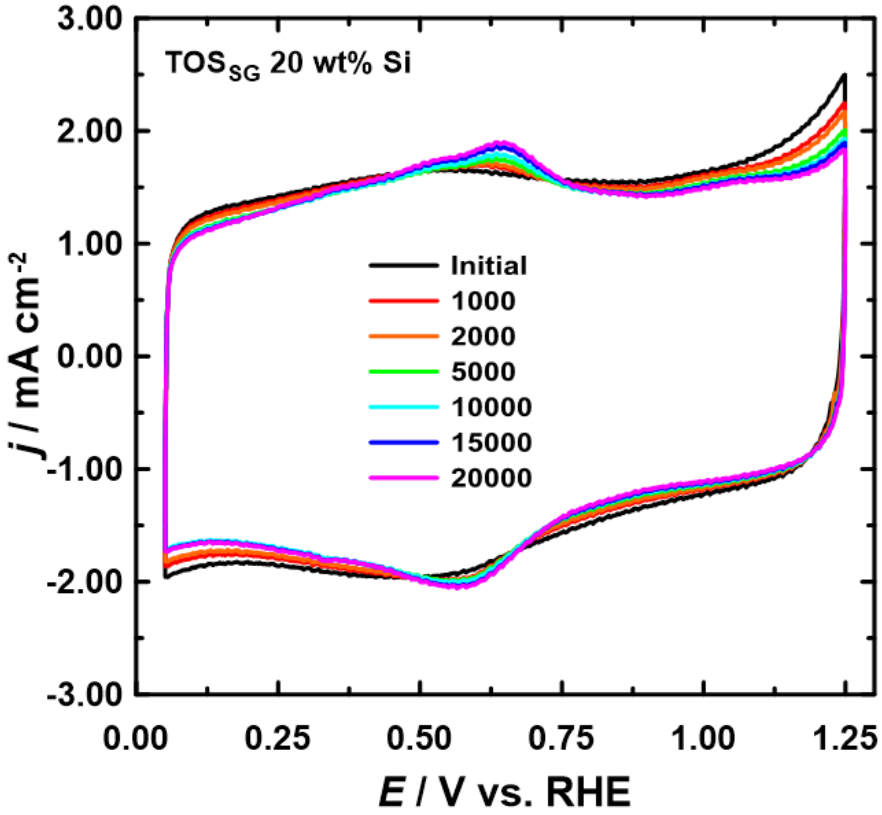

Figure 4.16. Variation in CV response for the optimized TOS_{SG} support under ADT conditions in N_2-saturated 0.5 M H_2SO_4 solution.

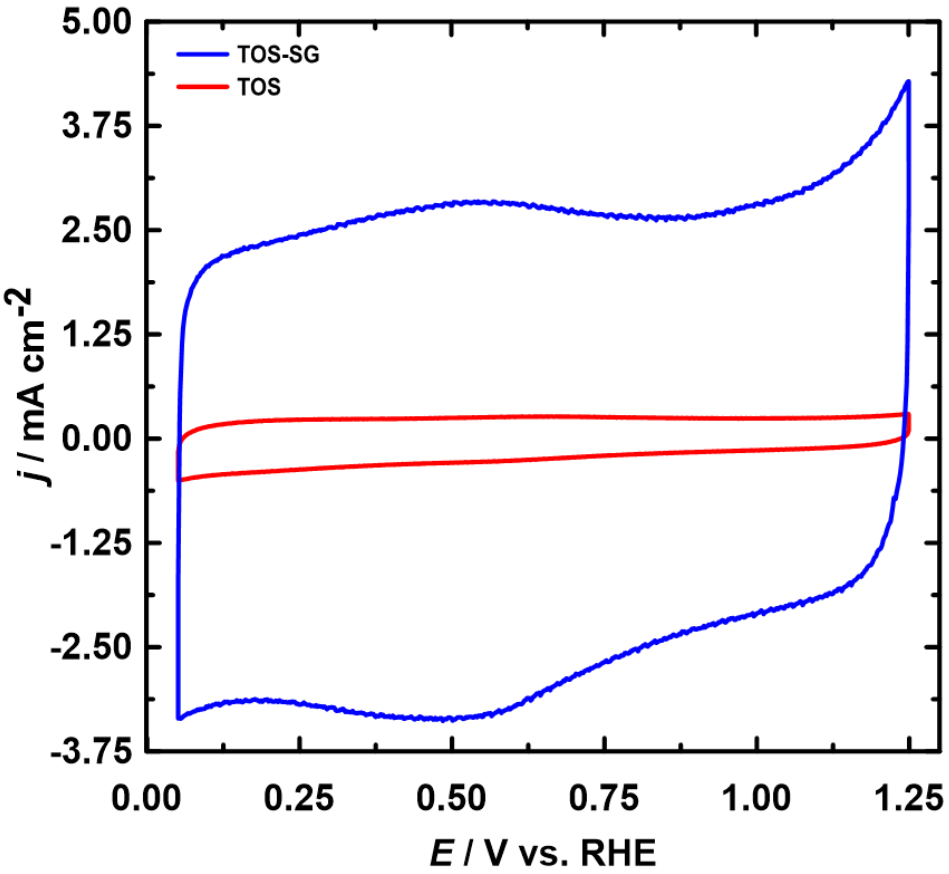

Figure 4.17. Initial half-cell CV response of the TOS_{SG} support compared to the conventional TOS support under ADT conditions.

EIS analysis was performed on the TOS_{SG} support at a DC bias potential of 0.425 V_{RHE} with the data represented as Nyquist and capacitance plots (Figure 4.18a,b). The Nyquist plot remained virtually constant with respect to cycle number and expansion of the high frequency region (Figure 4.18c) revealed a relatively short Warburg length which indicated low resistivity within the support layer due to the smaller Ti_3O_5 lattice structure. The capacitance of TOS_{SG} was also observed to remain constant throughout the ADT indicating the surface area remained unchanged. It is worth noting the limiting capacitance was significantly greater than the conventional TOS support suggesting remarkable capacitive capabilities (Figure 4.19). Due to the exceptional durability, low resistivity, and high surface area of the TOS_{SG} support, the activity

toward the ORR was investigated next.

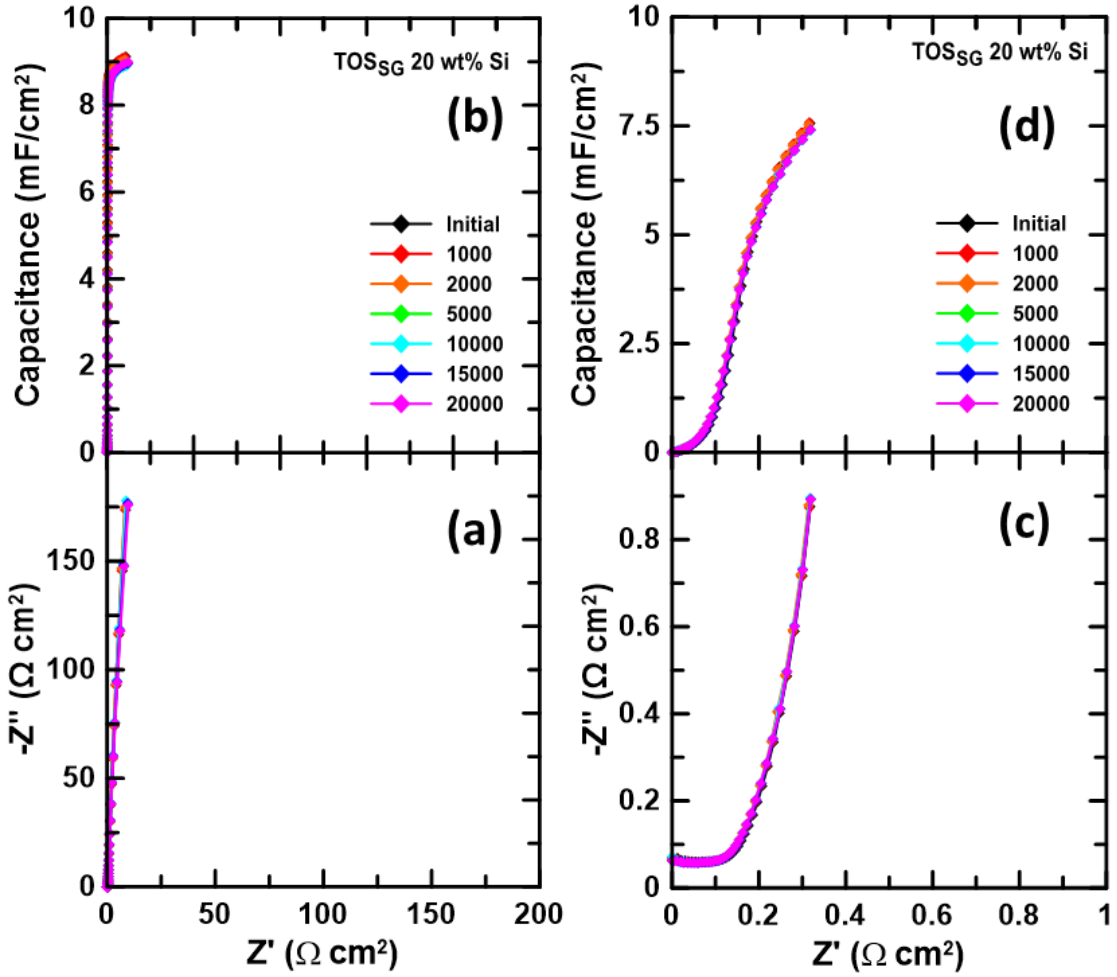

Figure 4.18. EIS responses for the optimized TOS_{SG} support under ADT conditions. The data is presented as Nyquist (a) and capacitance (b) plots, where (c) and (d) show the expansion of the Warburg region obtained at a DC potential bias of 0.425 V.

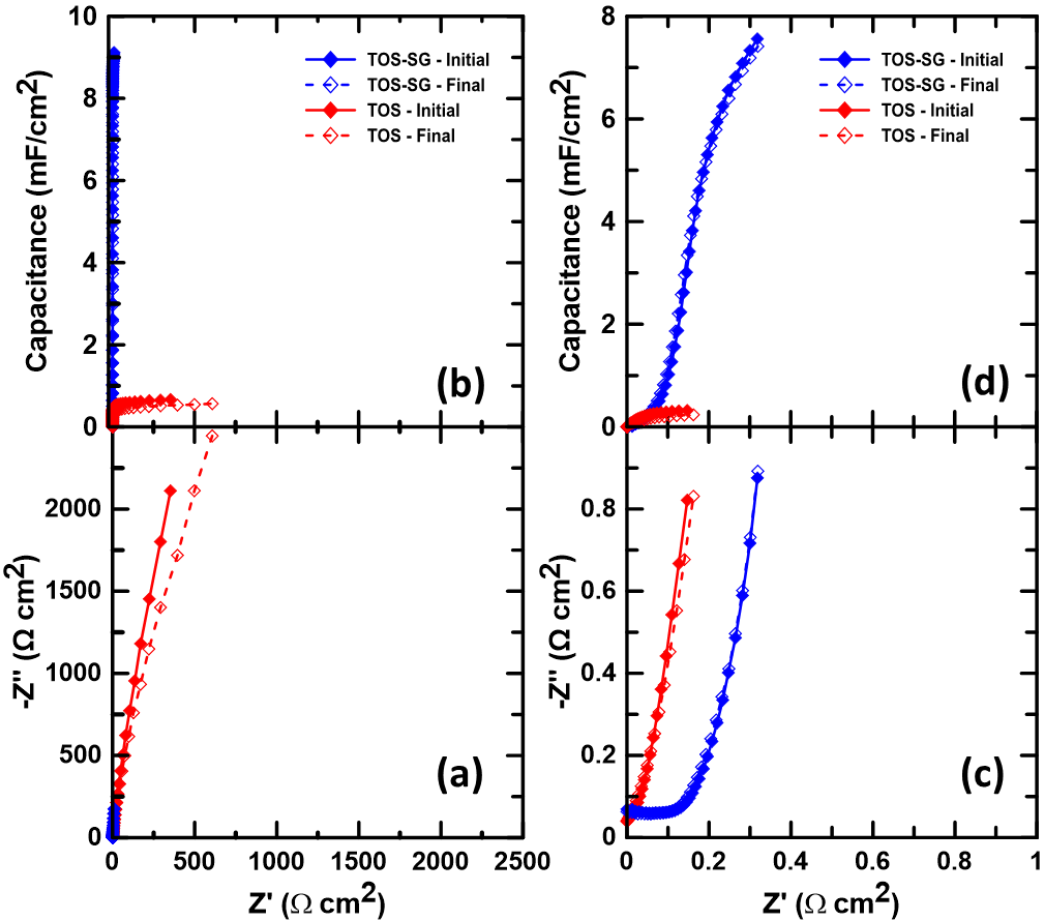

Figure 4.19. Initial EIS responses for TOS_{SG} compared to the conventional TOS support presented as (a) Nyquist and (b) capacitance plots. The expansion of the Warburg region within the Nyquist and capacitance plots is shown in (c) and (d), respectively.

The TOS_{SG} support was then platinized to form the Pt/TOS_{SG} catalyst. XRD was performed to confirm the Pt NP size supported on the TOS_{SG} support (Figure 4.20). The XRD pattern for the Pt/TOS_{SG} catalyst revealed typical metallic Pt reflections at 2θ = 39.98° {111}, 46.51° {200}, 67.69° {220}, 81.60° {311}, and 86.27° {222}. The Pt NPs favored the {111} orientation as indicated by the broad, intense peak at 2θ = 39.98°. The Debye-Scherrer formula was employed using peak position and full-width half-maximum (FWHM) of the Pt grains in the {311} and {222} orientation to quantify the Pt grain size. The average Pt grain size in the Pt/TOS_{SG} catalyst was determined to be 3 nm which compared favorably against the Pt/C catalyst (2 nm) and the Pt/TOS catalyst (7

nm).

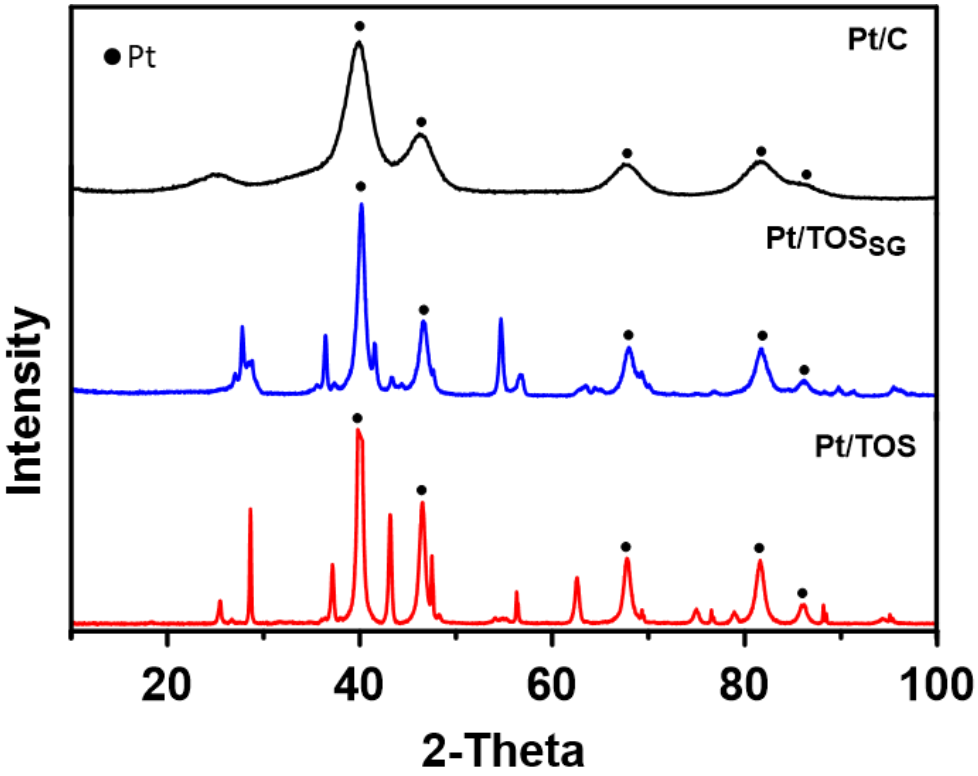

Figure 4.20. XRD pattern obtained for the Pt/TOS$_{SG}$ catalyst with the Pt/TOS and commercial Pt/C catalysts for reference.

To investigate the morphology of the Pt/TOS$_{SG}$ catalyst and confirm the Pt grain size, TEM images were obtained at different magnifications (Figure 4.21). The Pt grain size was observed to be ca. 2-4 nm in size which is in good agreement with XRD analysis. The TEM images revealed better distribution of Pt NPs for the Pt/TOS$_{SG}$ catalyst which could be further explained by the homogenous distribution of Si NPs throughout the TOS$_{SG}$ support. Figure 4.22 highlights the EDX analysis which shows even distribution of Ti, O, and Si, the latter of which serves as a nucleation site for the Pt NPs due to bonding with surface -OH groups. The smaller Pt grain size and homogenous distribution of dopants within the support structure justified the larger ECSA

measured for the Pt/TOS_{SG} catalyst in contrast to that of the conventional Pt/TOS catalyst (Table 4.3).

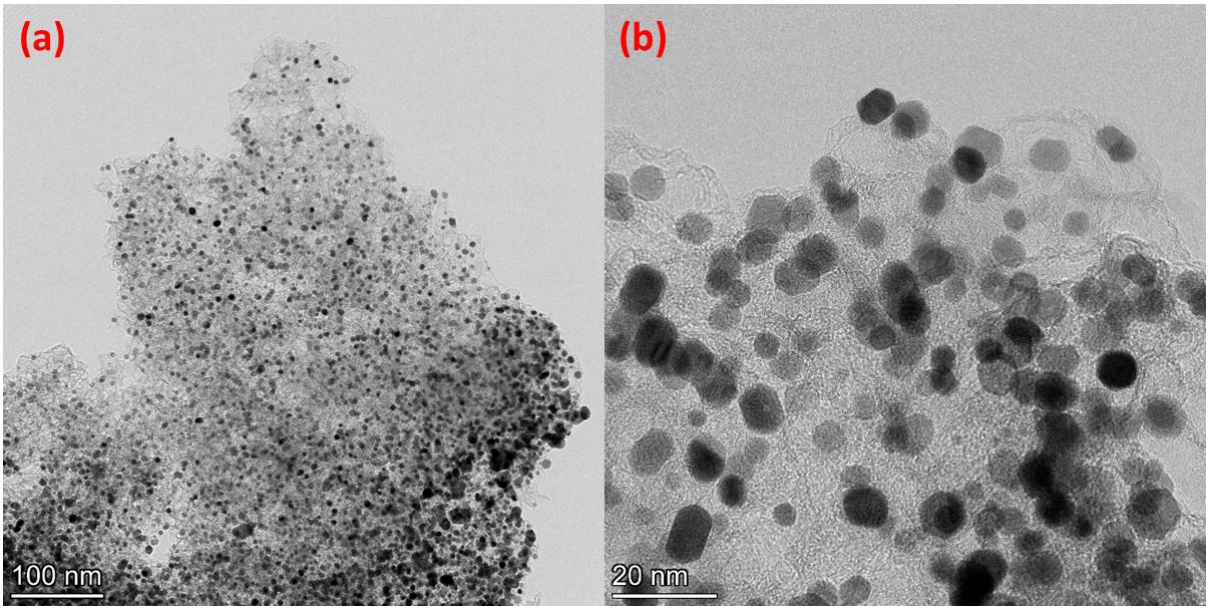

Figure 4.21. TEM images corresponding to the Pt/TOS_{SG} electrocatalyst.

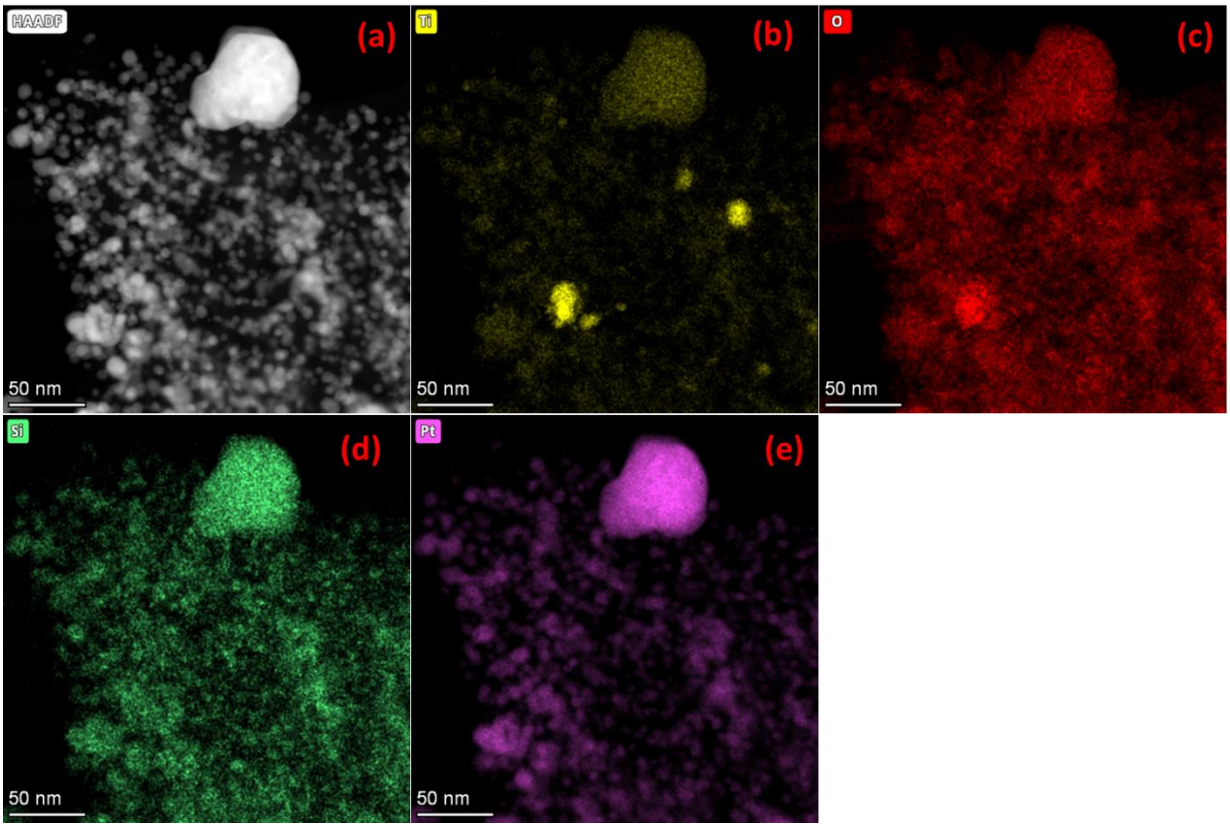

Figure 4.22. EDX analysis of the Pt/TOS_{SG} electrocatalyst represented as (a) TEM image and EDX mapping corresponding to the distribution of: (b) Ti, (c) O, (d) Si, and (e) Pt.

To investigate the stability and durability of the Pt/TOS_{SG} catalyst, a 20,000 potential cycle ADT was used. Figure 4.23a illustrates the variation in ECSA of the Pt/TOS_{SG} catalyst over the course of the ADT. The ECSA at beginning of life (BOL) for Pt/TOS_{SG} was 34.8 m^2 g^{-1} and only decreased ca. 16% over the course of the ADT. This demonstrates the success of the novel sol-gel approach to improve the ECSA compared to the conventional solid-state synthesis of the Pt/TOS catalyst. Indeed, the ECSA for Pt/TOS_{SG} is ca. 53% smaller than the ECSA for Pt/C, however, the durability remains intact over 20,000 potential cycles compared to Pt/C which decayed nearly 95%. This was attributed to the SMSI, which strongly anchored the Pt NPs to the TOS_{SG} support, thereby preventing particle size growth/agglomeration over the course of the ADT. The results

of the ADT are summarized in Table 4.3.

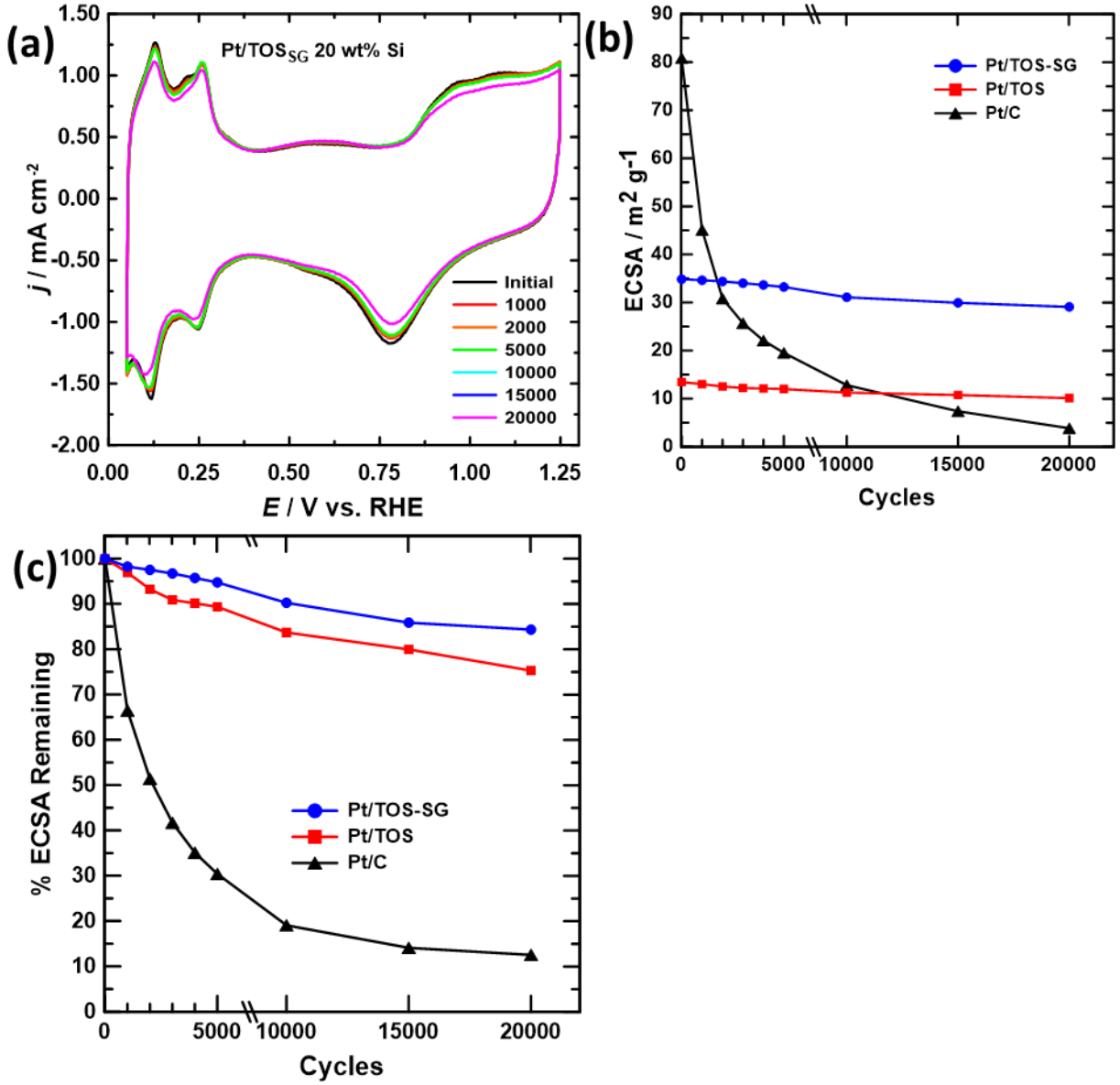

Figure 4.23. (a) Variation in CV response obtained for Pt/TOS$_{SG}$ in N_2-purged 0.5 M H_2SO_4 over a potential range of 0.05-1.25 V_{RHE} for 20,000 potential cycle ADT. The ECSA (b) and % ECSA remaining (c) are plotted as a function of ADT cycles, compared against the Pt/TOS and Pt/C catalysts.

Table 4.3. Characterization of the platinized Pt/TOS_{SG} catalyst compared with the Pt/TOS and Pt/C catalysts.

Catalyst Material	Pt size (nm)	$ECSA_{BOL}$ ($m^2\ g^{-1}$)	ECSA Remaining (%)
Pt/TOS_{SG}	3	34.8	83.4
Pt/TOS	7	13.4	75.3
Pt/C	2	80.8	4.8

The EIS response for Pt/TOS_{SG} catalyst to the 20,000 potential cycle ADT was presented as Nyquist and capacitance plots (Figure 4.24a,b) obtained at a potential bias of 0.425 V_{RHE}. With no significant changes observed within the Nyquist and capacitance plots, it was inferred that the electronic conductivity remained intact and there was no evidence to suggest support or catalyst corrosion. The limiting capacitance of this catalyst was observed to be quite high relative to that of the Pt/TOS catalyst which is a feature of the smaller particle size of the catalyst and support material. The Warburg length of the Pt/TOS_{SG} catalyst was relatively small which was observed by expanding the high frequency regions of the Nyquist and capacitance plots and projecting the Warburg length along the X-axis (Figure 4.24c,d). The short Warburg length is indicative of the ability of the Pt/TOS_{SG} catalyst to facilitate electronic and ionic conduction.

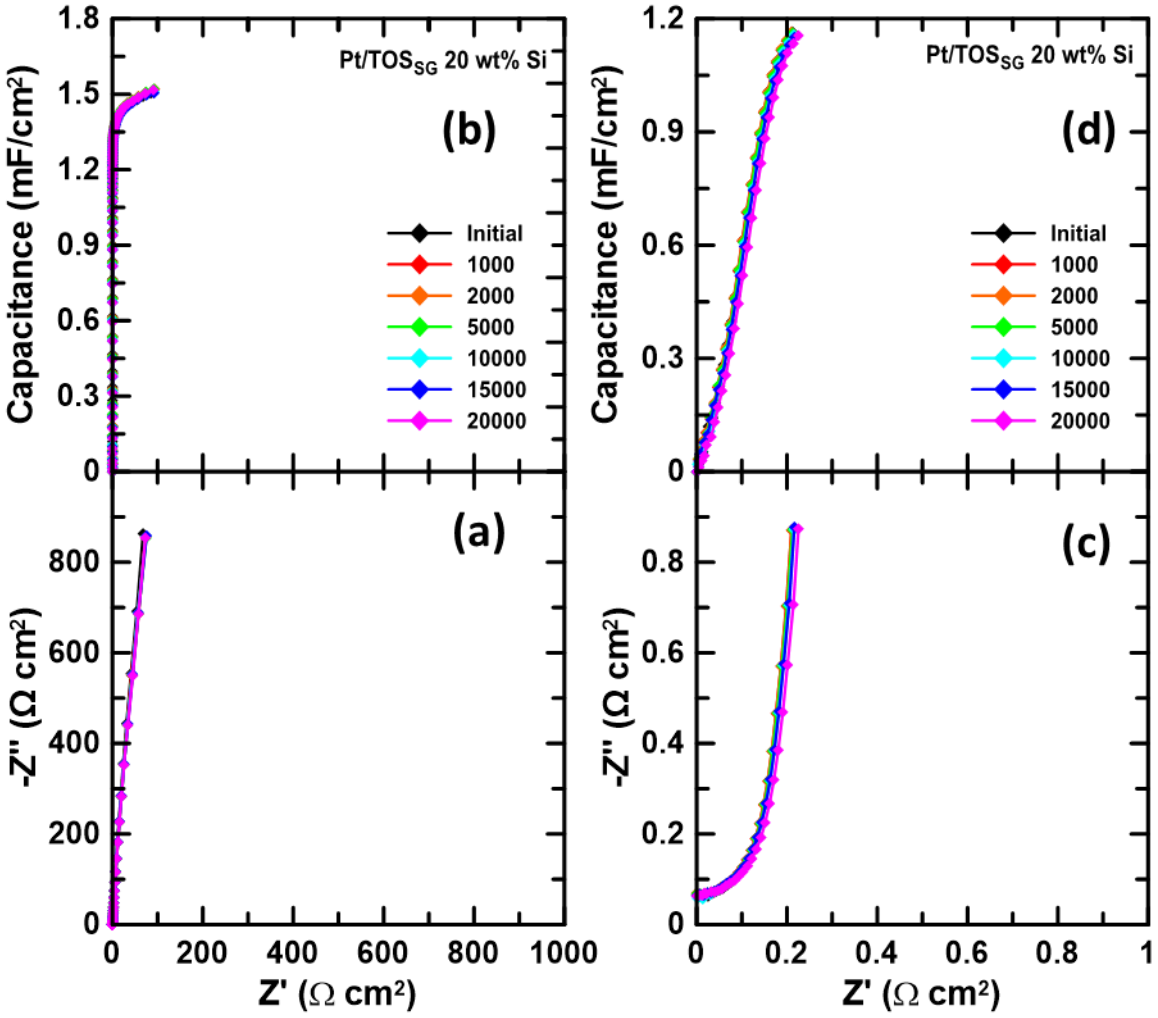

Figure 4.24. EIS responses for Pt/TOS$_{SG}$ support under ADT conditions. The data is presented as Nyquist (a) and capacitance (b) plots, where (c) and (d) show the expansion of the respective Warburg regions, obtained at a DC potential bias of 0.425 V.

4.2.2.2 Electroactivity Toward Oxygen Reduction Reaction

To investigate the influence of the TOS$_{SG}$ support on the Pt catalyst activity toward the ORR, an RDE experiment was performed before and after a 5,000 cycle ADT, in O_2-saturated 0.5 M H_2SO_4 solution at 1200 rpm (Figure 4.25). The Pt/TOS$_{SG}$ catalyst demonstrated better activity toward the ORR than the Pt/TOS catalyst, producing 0.46 mA cm^{-2} at 0.9 V_{RHE} with an onset potential of 0.92 V_{RHE} and a half-wave potential, $E_{1/2}$ of 0.82 V_{RHE}. The stability of the Pt/TOS$_{SG}$

catalyst was measured after applying a 5,000 cycle ADT which showed a decrease in $E_{1/2}$ from 0.82 to 0.75 V_{RHE}. The ECSA of Pt was determined to be 34.6 $m^2 g^{-1}$ which was significantly higher than the conventional Pt/TOS catalyst and was observed to decay by ca. 19% after 5,000 cycles. This demonstrated the remarkable durability and the ability of the TOS_{SG} support to anchor the Pt particles preventing rapid degradation as seen in the Pt/C catalyst which was observed with a ca. 70% decay in ECSA. While the Pt/TOS_{SG} catalyst did display some signs of Pt NP size growth and agglomeration via ECSA, it was attributed to residual carbon from the sol-gel process.

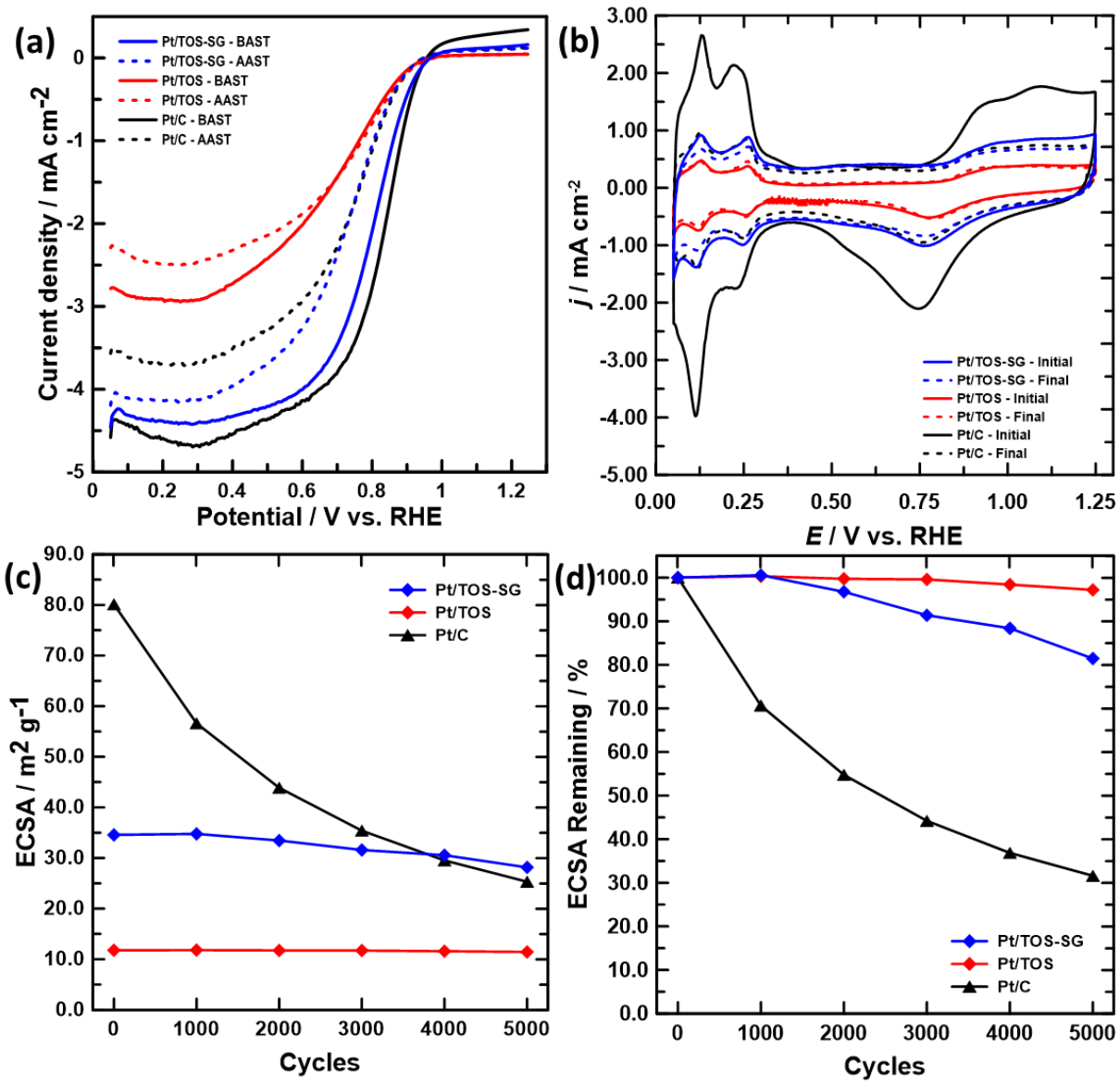

Figure 4.25. (a) Comparison of the ORR activity of the optimized Pt/TOS_{SG} catalyst compared to the Pt/TOS and commercial Pt/C catalysts; LSVs recorded at 10 mV s^{-1} in O_2-saturated 0.5 M H_2SO_4 solution (1200 rpm). The initial and final CV responses (b), variation in ECSA (c) and ECSA remaining (d) over the course of the ADT were recorded in N_2-saturated 0.5 M H_2SO_4 solution.

Table 4.4. ORR activity of Pt/TOS_{SG} catalyst compared to the Pt/TOS and commercial Pt/C catalysts.

Catalyst	Pt loading (mg cm^{-2})	I @ 0.9 (mA cm^{-2})	$E_{1/2,intial}$ (V_{RHE})	$E_{1/2,final}$ (V_{RHE})	$ECSA_{BOL}$ (m^2 g^{-1})	ECSA Remaining (%)	Electrolyte, Cycles, Scan rate (mV s^{-1})
Pt/TOS_{SG}	0.020	0.46	0.82	0.75	34.6	81.4	0.5 M H_2SO_4, 5000, 10
Pt/TOS	0.020	0.15	0.77	0.76	11.8	97.2	0.5 M H_2SO_4, 5000, 10
Pt/C	0.025	0.60	0.83	0.74	80.1	31.6	0.5 M H_2SO_4, 5000, 10

4.2.2.3 Accelerated Stress Tests: Load Cycling

To further investigate the interactions between the TOS_{SG} support and the catalyst particles, a load cycling AST protocol was performed. This involved 10,000 cycles scanned with a triangular waveform from 0.6-1.0 V_{RHE} with a retention time of 3 s, in N_2-saturated 0.5 M H_2SO_4 solution. To examine catalyst stability, the ECSA was monitored as a function of cycle number under the load cycling protocol (Figure 4.26a). The ECSA of Pt/TOS_{SG}, measured to be 35.0 m^2 g^{-1} which is ca. 3 times greater than that of the conventional Pt/TOS catalyst. The Pt/TOS_{SG} demonstrated a ca. 17% loss in ECSA over the course of the AST which indicated the good SMSI between the support and catalyst particles prevented Pt dissolution and agglomeration (Figure 4.26b). This compared favorably to the Pt/C catalyst. To examine the catalyst conductivity and support stability, EIS experiments were conducted throughout the AST. The EIS response for Pt/TOS_{SG} remained quite stable and demonstrated minimal variation in R_{Σ} (Figure 4.26c) and C_{LIM} (Figure 4.26d). This suggested the absence of support corrosion or Pt degradation. The higher C_{Lim} values can be explained by the smaller Ti particle size which has been shown to promote better charge storage capabilities as particle size decreases.[145,146]

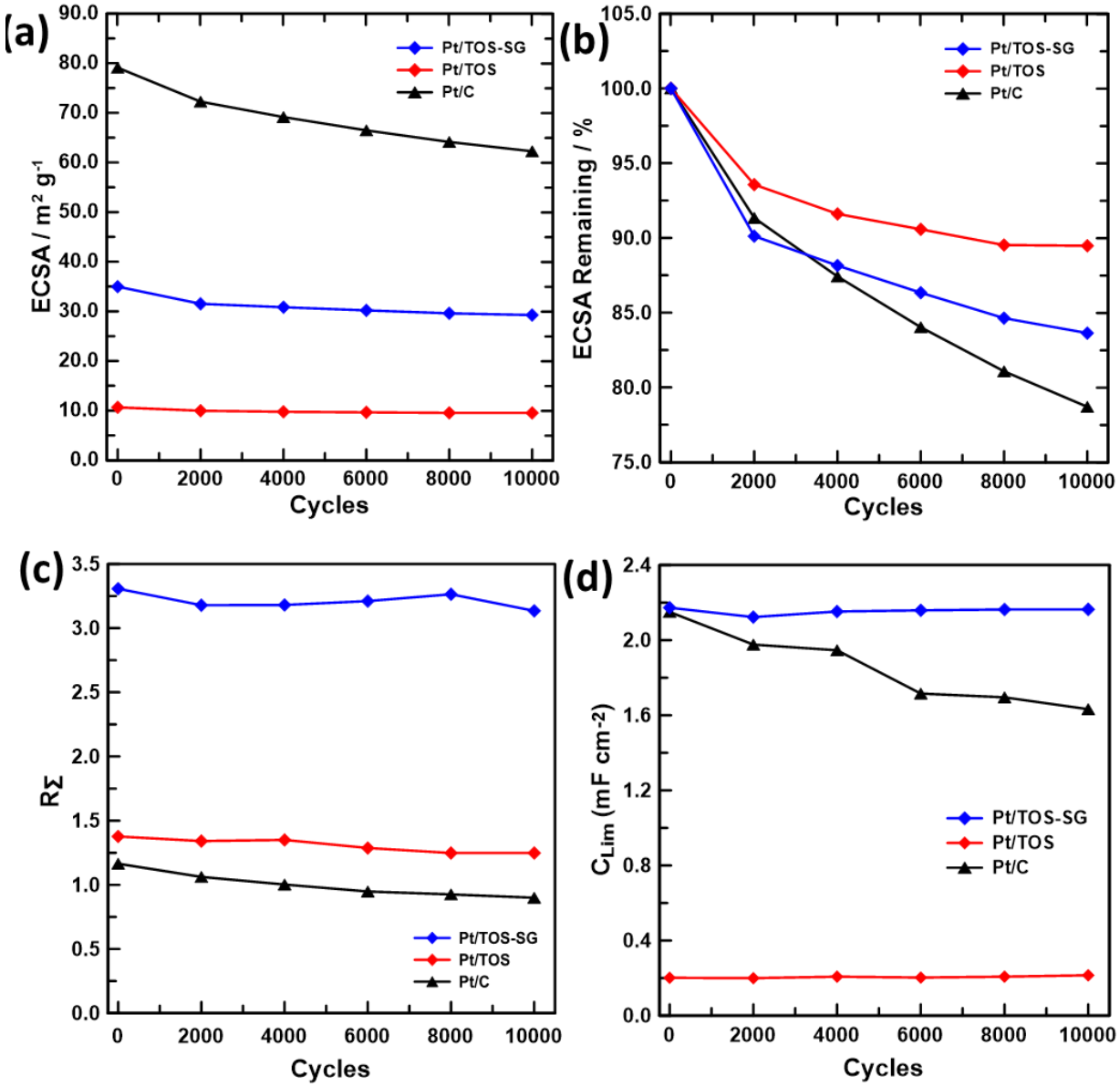

Figure 4.26. AST loading cycling protocol for the optimized Pt/TOS_{SG} catalyst showing the variation in (a) ECSA and (b) ECSA remaining over the course of the AST, obtained in N_2-purged 0.5 M H_2SO_4 solution. The variation in (c) R_Σ and (d) C_{Lim} over the course of the AST were recorded and obtained at a Bias potential of 0.425 V_{RHE}.

4.2.2.4 Accelerated Stress Tests: Startup/Shutdown

To further investigate the Pt/TOS_{SG} catalyst and TOS_{SG} support against corrosion and Pt degradation, it was subjected to the aggressive conditions of a startup/shutdown AST. This AST

applied a potential-square waveform cycled 10,000 times between 1.0-1.5 V_{RHE} with a retention time of 3 s in 0.1 M H_2SO_4 solution. The ECSA was monitored as a function of cycles which remained quite stable with only ca. 37% loss in ECSA observed (Figure 4.27a,b). This decrease was greater than that observed for Pt/TOS (ca. 28%) yet significantly less than the ca. 87% loss in ECSA for Pt/C. This indicates it is still possible for the TOS_{SG} support to facilitate SMSI between the catalyst particles. Despite this, the EIS response showed mild variation in R_{Σ} and relatively large increase in C_{Lim} which plateaued after 8,000 cycles (Figure 4.27c,d). The variation in C_{DL} corresponded to an increase in the surface area likely due to the formation of pseudocapacitive groups on the surface associated with residual carbon from the sol-gel process.

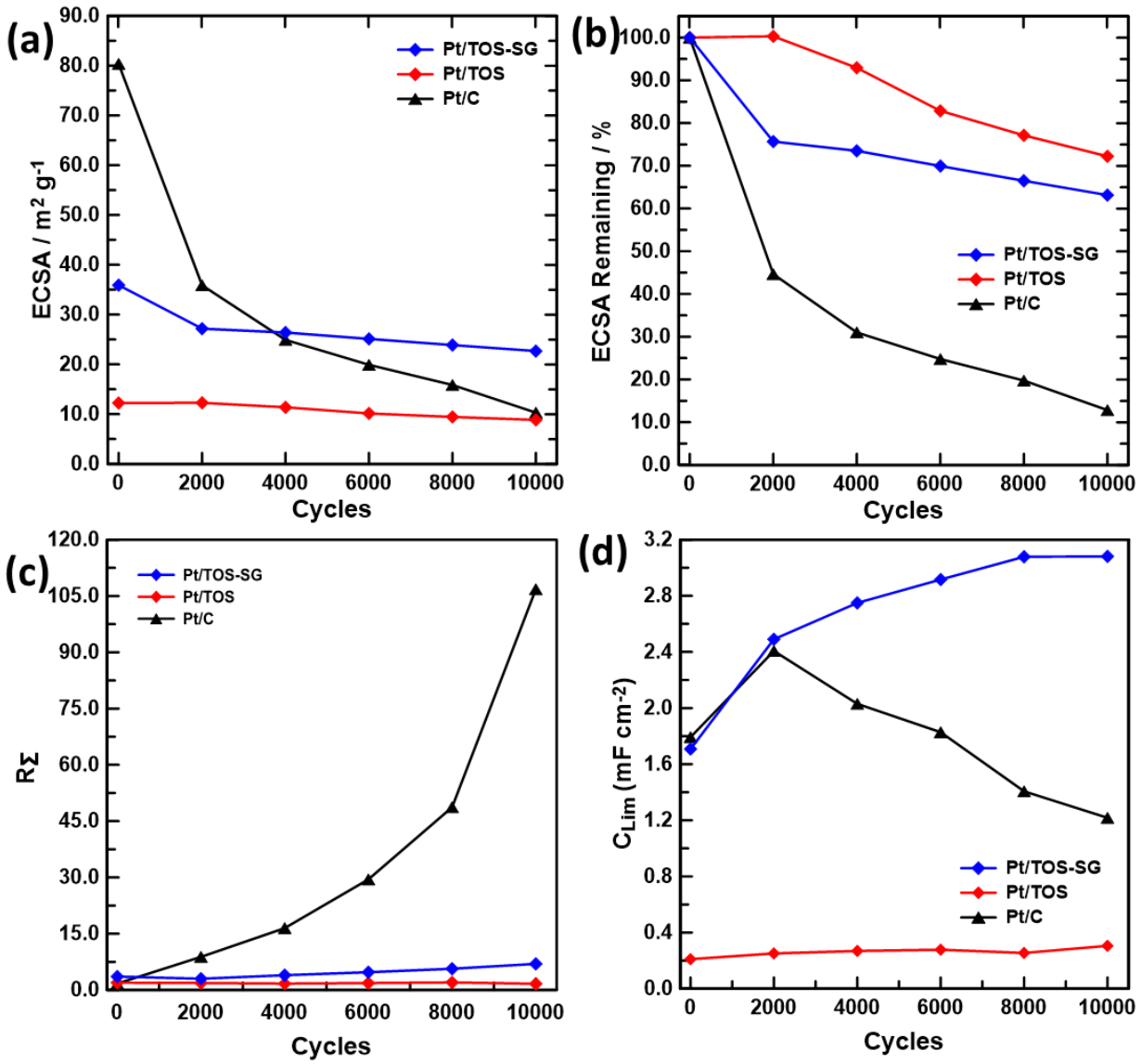

Figure 4.27. AST Startup/shutdown protocol for the optimized Pt/TOS_{SG} catalyst showing the variation in (a) ECSA and (b) ECSA remaining over the course of the AST, obtained in N_2-purged 0.5 M H_2SO_4 solution. The variation in (c) R_Σ and (d) C_{Lim} over the course of the AST were recorded and obtained at a Bias potential of 0.425 V_{RHE}.

4.2.2.5 Fuel Cell Testing

A membrane electrode assembly (MEA) consisting of a Pt/TOS_{SG} cathode and commercial Pt/C anode was prepared and tested in a 5 cm^2 cell (Fuel Cell Technologies) using a Fuel Cell Technologies single cell test station. Polarization and power density curves were obtained, with

H_2 and O_2 fed to the anode and cathode, respectively, using LabView software to control experimental parameters. The polarization curves in Figure 4.28a demonstrate similar performance between the Pt/TOS_{SG} and Pt/C catalysts. One subtle difference is that the Pt/TOS_{SG} catalyst exhibits almost no voltage loss due to mass transport as observed by the minimal voltage drop at the low potential region. This compared favorably to the Pt/C catalyst which exhibited a slight voltage drop at low potentials. Power density curves were also obtained from which the maximum power attainable by the cell was inferred (Figure 4.28b). The Pt/TOS_{SG} catalyst produced a maximum power density of 897.9 mW cm^{-2} whereas the Pt/C catalyst produced 850.8 mW cm^{-2} which demonstrated the enhanced capabilities of the TOS_{SG} support toward the Pt catalyst.

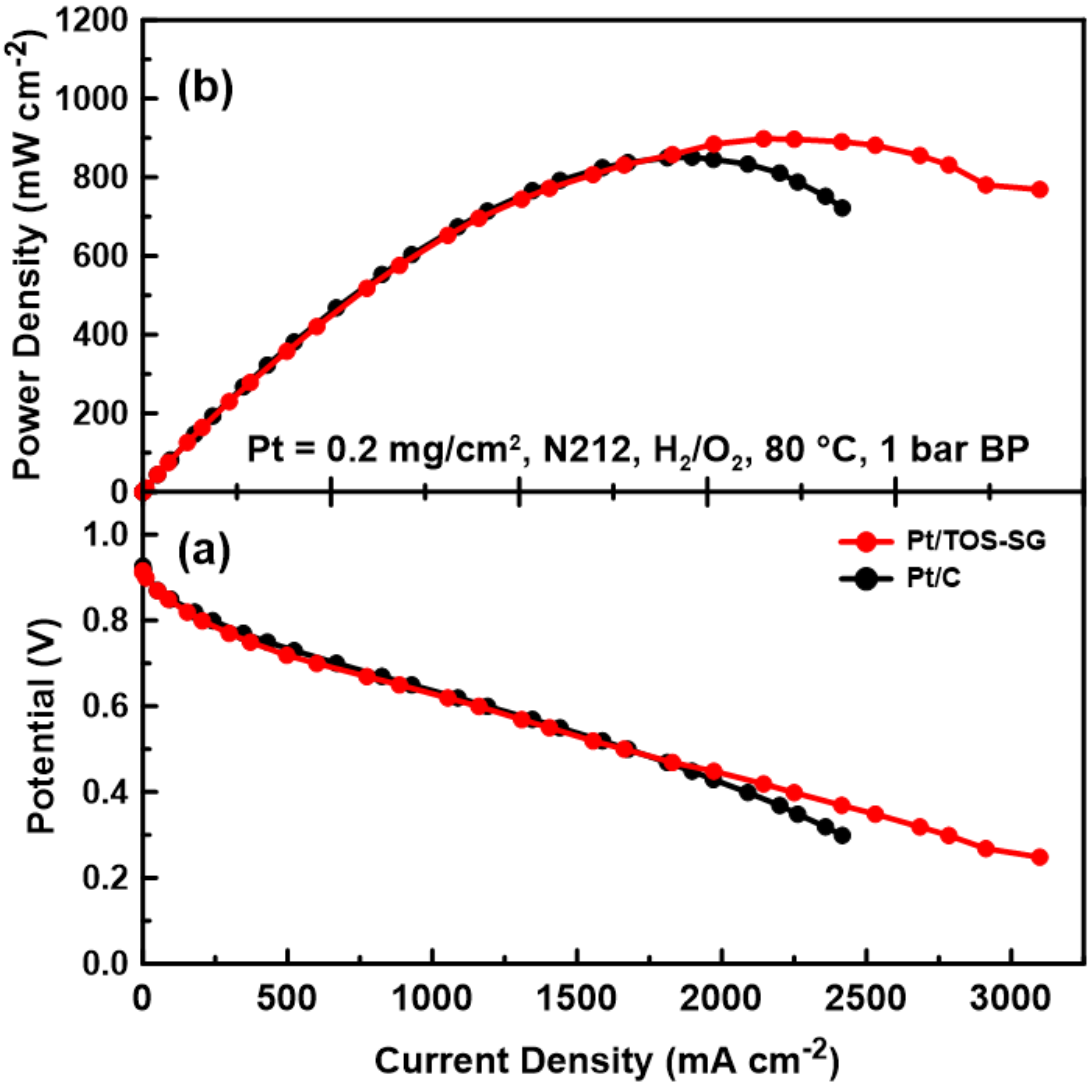

Figure 4.28. The fuel cell performance obtained for the Pt/TOS_{SG} catalyst compared to a commercial Pt/C catalyst. Data is presented as (a) power density and (b) polarization curves. Measurements recorded at 80 °C, with a Pt loading of 0.2 mg cm^{-2}, H_2 (g) and O_2 (g) were fed to the anode and cathode, respectively.

Figure 4.29a shows the polarization curves of the Pt/TOS_{SG} catalyst compared to the Pt/TOMS catalyst (ECSA = 89.6 m^2 g^{-1}) and a niobium-doped TiO_2 supported Pt catalyst (Pt/Nb-TiO_2) (ECSA = 43 m^2 g^{-1}) reported by He et al. which was chosen as another example of a highly durable catalyst.[71] Compared to these two catalysts, the Pt/TOS_{SG} was observed to experience very mild ohmic losses (ie. higher ionic membrane resistance and electronic support resistance).

This is evident at intermediate current densities where ohmic losses are traditionally observed.[94] Furthermore, at higher current densities both the Pt/TOMS and Pt/Nb-TiO_2 catalysts experience losses due to mass transport processes. The power density curves for the Pt/TOMS and Pt/Nb-TiO_2 catalysts were compared to Pt/TOS_{SG} and Pt/C in Figure 4.29b demonstrating maximum power densities of 1015.2 mW cm^{-2} and 705.5 mW cm^{-2}, respectively. Interestingly, it showed that while the Pt/TOS_{SG} catalyst possessed a relatively low ECSA, it was capable of outperforming the commercial Pt/C catalyst and Pt/Nb-TiO_2 catalyst using Si as a single dopant and approached similar performance capabilities of the Pt/TOMS catalyst. This suggests there is potential for the sol-gel process to produce a promising TOS support which can serve as a promising replacement of Pt/C as a fuel cell catalyst, even in the absence of Mo as a co-dopant. Moving forward, a more in-depth fuel cell study could be performed to investigate durability over 20,000 cycles, stability over 5,000 cycle startup/shutdown ASTs, and under different operating conditions (ie. humidity and temperature), and how these different parameters affect the MEA and overall fuel cell performance.

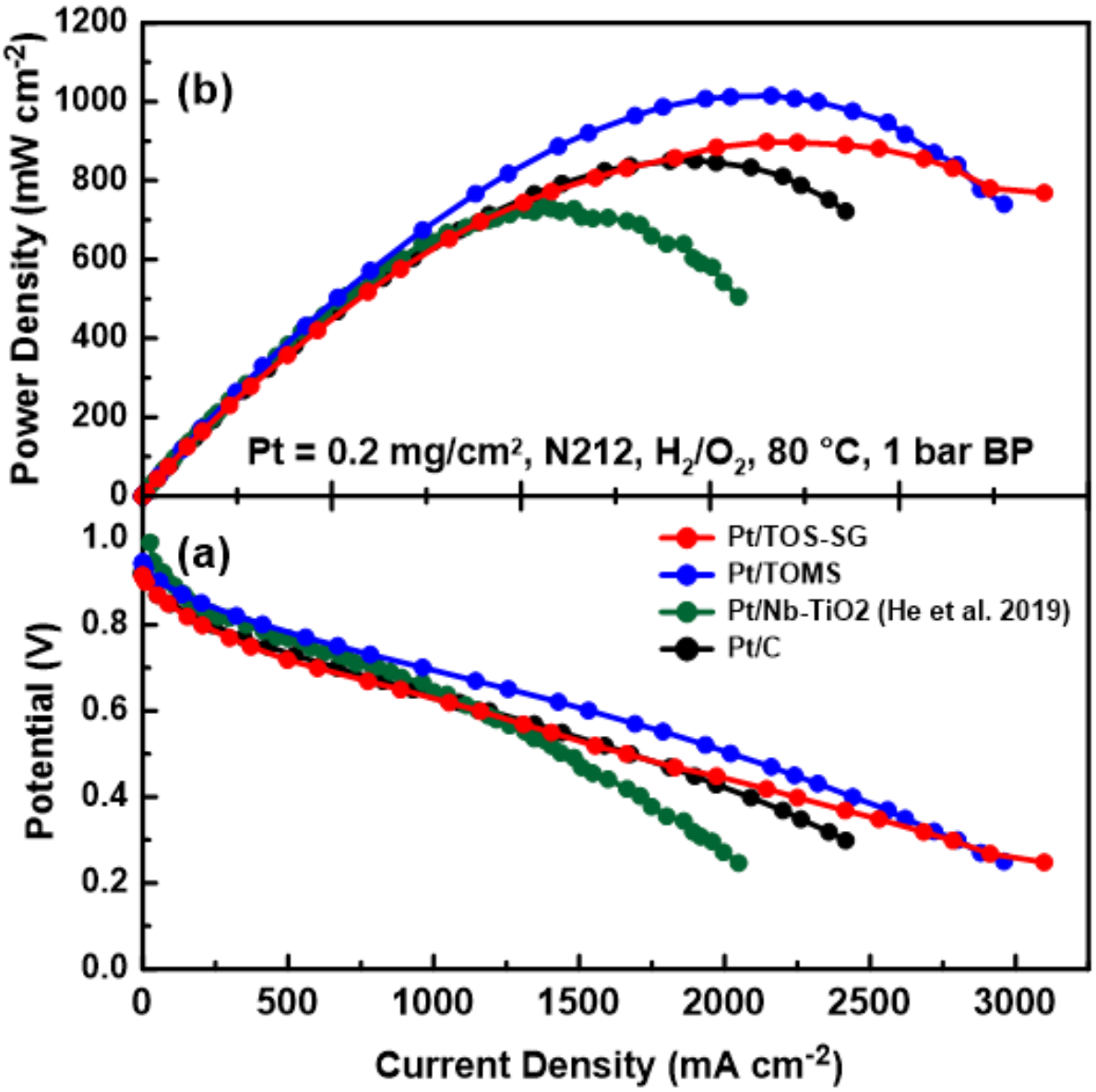

Figure 4.29. Comparison of the fuel cell performance obtained for the Pt/C, Pt/TOMS and Pt/TOS_{SG} catalysts. A $Pt/Nb\text{-}TiO_2$ catalyst is also referenced from He et al. (2019).[71] The data is shown as (a) power density and (b) polarization curves. Measurements recorded at 80 ^{o}C, with a Pt loading of 0.2 mg cm^{-2}, H_2 (g) and O_2 (g) were fed to the anode and cathode, respectively. The $Pt/Nb\text{-}TiO_2$ catalyst employed the use of a Nafion® 211 membrane.

4.3 Summary

The effect of incorporating smaller precursor materials in the synthesis of the TOS support to achieve higher surface area was explored in this chapter. Ball milling Si powder successfully

reduced from ca. 40 μm particle size to <1 μm particle size however, while this was enough to reduce the band gap of TiO_2 to 0.68 eV, it was unsuccessful in promoting adequate electron conduction or high surface area. In fact, the surface area of the TOS support was reduced substantially as the smaller Si particles occupied the Ti pores to a greater capacity. Electrochemical assessment of this support confirmed the high resistivity in the support layer due to the smaller Si particle size which impeded electronic conductivity within the TOS support. Thus, it was necessary to seek another method in which high surface area and conductivity could be achieved.

The encapsulation of Si via *in-situ* grown TiO_2 nanoparticles (ca. 15-20 nm in size) yielded a high surface area support (139.9 $m^2\ g^{-1}$) – nearly a 10-fold increase from the conventional support surface area (ca. 18 $m^2\ g^{-1}$). This TOS_{SG} support structure was analyzed via XRD which revealed the support structure to be dominated by the Ti_3O_5 suboxide phase, while the Ti_4O_7 phase was absent. The Ti_4O_7 phase is more conductive than the Ti_3O_5 phase which, in addition to the smaller particle size, lends to the lower conductivity of the TOS_{SG} support in contrast with the conventional TOS support. TEM images revealed the TOS_{SG} support possessed better distribution of Ti, O, and Si compared to the conventional TOS support in which Si formed unevenly distributed agglomerations and reduced overall Pt utilization of Pt/TOS. Electrochemical analysis revealed the TOS_{SG} support to be extremely stable during the 20,000 ADT and highly capacitive compared to the conventional TOS support owing to the smaller particle size.[145–147] The TOS_{SG} support also compared favorably to the TOM support synthesized by Esfahani et al., which possessed better electrical conductivity and a more narrow band gap overall.[73] The TOS_{SG} support performance was essentially on par with the TOMS support demonstrating that the

encapsulation of Si by TiO_2 via sol-gel synthesis can improve the overall performance of the support material.[79]

Once platinized, the support enabled better Pt utilization (ca. 35 $m^2 g^{-1}$) which was greater than that of Pt/TOM (22.3 $m^2 g^{-1}$) however, it was still less than that of Pt/TOMS (87.3 $m^2 g^{-1}$).[73,79] TEM images of the Pt/TOS_{SG} catalyst revealed the improved Pt utilization was a result of evenly distributed Si within the TOS_{SG} support which possessed surface -OH groups and served as the nucleation site for Pt NPs. The Pt/TOS_{SG} possessed improved activity toward the ORR (0.46 mA cm^{-2} produced at 0.9 V_{RHE}) compared to the conventional Pt/TOS catalyst which confirms the incorporation of smaller precursor material particle size to enhance the electrochemical properties. This performance is a stark comparison to the activity of the Pt/TOM and Pt/TOMS catalysts which produced 1.1 and 1.57 mA cm^{-2} at 0.9 V_{RHE}, respectively. The measured half-wave potential for Pt/TOS_{SG} after a 5,000 cycle ADT was observed to decrease, illustrated by a 10% shift to lower potentials (0.07 V_{RHE}), similar to the Pt/C catalyst. This shift in half-wave potential is slightly greater than that observed for Pt/TOM and Pt/TOMS, 0.04 V_{RHE} and 0.02 V_{RHE}, respectively.

Further examination of the relationship between the TOS_{SG} support and Pt particles was conducted via load cycling and startup/shutdown AST protocols. During the load cycling AST, the Pt/TOS_{SG} catalyst was stable compared to the Pt/C showing no significant changes in the ECSA or EIS response. During the more aggressive conditions of the startup/shutdown AST, the Pt/TOS_{SG} catalyst displayed a 37% decrease in ECSA, compared to nearly 90% decrease for Pt/C. In both cases of the load cycling and startup/shutdown ASTs, the decrease in Pt/TOS_{SG} ECSA was greater than that of Pt/TOMS where 93.2% and 91.3% ECSA remained after AST protocols, respectively.

The EIS response for Pt/TOS_{SG}, R_{Σ} and C_{Lim}, were observed to increase with potential cycling and was likely a result of the presence of residual carbon from the sol-gel synthesis of the support. On the other hand, the Pt/TOMS catalyst was observed as relatively stable, even under harsh AST protocols cycling up to 1.6 V_{RHE}.

Due to the success of the Pt/TOS_{SG} catalyst toward the *ex-situ* ASTs, it was subjected to further electrochemical testing via *in-situ* fuel cell performance tests on a single cell fuel cell test station. The results indicated the Pt/TOS_{SG} catalyst compared favorably to the commercial Pt/C catalyst such that the voltage loss due to mass transport was virtually absent in the Pt/TOS_{SG} catalyst. The power density curves revealed the Pt/TOS_{SG} could produce more power than the Pt/C catalyst. The fuel cell test results clearly demonstrated the enhanced capabilities of the TOS_{SG} support. This data suggests the practicality of TOS_{SG} as a potential electrocatalyst for fuel cell applications. In fact, the Pt/TOS_{SG} catalyst was compared to Pt/TOMS and a Pt/Nb-TiO_2 catalyst both which possess better resistance to ohmic losses however, it remained evident that the Pt/TOS_{SG} catalyst possessed better resistance to voltage losses due to mass transport. While there seems to be an advantage to doping the TiO_2 lattice with Mo and Si, and that Mo is associated with better ECSA and fuel cell performance, this data suggests that the novel sol-gel approach for synthesizing catalyst supports could enhance the overall performance of catalyst supports synthesized in the solid state.

Chapter 5: Conclusions and Future Work

The objective of this thesis was to synthesize a support that possessed good electronic conductivity and a narrow band gap, a large surface area, good resistance to corrosion, and good stability and activity toward the ORR. This work has established the influence of Si as a reducing agent on the physical and electrochemical properties of TiO_2, in the absence of Mo which favored the formation of a conductive titanium suboxide doped by Si, TOS.

The TOS support was optimized for 20 wt% Si and was associated with a narrow optical band gap and high electronic conductivity. It also demonstrated high durability and stability toward the ORR which was promising for FC applications. However, the TOS support possessed a low surface area due to the agglomeration of Si particles on the surface confirmed through TEM imaging and EDX mapping. This ultimately led to a non-uniform distribution of Pt NPs over the surface of the Pt/TOS catalyst and thus a low ECSA compared to a commercial Pt/C catalyst.

Further optimization of this TOS support explored using nanoparticle precursors during synthesis to enhance the surface area and improve the ECSA of the Pt supported catalysts. These supports included the TOS (Si BM 72h) and the TOS_{SG} support. These methods introduced smaller particle sizes within the TOS support, and it was hypothesized that as particle size decreased, the surface area would increase. The TOS (Si BM 72h) support was synthesized using the conventional solid-state approach where fresh Si was substituted for ball milled Si and used to dope fresh TiO_2. This support proved ineffective due to the pores of the Si NPs occupying the pores of the Ti particles such that the surface area was adversely affected and they inhibited electron conduction within the support material. This resulted in a very large resistance profile coupled with extremely low capacitance. As such, the TOS (Si BM 72h) support was deemed unfit as a

PEMFC catalyst support and another route to expanding the surface area was explored. The next modification to the TOS synthesis procedure incorporated ball milled Si encapsulated by *in-situ* grown TiO_2 nanoparticles by way of a novel sol-gel method. This produced the TOS_{SG} support and led to significantly smaller particle size and better distribution of Ti, O, and Si which was observed to facilitate better Pt utilization in the Pt/TOS_{SG} catalyst. This approach also provided a larger support surface area while producing adequate conductivity and maintaining a narrow band gap, comparing favorably to the TOM and TOMS supports.

The band gap energy was determined via diffuse reflectance spectroscopy and the electronic conductivity was established by measuring the resistance across the TOS support pellet. A narrow band gap energy and high conductivity were established for the conventional TOS 20 wt% Si support which compared favorably to the TOMS support. The TOS (Si BM 72h) support had a low electronic conductivity due to the Si NPs introducing grain boundaries and limiting electron conduction throughout the material. The TOS_{SG} support had narrow band gap and a conductivity comparable to that of TOMS which was a result of the overall reduced particle size which is known to introduce surface defects within the material that help narrow the gap. Cyclic voltammetry and EIS were also employed to provide a better look at the conductivity profiles of the TOS, TOS (Si BM 72h), and TOS_{SG} supports. The CV response of the TOS 10-20 wt% Si and TOS_{SG} supports adopted box-like responses which confirmed their conductivity. The TOS 2-5 wt% Si supports and TOS (Si BM 72h) support exhibited tailing in their CV profiles which was a result of high ohmic resistance. The EIS responses also provided insight toward the resistance associated with the conventional TOS supports. As the Si concentration was increased in the conventional TOS supports, the magnitude of the impedance scales decreased drastically as the

TiO_2 phase subsided and subsequently reduced to its suboxide phases. These results agreed with XRD analyses which indicated the TOS supports did in fact possess the desired suboxide phases necessary for electronic conduction in PEMFC applications. While the TOS_{SG} support demonstrated minimal resistance, the TOS (Si BM 72h) support displayed a large resistance profile which was a direct result of the Si NPs inhibiting electron conduction throughout the support material.

The conventional and optimized TOS supports, and their catalysts, demonstrated remarkable corrosion resistance due to the high oxidative state of the metals as well as the SMSI that occured between the supports and catalyst NPs. The durability of the supports was primarily investigated through ADTs using CV and EIS. The CV and EIS responses to the ADTs were monitored over 20,000 potential cycles during which the TOS supports exhibited no evidence of support degradation or changes to support layer resistance. Once platinized, the Pt/TOS and Pt/TOS_{SG} catalysts were exceptionally durable toward to the ADTs and ASTs. A commercial Pt/C catalyst was used as reference and the ECSA was observed to decay by 90% over the course of the ADT whereas the Pt/TOS and Pt/TOS_{SG} ECSA only decayed by ca. 17% and 25%, respectively.

The catalysts were then subjected to ASTs which are designed to evaluate the catalysts against support corrosion and Pt degradation. Under the AST protocols, the Pt/TOS and Pt/TOS_{SG} catalysts performed exceptionally well apart from Pt/TOS_{SG} exhibiting an increase in capacitance in response to the aggressive startup/shutdown test. This was characteristic of carbon oxidation and corrosion which was attributed to residual carbon present from the sol-gel process which was not entirely carbon-free. When compared to the commercial Pt/C catalyst, the Pt/TOS and Pt/TOS_{SG} catalysts overall demonstrated exceptional durability when subjected to the ASTs which

was a testament to the SMSI between the supports and catalyst NPs which limited any Pt NP agglomeration or dissolution.

To investigate the stability of the catalysts toward the ORR, the activity of the Pt/TOS and Pt/TOS_{SG} catalysts was measured. This involved LSVs which were obtained to assess the onset potential, the current produced at 0.9 V_{RHE}, and $E_{1/2}$. The $E_{1/2}$ was monitored before and after a 5,000 potential cycle ADT to compare stability. The Pt/TOS catalyst displayed poor ORR activity due to low ECSA which resulted from the low support surface area. Specifically, the Pt NPs formed agglomerations on the support surface which, through EDX mapping, was determined to be a result of the agglomeration of Si particles which served as anchors for the Pt NPs. While the Pt/TOs catalyst possessed low Pt utilization and poor ORR activity, it retained remarkable stability over the course of the ADT when compared to Pt/TOS_{SG} and Pt/C. The Pt/TOS_{SG} catalyst demonstrated improved support surface area and thus a higher ECSA and improved ORR activity. EDX mapping confirmed the uniform distribution of Si particles which possessed surface -OH groups to anchor the Pt NPs. While an improvement of the ORR activity was observed, the stability of the catalyst was comparable to that of Pt/C and was attributed to the presence of residual carbon. While this method was not carbon-free, it did establish the use of nanoparticles to produce a more durable, stable, and conductive metal oxide support. Further refinement of the synthetic process could eliminate the residual carbon product.

While the ASTs measured the activity and performance of the catalysts *ex-situ*, a brief *in-situ* fuel cell performance test was performed on the Pt/TOS_{SG} catalyst and compared to a commercial Pt/C catalyst, Pt/TOMS and $Pt/Nb\text{-}TiO_2$ (synthesized by He et al. 2019). The Pt/TOS_{SG} catalyst demonstrated improved resistance to mass transport voltage losses and a higher power

density compared to Pt/C and Pt-Nb-TiO_2. While the Pt/TOS_{SG} catalyst was outperformed by Pt/TOMS, it demonstrated good performance considering it possessed a smaller ECSA which illustrated the significance of the sol-gel synthetic method as a viable approach to improving the mass activities of metal oxide supports.

Finally, when considering the TOM and TOMS supports, it should be noted the TOM support possessed semi-conductive properties (ie. semi-conductor band gap and low conductivity) which were impractical for fuel cell application. Therefore, considering the success of the TOS support, which presented with conductor-like band gap and electronic conductivity, it is inferred that Si serves a critical role in lowering the band gap of the suboxide structure and improving overall conductivity. On the other hand, when comparing the TOS and TOS_{SG} supports to the TOM and TOMS supports, it appears Mo serves a more superficial role via altering the morphology of the support to yield a higher surface area.

Moving forward, carbon-free support materials on the nanoscale should be considered for the synthesis of future TOS supports. The TOS_{SG} support demonstrated the practicality of the novel sol-gel synthetic method and the importance of using nanoparticles in support synthesis to greatly enhance the surface area, which is necessary for better Pt utilization and, ultimately, improved ORR activity and fuel cell performance. In addition to the ORR, the Pt/TOS and Pt/TOS_{SG} present as likely catalysts for the methanol and ethanol oxidation reactions due to their durability and ability to facilitate good electron conduction. Specifically, the Pt/TOS_{SG} is promising as it offered better stability toward the ORR and demonstrated remarkable overall durability and stability when subjected to more aggressive AST protocols. It has also been reported in literature that the SMSI between the metal oxide supports and Pt NPs can suppress adsorption of reaction

intermediates such as CO and OH^- ions that impede the MOR and EOR.[148]

Due to limited time, further physical characterization of the TOS_{SG} support was not completed. Thorough characterization should include thermogravimetric analysis to quantify the extent of carbon content within the TOS_{SG} support. Additional TEM images would be beneficial in identifying d-spacing of the Pt/TOS catalysts to confirm particle size obtained from XRD analysis, as the catalytic activity of Pt electrocatalysts has been shown to depend on the orientation of their crystal structure.[149,150] XPS would also prove vital in determining the chemical states of Ti, Si, O, and Pt, as well as the SMSI between the TOS support and Pt catalyst. It would also be beneficial to perform additional *ex-situ* ASTs at elevated temperatures and increased upper potential limits to increase the stress on the support and catalyst materials.[22,149] This would provide more information on the durability and stability of the catalysts.

References

1. Edwards, P. P., Kuznetsov, V. L., David, W. I. F. & Brandon, N. P. Hydrogen and fuel cells: Towards a sustainable energy future. *Energy Policy*. **36**, 4356–4362 (2008).

2. Dell, R. Energy storage - a key technology for global energy sustainability. *J. Power Sources*. **100**, 2–17 (2001).

3. Pollet, B. G., Staffell, I. & Shang, J. L. Current status of hybrid, battery and fuel cell electric vehicles: From electrochemistry to market prospects. *Electrochim. Acta*. **84**, 235–249 (2012).

4. Gielen, D., Boshell, F., Saygin, D., Bazilian, M. D., Wagner, N. & Gorini, R. The role of renewable energy in the global energy transformation. *Energy Strateg. Rev.* **24**, 38–50 (2019).

5. Debe, M. K. Electrocatalyst approaches and challenges for automotive fuel cells. *Nature* **486**, 43–51 (2012.).

6. Borup, R., Meyers, J., Pivovar, B., Kim, Y. S., Mukundan, R., Garland, N., Myers, D., Wilson, M., Garzon, F., Wood, D., Zelenay, P., More, K., Stroh, K., Zawodzinski, T., Boncella, J., McGrath, J. E., Inaba, M., Miyatake, K., Hori, M., Ota, K., Ogumi, Z., Miyata, S., Nishikata, A., Siroma, Z., Uchimoto, Y., Yasuda, K., Kimijima, K. & Iwashita, N. Scientific Aspects of Polymer Electrolyte Fuel Cell Durability and Degradation. *Chem. Rev.* **107**, 3904–3951 (2007).

7. Borup, R. L., Kusoglu, A., Neyerlin, K. C., Mukundan, R., Ahluwalia, R. K., Cullen, D. A., More, K. L., Weber, A. Z. & Myers, D. J. Recent developments in catalyst-related PEM fuel cell durability. *Curr. Opin. Electrochem.* **21**, 192–200 (2020).

8. Sui, S., Wang, X., Zhou, X., Su, Y., Riffat, S. & Liu, C. jun. A comprehensive review of Pt electrocatalysts for the oxygen reduction reaction: Nanostructure, activity, mechanism and carbon support in PEM fuel cells. *J. Mater. Chem. A*. **5**, 1808–1825 (2017).

9. Kongkanand, A. & Mathias, M. F. The Priority and Challenge of High-Power Performance of Low-Platinum Proton-Exchange Membrane Fuel Cells. *J. Phys. Chem. Lett.* **7**, 1127–1137

(2016).

10. Kordesch, K. V. & Simader, G. R. Environmental Impact of Fuel Cell Technology. *Chem. Rev.* **95**, 191–207 (1995).

11. Sharma, S. & Pollet, B. G. Support materials for PEMFC and DMFC electrocatalysts - A review. *J. Power Sources*. **208**, 96–119 (2012).

12. Staffell, I., Scamman, D., Velazquez Abad, A., Balcombe, P., Dodds, P. E., Ekins, P., Shah, N. & Ward, K. R. The role of hydrogen and fuel cells in the global energy system. *Energy Environ. Sci.* **12**, 463–491 (2019).

13. Perry, M. L. & Fuller, T. F. A Historical Perspective of Fuel Cell Technology in the 20th Century. *J. Electrochem. Soc.* **149**, S59 (2002).

14. Bacon, F. T. Fuel cells, past, present and future. *Electrochim. Acta*. **14**, 569–585 (1969).

15. Appleby, A. J. From Sir William Grove to today: fuel cells and the future. *J. Power Sources*. **29**, 3–11 (1990).

16. Grove, W. R. On a Gaseous Voltaic Battery. *Philos. Mag.* **92**, 3753–3756 (2012).

17. Özgür, T. & Yakaryılmaz, A. C. A review: Exergy analysis of PEM and PEM fuel cell based CHP systems. *Int. J. Hydrogen Energy*. **43**, 17993–18000 (2018).

18. Barbir, F. Fuel Cell Basic Chemistry and Thermodynamics. *PEM Fuel Cells*. 17–32 (2013).

19. Singh, K., Tetteh, E. B., Lee, H. Y., Kang, T. H. & Yu, J. S. Tailor-Made Pt Catalysts with Improved Oxygen Reduction Reaction Stability/Durability. *ACS Catal.* **9**, 8622–8645 (2019).

20. Alipour Moghadam Esfahani, R., Ebralidze, I. I., Specchia, S. & Easton, E. B. A fuel cell catalyst support based on doped titanium suboxides with enhanced conductivity, durability and fuel cell performance. *J. Mater. Chem. A*. **6**, 14805–14815 (2018).

21. Fruehwald, H. M., Ebralidze, I. I., Zenkina, O. V. & Easton, E. B. Effect of Transition Metals on the Oxygen Reduction Reaction Activity at Metal-N 3 /C Active Sites. *ChemElectroChem*. **8**, 53–61 (2021).

22. He, C., Sankarasubramanian, S., Matanovic, I., Atanassov, P. & Ramani, V. Understanding

the Oxygen Reduction Reaction Activity and Oxidative Stability of Pt Supported on Nb-Doped TiO 2. *ChemSusChem*. **12**, 3468–3480 (2019).

23. Kumar, A. & Ramani, V. Ta 0.3 Ti 0.7 O 2 Electrocatalyst Supports Exhibit Exceptional Electrochemical Stability . *J. Electrochem. Soc.* **160**, F1207–F1215 (2013).

24. Barbir, F. Main Cell Components, Material Properties, and Processes. *PEM Fuel Cells* (2013.).

25. Holton, O. T. & Stevenson, J. W. The Role of Platinum in Proton Exchange Membrane Fuel Cells Evaluation of platinum's unique properties for use in both the anode and cathode of a proton exchange membrane fuel cell. *@BULLETPlatinum Met. Rev*. **57**, 259–271 (2013).

26. Fuel Cell 2016 Multi-Year Research, Development, and Demonstration Plan. (https://www.energy.gov/sites/prod/files/2017/05/f34/fcto_myrdd_fuel_cells.pdf (2016)).

27. Chen, S., Gasteiger, H. A., Hayakawa, K., Tada, T. & Shao-Horn, Y. Platinum-Alloy Cathode Catalyst Degradation in Proton Exchange Membrane Fuel Cells: Nanometer-Scale Compositional and Morphological Changes. *J. Electrochem. Soc.* **157**, A82 (2010).

28. Gasteiger, H. A., Panels, J. E. & Yan, S. G. Dependence of PEM fuel cell performance on catalyst loading. *J. Power Sources*. **127**, 162–171 (2004).

29. Thompson, S. T., James, B. D., Huya-Kouadio, J. M., Houchins, C., DeSantis, D. A., Ahluwalia, R., Wilson, A. R., Kleen, G. & Papageorgopoulos, D. Direct hydrogen fuel cell electric vehicle cost analysis: System and high-volume manufacturing description, validation, and outlook. *J. Power Sources*. **399**, 304–313 (2018).

30. Topalov, A. A., Cherevko, S., Zeradjanin, A. R., Meier, J. C., Katsounaros, I. & Mayrhofer, K. J. J. Towards a comprehensive understanding of platinum dissolution in acidic media. *Chem. Sci.* **5**, 631–638 (2014).

31. Li, L., Hu, L., Li, J. & Wei, Z. Enhanced stability of Pt nanoparticle electrocatalysts for fuel cells. *Nano Res.* **8**, 418–440 (2015).

32. Yu, X. & Ye, S. Recent advances in activity and durability enhancement of Pt/C catalytic

cathode in PEMFC. Part II: Degradation mechanism and durability enhancement of carbon supported platinum catalyst. *J. Power Sources*. **172**, 145–154 (2007).

33. Darling, R. M. & Meyers, J. P. Kinetic Model of Platinum Dissolution in PEMFCs. *J. Electrochem. Soc.* **150**, A1523 (2003).

34. Alipour Moghadam Esfahani, R., Rivera Gavidia, L. M., García, G., Pastor, E. & Specchia, S. Highly active platinum supported on Mo-doped titanium nanotubes suboxide (Pt/TNTS-Mo) electrocatalyst for oxygen reduction reaction in PEMFC. *Renew. Energy*. **120**, 209–219 (2018).

35. Jurkiewicz, K., Pawlyta, M. & Burian, A. Structure of Carbon Materials Explored by Local Transmission Electron Microscopy and Global Powder Diffraction Probes. *C*. **4**, 68 (2018).

36. Park, Y. C., Kakinuma, K., Uchida, M., Uchida, H. & Watanabe, M. Deleterious effects of interim cyclic voltammetry on Pt/carbon black catalyst degradation during start-up/shutdown cycling evaluation. *Electrochim. Acta*. **123**, 84–92 (2014).

37. Shahgaldi, S. & Hamelin, J. Improved carbon nanostructures as a novel catalyst support in the cathode side of PEMFC: A critical review. *Carbon N. Y.* **94**, 705–728 (2015).

38. Yu, X. & Ye, S. Recent advances in activity and durability enhancement of Pt/C catalytic cathode in PEMFC. Part I. Physico-chemical and electronic interaction between Pt and carbon support, and activity enhancement of Pt/C catalyst. *J. Power Sources*. **172**, 133–144 (2007).

39. Speder, J., Zana, A., Spanos, I., Kirkensgaard, J. J. K., Mortensen, K., Hanzlik, M. & Arenz, M. Comparative degradation study of carbon supported proton exchange membrane fuel cell electrocatalysts – The influence of the platinum to carbon ratio on the degradation rate. *J. Power Sources*. **261**, 14–22 (2014).

40. Odetola, C., Trevani, L. N. & Easton, E. B. Photo enhanced methanol electrooxidation: Further insights into Pt and TiO2 nanoparticle contributions. *Appl. Catal. B Environ.* **210**, 263–275 (2017).

41. Jia, N., Martin, R. B., Qi, Z., Lefebvre, M. C. & Pickup, P. G. Modification of carbon supported

catalysts to improve performance in gas diffusion electrodes. *Electrochim. Acta*. **46**, 2863–2869 (2001).

42. Ferreira, P. J., La O', G. J., Shao-Horn, Y., Morgan, D., Makharia, R., Kocha, S. & Gasteiger, H. A. Instability of Pt/C electrocatalysts in proton exchange membrane fuel cells: A mechanistic investigation. *J. Electrochem. Soc.* **152**, 2256–2271 (2005).

43. Yasuda, K., Taniguchi, A., Akita, T., Ioroi, T. & Siroma, Z. Platinum dissolution and deposition in the polymer electrolyte membrane of a PEM fuel cell as studied by potential cycling. *Phys. Chem. Chem. Phys.* **8**, 746–752 (2006).

44. Young, A. P., Stumper, J. & Gyenge, E. Characterizing the Structural Degradation in a PEMFC Cathode Catalyst Layer: Carbon Corrosion. *J. Electrochem. Soc.* **156**, B913 (2009).

45. Castanheira, L., Silva, W. O., Lima, F. H. B., Crisci, A., Dubau, L. & Maillard, F. Carbon corrosion in proton-exchange membrane fuel cells: Effect of the carbon structure, the degradation protocol, and the gas atmosphere. *ACS Catal.* **5**, 2184–2194 (2015).

46. Lyon, S. B. Corrosion of noble metals. *Shreir's Corros.* **1**, 2205–2223 (2010).

47. Zhang, Z., Liu, J., Gu, J., Su, L. & Cheng, L. An overview of metal oxide materials as electrocatalysts and supports for polymer electrolyte fuel cells. *Energy Environ. Sci.* **7**, 2535–2558 (2014).

48. Chhina, H., Campbell, S. & Kesler, O. Ex situ Evaluation of Tungsten Oxide as a Catalyst Support for PEMFCs. *J. Electrochem. Soc.* **154**, B533 (2007).

49. Martins, P. F. B. D. & Ticianelli, E. A. Electrocatalytic Activity and Stability of Platinum Nanoparticles Supported on Carbon-Molybdenum Oxides for the Oxygen Reduction Reaction. *ChemElectroChem*. **2**, 1298–1306 (2015).

50. Odetola, C., Trevani, L. & Easton, E. B. Enhanced activity and stability of Pt/TiO2/carbon fuel cell electrocatalyst prepared using a glucose modifier. *J. Power Sources*. **294**, 254–263 (2015).

51. Tauster, S. J., Fung, S. C., Baker, R. T. & Horsley, J. A. Strong interactions in supported-metal catalysts. *Science*. **211**, 1121–1125 (1981).

52. Alipour Moghadam Esfahani, R., Vankova, S. K., Easton, E. B., Ebralidze, I. I. & Specchia, S. A hybrid Pt/NbO/CNTs catalyst with high activity and durability for oxygen reduction reaction in PEMFC. *Renew. Energy*. **154**, 913–924 (2020).

53. Senevirathne, K., Hui, R., Campbell, S., Ye, S. & Zhang, J. Electrochimica Acta Electrocatalytic activity and durability of Pt / NbO 2 and Pt / Ti 4 O 7 nanofibers for PEM fuel cell oxygen reduction reaction. *Electrochim. Acta*. **59**, 538–547 (2012).

54. Gustavsson, M., Ekström, H., Hanarp, P., Eurenius, L., Lindbergh, G., Olsson, E. & Kasemo, B. Thin film Pt/TiO2 catalysts for the polymer electrolyte fuel cell. *J. Power Sources*. **163**, 671–678 (2007).

55. Fujishima, A. & Honda, K. Electrochemical Photolysis of Water at a Semiconductor Electrode. *Nature*. **238**, 37–38 (1972).

56. Pan, C. J., Tsai, M. C., Su, W. N., Rick, J., Akalework, N. G., Agegnehu, A. K., Cheng, S. Y. & Hwang, B. J. Tuning/exploiting Strong Metal-Support Interaction (SMSI) in Heterogeneous Catalysis. *J. Taiwan Inst. Chem. Eng.* **74**, 154–186 (2017).

57. Jiménez-Morales, I., Cavaliere, S., Jones, D. & Rozière, J. Strong metal-support interaction improves activity and stability of Pt electrocatalysts on doped metal oxides. *Phys. Chem. Chem. Phys.* **20**, 8765–8772 (2018).

58. Lewera, A., Timperman, L., Roguska, A. & Alonso-Vante, N. Metal-support interactions between nanosized Pt and metal oxides (WO 3 and TiO2) studied using X-ray photoelectron spectroscopy. *J. Phys. Chem. C*. **115**, 20153–20159 (2011).

59. Hepel, M., Dela, I., Hepel, T., Luo, J. & Zhong, C. J. Novel dynamic effects in electrocatalysis of methanol oxidation on supported nanoporous TiO2 bimetallic nanocatalysts. *Electrochim. Acta*. **52**, 5529–5547 (2007).

60. Huang, S. Y., Ganesan, P. & Popov, B. N. Electrocatalytic activity and stability of niobium-doped titanium oxide supported platinum catalyst for polymer electrolyte membrane fuel cells. *Appl. Catal. B Environ.* **96**, 224–231 (2010).

61. Onoda, M. Phase Transitions of Ti3O5. *J. Solid State Chem.* **136**, 67–73 (1998).

62. Walsh, F. C. & Wills, R. G. A. The continuing development of Magnéli phase titanium sub-oxides and Ebonex® electrodes. *Electrochim. Acta*. **55**, 6342–6351 (2010).

63. Xu, B., Sohn, H. Y., Mohassab, Y. & Lan, Y. Structures, preparation and applications of titanium suboxides. *RSC Adv.* **6**, 79706–79722 (2016).

64. Bartholomew, R. F. & Frankl, D. R. Electrical properties of some titanium oxides. *Phys. Rev.* **187**, 828–833 (1969).

65. Wang, L., Zhang, X., Liu, W., Xu, W., Singh, A. & Lin, Y. Electrochemical properties of Ti3O5 powders prepared by carbothermal reduction. *J. Mater. Sci. Mater. Electron.* **28**, 6421–6425 (2017).

66. Tanaka, K., Nasu, T., Miyamoto, Y., Ozaki, N., Tanaka, S., Nagata, T., Hakoe, F., Yoshikiyo, M., Nakagawa, K., Umeta, Y., Imoto, K., Tokoro, H., Namai, A. & Ohkoshi, S. I. Structural phase transition between γ-Ti3O5 and δ-Ti3O5 by breaking of a one-dimensionally conducting pathway. *Cryst. Growth Des.* **15**, 653–657 (2015.).

67. Liu, R., Shang, J. X. & Wang, F. H. Electronic, magnetic and optical properties of β-Ti3O 5 and λ-Ti3O5: A density functional study. *Comput. Mater. Sci.* **81**, 158–162 (2014).

68. Gusev, A. A., Avvakumov, E. G., Medvedev, A. Z. & Masliy, A. I. Ceramic electrodes based on magneli phases of titanium oxides. *Sci. Sinter.* **39**, 51–57 (2007).

69. Ohkoshi, S., Tsunobuchi, Y., Matsuda, T., Hashimoto, K., Namai, A., Hakoe, F. & Tokoro, H. Synthesis of a metal oxide with a room-temperature photoreversible phase transition. *Nat. Chem.* **2**, 539–545 (2010).

70. Hussain, S., Erikson, H., Kongi, N., Tarre, A., Ritslaid, P., Kikas, A., Kisand, V., Kozlova, J., Aarik, J., Tamm, A., Sammelselg, V. & Tammeveski, K. Platinum Sputtered on Nb-doped TiO 2 Films Prepared by ALD: Highly Active and Durable Carbon-free ORR Electrocatalyst . *J. Electrochem. Soc.* **167**, 164505 (2020).

71. He, C., Sankarasubramanian, S., Matanovic, I., Atanassov, P. & Ramani, V. Understanding the Oxygen Reduction Reaction Activity and Oxidative Stability of Pt Supported on Nb-Doped TiO2. *ChemSusChem*. **12**, 3468–3480 (2019).

72. Tsai, M. C., Nguyen, T. T., Akalework, N. G., Pan, C. J., Rick, J., Liao, Y. F., Su, W. N. & Hwang, B. J. Interplay between Molybdenum Dopant and Oxygen Vacancies in a TiO2 Support Enhances the Oxygen Reduction Reaction. *ACS Catal.* **6**, 6551–6559 (2016).

73. Alipour Moghadam Esfahani, R., Vankova, S. K., Monteverde Videla, A. H. A. & Specchia, S. Innovative carbon-free low content Pt catalyst supported on Mo-doped titanium suboxide (Ti 3 O 5 -Mo) for stable and durable oxygen reduction reaction. *Appl. Catal. B Environ.* **201**, 419–429 (2017).

74. Elezović, N. R., Babić, B. M., Radmilovic, V. R., Vračar, L. M. & Krstajić, N. V. Novel Pt catalyst on ruthenium doped TiO2 support for oxygen reduction reaction. *Appl. Catal. B Environ.* **140**–**141**, 206–212 (2013).

75. Ismael, M. Highly effective ruthenium-doped TiO2 nanoparticles photocatalyst for visible-light-driven photocatalytic hydrogen production. *New J. Chem.* **43**, 9596–9605 (2019).

76. Eastcott, J. I., Powell, J. A., Vreugdenhil, A. J. & Easton, E. B. Electrochemical and Morphological Studies of Ceramic Carbon Electrodes for Fuel Cell Systems. *ECS Trans.* **41**, 853–864 (2011).

77. Alipour Moghadam Esfahani, R., Moghaddam, R. B., Ebralidze, I. I. & Easton, E. B. A hydrothermal approach to access active and durable sulfonated silica- ceramic carbon electrodes for PEM fuel cell applications. *Appl. Catal. B Environ.* **239**, 125–132 (2018).

78. Alipour Moghadam Esfahani, R., Monteverde Videla, A. H. A., Vankova, S. & Specchia, S. Stable and methanol tolerant Pt/TiOx-C electrocatalysts for the oxygen reduction reaction. *Int. J. Hydrogen Energy*. **40**, 14529–14539 (2015).

79. Alipour Moghadam Esfahani, R., Ebralidze, I. I., Specchia, S. & Easton, E. B. A fuel cell catalyst support based on doped titanium suboxides with enhanced conductivity, durability and fuel cell performance. *J. Mater. Chem. A*. **6**, 14805–14815 (2018).

80. Alipour Moghadam Esfahani, R. & Easton, E. B. Exceptionally durable Pt/TOMS catalysts for fuel cells. *Appl. Catal. B Environ.* **268**, (2020).

81. Alipour Moghadam Esfahani, R., Moghaddam, R. B. & Easton, E. B. High performance

Pt/Ti3O5Mo0.2Si0.4 electrocatalyst with outstanding methanol oxidation activity. *Catal. Sci. Technol.* **9**, 4118–4124 (2019).

82. Alipour Moghadam Esfahani, R., Moghaddam, R. B. & Easton, E. B. Ultra-Durable Ti 3 O 5 Mo 0.2 Si 0.4 Fuel Cell Catalyst Supports with Enhanced Conductivity . *ECS Trans.* **92**, 603–611 (2019).

83. Kissinger, P. T. & Heineman, W. R. Cyclic voltammetry. *J. Chem. Educ.* **60**, 702–706 (1983).

84. Wang, H. *PEM Fuel Cells* 265–304 ((Elsevier), 2013.).

85. Easton, E. B. & Pickup, P. G. An electrochemical impedance spectroscopy study of fuel cell electrodes. *Electrochim. Acta*. **50**, 2469–2474 (2005).

86. Reid, O., Saleh, F. S. & Easton, E. B. Determining electrochemically active surface area in PEM fuel cell electrodes with electrochemical impedance spectroscopy and its application to catalyst durability. *Electrochim. Acta*. **114**, 278–284 (2013).

87. Lefebvre, M. C. Characterization of Ionic Conductivity Profiles within Proton Exchange Membrane Fuel Cell Gas Diffusion Electrodes by Impedance Spectroscopy. *Electrochem. Solid-State Lett.* **2**, 259 (1999).

88. Lefebvre, M., Qi, Z., Rana, D. & Pickup, P. G. Chemical synthesis, characterization, and electrochemical studies of poly(3,4-ethylenedioxythiophene)/ Poly(styrene-4-sulfonate) composites. *Chem. Mater.* **11**, 262–268 (1999).

89. Easton, E. B. & Pickup, P. G. An electrochemical impedance spectroscopy study of fuel cell electrodes. *Electrochim. Acta*. **50**, 2469–2474 (2005).

90. Reid, O. O., Saleh, F. S. & Easton, E. B. Application of the Transmission Line EIS Model to Fuel Cell Catalyst Layer Durability. *ECS Trans.* **61**, 25–32 (2014).

91. Saleh, F. S. & Easton, E. B. Diagnosing Degradation within PEM Fuel Cell Catalyst Layers Using Electrochemical Impedance Spectroscopy. *J. Electrochem. Soc.* **159**, B546–B553 (2012).

92. Bard, A. J. & Faulkner, L. R. Electrochemical methods fundamentals and applications.

((John Wiley & Sons), 2001.).

93. Yuan, X.-Z., Song, C., Wang, H. & Zhang, J. Electrochemical Impedance Spectroscopy in PEM Fuel Cells. ((Springer London), 2010.).

94. Zhang, J. PEM fuel cell electrocatalysts and catalyst layers: Fundamentals and applications. *PEM Fuel Cell Electrocatal. Catal. Layers Fundam. Appl.* (2008.).

95. Barbir, F. Fuel Cell Electrochemistry. *PEM Fuel Cells* (2013.).

96. Eastcott, J. I. & Easton, E. B. Investigation of Transport Mechanisms for Sulfonated Silica-Based Fuel Cell Electrode Structures. *J. Electrochem. Soc.* **162**, F764–F771 (2015).

97. Eastcott, J. I. & Easton, E. B. Sulfonated silica-based fuel cell electrode structures for low humidity applications. *J. Power Sources*. **245**, 487–494 (2014).

98. Alipour Moghadam Esfahani, R., Rivera Gavidia, L. M., García, G., Pastor, E. & Specchia, S. Highly active platinum supported on Mo-doped titanium nanotubes suboxide (Pt/TNTS-Mo) electrocatalyst for oxygen reduction reaction in PEMFC. *Renew. Energy*. **120**, 209–219 (2018).

99. Alipour Moghadam Esfahani, R., Moghaddam, R. B., Ebralidze, I. I. & Easton, E. B. A hydrothermal approach to access active and durable sulfonated silica-ceramic carbon electrodes for PEM fuel cell applications. *Appl. Catal. B Environ.* **239**, 125–132 (2018).

100. Makuła, P., Pacia, M. & Macyk, W. How To Correctly Determine the Band Gap Energy of Modified Semiconductor Photocatalysts Based on UV-Vis Spectra. *J. Phys. Chem. Lett.* **9**, 6814–6817 (2018.).

101. López, R. & Gómez, R. Band-gap energy estimation from diffuse reflectance measurements on sol-gel and commercial TiO 2: A comparative study. *J. Sol-Gel Sci. Technol.* **61**, 1–7 (2012).

102. Binninger, T., Fabbri, E., Kötz, R. & Schmidt, T. J. Determination of the Electrochemically Active Surface Area of Metal-Oxide Supported Platinum Catalyst. *J. Electrochem. Soc.* **161**, H121–H128 (2014).

103. Saleh, F. S. & Easton, E. B. Assessment of the ethanol oxidation activity and durability of Pt catalysts with or without a carbon support using Electrochemical Impedance Spectroscopy. *J. Power Sources*. **246**, 392–401 (2014).

104. Clavilier, J., Armand, D. & Wu, B. L. Electrochemical study of the initial surface condition of platinum surfaces with (100) and (111) orientations. *J. Electroanal. Chem.* **135**, 159–166 (1982).

105. Adler, D. Mechanisms for metal-nonmental transitions in transition-metal oxides and sulfides. *Rev. Mod. Phys.* **40**, 714–736 (1968).

106. Nasu, T., Tokoro, H., Tanaka, K., Hakoe, F., Namai, A. & Ohkoshi, S. Sol–gel synthesis of nanosized λ-Ti3O5 crystals. *IOP Conf. Ser. Mater. Sci. Eng.* **54**, 012008 (2014).

107. Olguí n, D., Vallejo, E. & Rubio-Ponce, A. Ab initio study of the low-pressure phases of Ti3O5. *Phys. Status Solidi Basic Res.* **252**, 659–662 (2015).

108. Gunkel, F., Christensen, D. V., Chen, Y. Z. & Pryds, N. Oxygen vacancies: The (in)visible friend of oxide electronics. *Appl. Phys. Lett.* **116**, (2020).

109. Kubelka, P. & Munk, F. An article on optics of paint layers. *Z. Tech. Phys*. **12**, 259–274 (1931).

110. Kubelka, P. New Contributions to the Optics of Intensely Light-Scattering Materials Part I. *J. Opt. Soc. Am.* **38**, 448–457 (1948).

111. Lin, H., Huang, C. P., Li, W., Ni, C., Shah, S. I. & Tseng, Y. H. Size dependency of nanocrystalline TiO2 on its optical property and photocatalytic reactivity exemplified by 2-chlorophenol. *Appl. Catal. B Environ.* **68**, 1–11 (2006).

112. Tauc, J., Grigorovici, R. & Vancu, A. Optical Properties and Electronic Structure of Amorphous Germanium. *Phys. status solidi*. **15**, 627–637 (1966).

113. Alipour Moghadam Esfahani, R., Vankova, S. K., Monteverde Videla, A. H. A. & Specchia, S. Innovative carbon-free low content Pt catalyst supported on Mo-doped titanium suboxide (Ti3O5 -Mo) for stable and durable oxygen reduction reaction. *Appl. Catal. B Environ.* **201**, 419–429 (2017).

114. Siracusano, S., Stassi, A., Modica, E., Baglio, V. & Aricò, A. S. Preparation and characterisation of Ti oxide based catalyst supports for low temperature fuel cells. *Int. J. Hydrogen Energy*. **38**, 11600–11608 (2013).

115. Zheng, L., Zeng, Q., Liao, S. & Zeng, J. Highly performed non-humidification membrane electrode assembly prepared with binary RuO 2-SiO 2 oxide supported Pt catalysts as anode. *Int. J. Hydrogen Energy*. **37**, 13103–13109 (2012).

116. Eastcott, J. I. & Easton, E. B. Sulfonated silica-based fuel cell electrode structures for low humidity applications. *J. Power Sources*. **245**, 487–494 (2014).

117. Seok, S., Choi, I., Lee, K. G., Choi, B. G., Park, K. J., Park, J. Y., Kwon, O. J., Lee, S. J. & Kim, D. H. Dopamine-induced Pt and N-doped carbon@silica hybrids as high-performance anode catalysts for polymer electrolyte membrane fuel cells. *RSC Adv.* **4**, 42582–42584 (2014).

118. Lo, C.-P. & Ramani, V. SiO 2 –RuO 2 : A Stable Electrocatalyst Support. *ACS Appl. Mater. Interfaces*. **4**, 6109–6116 (2012).

119. Alipour Moghadam Esfahani, R., Vankova, S. K., Monteverde Videla, A. H. A. & Specchia, S. Innovative carbon-free low content Pt catalyst supported on Mo-doped titanium suboxide (Ti3O5-Mo) for stable and durable oxygen reduction reaction. *Appl. Catal. B Environ.* **201**, 419–429 (2017).

120. Chiou, C. T. *Partit. Adsorpt. Org. Contam. Environ. Syst.* 39–52 ((John Wiley & Sons, Inc.), 2003.).

121. Eastcott, J. I. & Easton, E. B. Electrochemical studies of ceramic carbon electrodes for fuel cell systems: A catalyst layer without sulfonic acid groups. *Electrochim. Acta*. **54**, 3460–3466 (2009).

122. Kim, Y. S., Balland, V., Limoges, B. & Costentin, C. Cyclic voltammetry modeling of proton transport effects on redox charge storage in conductive materials: Application to a TiO2 mesoporous film. *Phys. Chem. Chem. Phys.* **19**, 17944–17951 (2017).

123. Augustyn, V., Simon, P. & Dunn, B. Pseudocapacitive oxide materials for high-rate

electrochemical energy storage. *Energy Environ. Sci.* **7**, 1597–1614 (2014).

124. Wang, Q., Li, M. & Wang, Z. Supercapacitive performance of TiO2 boosted by a unique porous TiO2/Ti network and activated Ti3+. *RSC Adv.* **9**, 7811–7817 (2019).

125. Moghaddam, R. B. & Easton, E. B. Impedance spectroscopy assessment of catalyst coated Nafion assemblies for proton exchange membrane fuel cells. *Electrochim. Acta*. **292**, 292–298 (2018).

126. Pinchuk, O. A., Dundar, F., Ata, A. & Wynne, K. J. Improved thermal stability, properties, and electrocatalytic activity of sol-gel silica modified carbon supported Pt catalysts. *Int. J. Hydrogen Energy*. **37**, 2111–2120 (2012).

127. Zhu, T., Du, C., Liu, C., Yin, G. & Shi, P. SiO 2 stabilized Pt/C cathode catalyst for proton exchange membrane fuel cells. *Appl. Surf. Sci.* **257**, 2371–2376 (2011).

128. Li, D., Wang, C., Strmcnik, D. S., Tripkovic, D. V., Sun, X., Kang, Y., Chi, M., Snyder, J. D., Van Der Vliet, D., Tsai, Y., Stamenkovic, V. R., Sun, S. & Markovic, N. M. Functional links between Pt single crystal morphology and nanoparticles with different size and shape: The oxygen reduction reaction case. *Energy Environ. Sci.* **7**, 4061–4069 (2014).

129. Alipour Moghadam Esfahani, R., Fruehwald, H. M., Afsahi, F. & Easton, E. B. Enhancing fuel cell catalyst layer stability using a dual-function sulfonated silica-based ionomer. *Appl. Catal. B Environ.* **232**, 314–321 (2018).

130. Easton, E. B., Qi, Z., Kaufman, A. & Pickup, P. G. Chemical modification of proton exchange membrane fuel cell catalysts with a sulfonated silane. *Electrochem. Solid-State Lett.* **4**, 59–62 (2001).

131. Borup, R. L., Davey, J. R., Garzon, F. H., Wood, D. L. & Inbody, M. A. PEM fuel cell electrocatalyst durability measurements. *J. Power Sources*. **163**, 76–81 (2006).

132. Parrondo, J., Han, T., Niangar, E., Wang, C., Dale, N., Adjemian, K. & Ramani, V. Platinum supported on titanium-ruthenium oxide is a remarkably stable electrocatayst for hydrogen fuel cell vehicles. *Proc. Natl. Acad. Sci. U. S. A.* **111**, 45–50 (2014).

133. Alipour Moghadam Esfahani, R. & Easton, E. B. Exceptionally durable Pt/TOMS catalysts

for fuel cells. *Appl. Catal. B Environ.* **268**, 118743 (2020).

134. Ohma, A., Shinohara, K., Iiyama, A., Yoshida, T. & Daimaru, A. Membrane and Catalyst Performance Targets for Automotive Fuel Cells by FCCJ Membrane, Catalyst, MEA WG. *ECS Trans.* **41**, 775–784 (2011).

135. Zana, A., Speder, J., Roefzaad, M., Altmann, L., Bäumer, M. & Arenz, M. Probing Degradation by IL-TEM: The Influence of Stress Test Conditions on the Degradation Mechanism. *J. Electrochem. Soc.* **160**, F608–F615 (2013).

136. Wu, J., Yuan, X. Z., Martin, J. J., Wang, H., Zhang, J., Shen, J., Wu, S. & Merida, W. A review of PEM fuel cell durability: Degradation mechanisms and mitigation strategies. *J. Power Sources*. **184**, 104–119 (2008).

137. Macauley, N., Papadias, D. D., Fairweather, J., Spernjak, D., Langlois, D., Ahluwalia, R., More, K. L., Mukundan, R. & Borup, R. L. Carbon Corrosion in PEM Fuel Cells and the Development of Accelerated Stress Tests. *J. Electrochem. Soc.* **165**, F3148–F3160 (2018).

138. Sharma, R. & Andersen, S. M. Quantification on Degradation Mechanisms of Polymer Electrolyte Membrane Fuel Cell Catalyst Layers during an Accelerated Stress Test. *ACS Catal.* **8**, 3424–3434 (2018).

139. Alipour Moghadam Esfahani, R. & Easton, E. B. Exceptionally durable Pt/TOMS catalysts for fuel cells. *Appl. Catal. B Environ.* **268**, 118743 (2020).

140. Guo, X. & Maier, J. Grain Boundary Blocking Effect in Zirconia: A Schottky Barrier Analysis. *J. Electrochem. Soc.* **148**, E121 (2001).

141. Thommes, M., Kaneko, K., Neimark, A. V., Olivier, J. P., Rodriguez-Reinoso, F., Rouquerol, J. & Sing, K. S. W. Physisorption of gases, with special reference to the evaluation of surface area and pore size distribution (IUPAC Technical Report). *Pure Appl. Chem.* **87**, 1051–1069 (2015).

142. Brus, L. E. Electron-electron and electron-hole interactions in small semiconductor crystallites: The size dependence of the lowest excited electronic state. *J. Chem. Phys.* **80**, 4403–4409 (1984).

143. Brus, L. Electronic wave functions in semiconductor clusters: Experiment and theory. *J. Phys. Chem.* **90**, 2555–2560 (1986).

144. Rino, J. & Studart, N. Structural correlations in titanium dioxide. *Phys. Rev. B - Condens. Matter Mater. Phys.* **59**, 6643–6649 (1999).

145. Wang, J., Polleux, J., Lim, J. & Dunn, B. Pseudocapacitive contributions to electrochemical energy storage in TiO 2 (anatase) nanoparticles. *J. Phys. Chem. C*. **111**, 14925–14931 (2007).

146. Brezesinski, T., Wang, J., Tolbert, S. H. & Dunn, B. Next generation pseudocapacitor materials from sol-gel derived transition metal oxides. *J. Sol-Gel Sci. Technol.* **57**, 330–335 (2011).

147. Rennie, A. J. R., Martins, V. L., Smith, R. M. & Hall, P. J. Influence of particle size distribution on the performance of ionic liquid-based electrochemical double layer capacitors. *Sci. Rep.* **6**, 1–10 (2016).

148. Pan, C., Tsai, M., Su, W., Rick, J., Akalework, N. G., Agegnehu, A. K., Cheng, S.-Y. & Hwang, B. Tuning/exploiting Strong Metal-Support Interaction (SMSI) in Heterogeneous Catalysis. *J. Taiwan Inst. Chem. Eng.* **74**, 154–186 (2017).

149. Alipour Moghadam Esfahani, R. & Easton, E. B. Exceptionally durable Pt/TOMS catalysts for fuel cells. *Appl. Catal. B Environ.* **268**, 118743 (2020).

150. Stamenkovic, V. R., Fowler, B., Mun, B. S., Wang, G., Ross, P. N., Lucas, C. A., Marković, N. M., Stamenkovic, V. R., Fowler, B., Mun, B. S. & Wang, G. Improved Oxygen Reducation Activity on Pt3Ni(111) via Increased Surface Site Availability. *Science (80-.).* **315**, 493–497 (2007).